


5-2018

# Design, Fabrication, and Characterization of Novel Optoelectronic Devices for Near-infrared Detection

Ahmad Nusir

*University of Arkansas, Fayetteville*

Follow this and additional works at: <http://scholarworks.uark.edu/etd>

 Part of the [Electronic Devices and Semiconductor Manufacturing Commons](#), and the [Semiconductor and Optical Materials Commons](#)

---

## Recommended Citation

Nusir, Ahmad, "Design, Fabrication, and Characterization of Novel Optoelectronic Devices for Near-infrared Detection" (2018). *Theses and Dissertations*. 2646.

<http://scholarworks.uark.edu/etd/2646>

This Dissertation is brought to you for free and open access by ScholarWorks@UARK. It has been accepted for inclusion in Theses and Dissertations by an authorized administrator of ScholarWorks@UARK. For more information, please contact [scholar@uark.edu](mailto:scholar@uark.edu), [ccmiddle@uark.edu](mailto:ccmiddle@uark.edu).

Design, Fabrication, and Characterization of Novel Optoelectronic Devices for Near-infrared  
Detection

A dissertation submitted in partial fulfillment  
of the requirements for the degree of  
Doctor of Philosophy in Engineering

by

Ahmad I. Nusir  
University of Jordan  
Bachelors of Science in Electrical Engineering, 2012  
University of Arkansas  
Masters of Science in Electrical Engineering, 2014

May 2018  
University of Arkansas

This dissertation is approved for recommendation to the Graduate Council.

---

Prof. Omar Manasreh  
Dissertation Director

---

Prof. Simon Ang  
Committee Member

---

Dr. Jingxian Wu  
Committee Member

---

Dr. Joseph B. Herzog  
Committee Member

## **Abstract**

Investigating semiconductor materials and devices at the nanoscale has become crucial in order to maintain the exponential development in today's technology. There is a critical need for making devices lower in power consumption and smaller in size. Nanoscale semiconductor materials provide a powerful platform for optoelectronic device engineers. They own interesting properties which include enhanced photoconductivity and size-tunable interband transitions.

In this research, different types of nanostructures were investigated for optoelectronic devices: nanocrystals, nanowires, and thin-films. First, lead selenide nanocrystals with narrow bandgap were synthesized, size-tailored, and functionalized with molecular ligands for the application of uncooled near-infrared photodetectors. The devices showed strong room-temperature responsivity that is covering the entire near-infrared spectral region. In the second investigation self-powered devices based on asymmetric Schottky contacts were designed and fabricated to efficiently detect near-infrared radiations without external biasing. The dimensions and the type of the metal contacts were optimized in order to improve on the device performance. Then silicon nanowires were integrated with the asymmetric contacts to further enhance the performance of the self-powered detectors by increasing the light absorption. Third, an array of gold thin-films was designed to enhance the photocurrent in the near-infrared through the internal photoemission of hot electrons. The photocurrent enhancement was studied as function of thickness and type of the metal thin-film.

Overall, those investigations provided important design considerations for future optoelectronic devices based on nanostructures. Moreover, the implementation of nanostructures with the devices showed superior performance as compared to the bulk.

© 2018 by Ahmad Nusir  
All Rights Reserved

## **Acknowledgment**

I would like to express my sincere gratitude to my graduate advisor and dissertation director, Prof. Omar Manasreh, for guiding me through all the years of my masters and doctoral research. His broad knowledge and technical experience in semiconductor materials and devices helped me in getting a good understanding of device engineering and semiconductor processing. Without his valuable instructions and guidance, none of this tremendous hard work will be achieved.

I am also thankful to my dissertation committee members: Prof. Simon Ang, Dr. Jingxian Wu, and Dr. Joseph Herzog for having the time to review my dissertation research.

I would like to thank my group members in Optoelectronics Research Lab: Mohammad Marie, Ramesh Vasan, Sanghamitra Mandal, Wafaa Gebriel, and Hayder Salman, for their help and support throughout my research projects. Also, I would like to thank Dr. Mourad Benamara and Stephen Bauman for helping me with the SEM imaging and Mr. Errol Porter for his assistance in the fabrication of devices.

## **Dedication**

This dissertation is dedicated to my parents, my wife, and my daughter for their help and support. Their valuable advises and wishes helped me to focus on the essentials. Without them I would not move this far.

## Table of Contents

|             |  |    |
|-------------|--|----|
| <b>I.</b>   | <b>Introduction</b> .....                                | 1  |
| <b>A.</b>   | <b>Nanocrystals</b> .....                                | 3  |
|             | Overview.....  | 3  |
|             | PbSe Nanocrystals.....                                   | 5  |
|             | Ligand Exchange.....                                     | 6  |
|             | Quantum Confinement.....                                 | 8  |
|             | Optical Properties.....                                  | 10 |
| <b>B.</b>   | <b>Nanowires</b> .....                                   | 11 |
| <b>C.</b>   | <b>Device Physics</b> .....                              | 13 |
|             | Basics of Photoconductivity.....                         | 13 |
|             | Schottky Junctions.....                                  | 16 |
|             | Metal-semiconductor-metals Photodetectors.....           | 18 |
|             | Hot Electrons and Internal Photoemission.....            | 21 |
| <b>D.</b>   | <b>Figures of Merits</b> .....                           | 22 |
| <b>II.</b>  | <b>Nanomaterials Growth and Device Fabrication</b> ..... | 24 |
| <b>A.</b>   | <b>Introduction</b> .....                                | 24 |
| <b>B.</b>   | <b>Nanocrystals Growth</b> .....                         | 24 |
|             | Synthesis of PbSe Nanocrystals.....                      | 24 |
|             | Ligand Exchange Procedure.....                           | 27 |
| <b>C.</b>   | <b>Nanowires Growth</b> .....                            | 28 |
|             | Metal-assisted Wet Etching.....                          | 28 |
|             | Electroless Etching.....                                 | 29 |
|             | Nanosphere Lithography.....                              | 30 |
| <b>D.</b>   | <b>Device Fabrication</b> .....                          | 32 |
|             | Optical Photolithography.....                            | 32 |
|             | Processing of Devices.....                               | 34 |
| <b>III.</b> | <b>Characterization Techniques</b> .....                 | 38 |
| <b>A.</b>   | <b>Introduction</b> .....                                | 38 |
| <b>B.</b>   | <b>Optical Characterization</b> .....                    | 38 |
|             | Optical Absorbance.....                                  | 38 |

|            |  |           |
|------------|--|-----------|
|            | Photoluminescence.....                           | 40        |
|            | Spectral Response.....                           | 42        |
|            | External Quantum Efficiency.....                 | 44        |
| <b>C.</b>  | <b>Electrical Characterization.....</b>          | <b>45</b> |
|            | Current-Voltage Characteristics.....             | 45        |
|            | Photocurrent Map.....                            | 46        |
| <b>IV.</b> | <b>Results and Discussion.....</b>               | <b>47</b> |
| <b>A.</b>  | <b>Introduction.....</b>                         | <b>47</b> |
| <b>B.</b>  | <b>PbSe Nanocrystals Photodetectors.....</b>     | <b>48</b> |
|            | Optical Properties.....                          | 48        |
|            | Ligand Exchange Effect.....                      | 53        |
|            | Device Photoresponse.....                        | 57        |
| <b>C.</b>  | <b>Self-powered Photodetectors.....</b>          | <b>63</b> |
|            | Device Optimization.....                         | 63        |
|            | Device Performance.....                          | 72        |
| <b>D.</b>  | <b>Photodetectors Based on Si Nanowires.....</b> | <b>75</b> |
|            | SEM Images.....                                  | 75        |
|            | Device Performance.....                          | 78        |
| <b>E.</b>  | <b>Hot Electrons in Au Thin-films.....</b>       | <b>83</b> |
|            | Photocurrent Map.....                            | 85        |
|            | Photoresponsivity Enhancement.....               | 86        |
|            | Effect of Thin-film Thickness.....               | 88        |
| <b>V.</b>  | <b>Conclusions.....</b>                          | <b>91</b> |
| <b>A.</b>  | <b>Summary.....</b>                              | <b>91</b> |
| <b>B.</b>  | <b>Contributions.....</b>                        | <b>92</b> |
| <b>C.</b>  | <b>Future Work.....</b>                          | <b>95</b> |
|            | <b>References.....</b>                           | <b>96</b> |



## List of Figures

|             |   |    |
|-------------|---|----|
| Figure 1.1  | Electromagnetic spectrum in the optical region.....   | 1  |
| Figure 1.2  | Ligand exchange process in nanocrystals grown using colloidal growth.....   | 7  |
| Figure 1.3  | Sketch of the band structure of nanocrystals.....   | 9  |
| Figure 1.4  | Absorbance and PL spectra of PbSe nanocrystals showing the Stokes shift.....  | 11 |
| Figure 1.5  | Top SEM image of Si nanowires grown using metal-assisted wet etching.....   | 13 |
| Figure 1.6  | Generation of photo-excited carriers and the drift mechanism in photodetectors.                                       | 14 |
| Figure 1.7  | Plot of the phot-excited carrier concentration as function of time under on/off light cycle.....                      | 15 |
| Figure 1.8  | Formation of Schottky junction between metal and n-type semiconductor.....  | 16 |
| Table 1.1   | List of metal work function ( $\phi_m$ ) and electron affinity of semiconductors ( $\chi_s$ ) [46].....               | 17 |
| Figure 1.9  | Sketch of the energy band diagram of self-powered near-infrared photodetector with structure of Au-undoped Si-Ti..... | 20 |
| Figure 1.10 | Internal photoemission mechanism in Schottky junctions.....   | 22 |
| Figure 2.1  | Sketch of the synthesis setup for growing the nanocrystals.....   | 25 |
| Figure 2.2  | Synthesis procedure of the PbSe nanocrystals.....   | 26 |
| Figure 2.3  | Mechanism of metal-assisted wet etching of Si in HF acid.....   | 28 |
| Figure 2.4  | Growth of Si nanowires using electroless etching.....   | 30 |
| Figure 2.5  | Growth of Si nanowires using nanosphere lithography.....  | 31 |
| Figure 2.6  | Microscopic images of the self-powered photodetector after each fabrication step.....                                 | 34 |

|             |  |    |
|-------------|--|----|
| Figure 2.7  | Microscopic images of asymmetrical interdigital electrodes spaced by a channel with width of (a) 50 $\mu\text{m}$ and (b) 5 $\mu\text{m}$ . (c) Image of the markers used in the alignment between the first mask and the second mask..... | 35 |
| Figure 2.8  | Etch profile of the prepared Si fingers using wet etching.....   | 35 |
| Figure 2.9  | Fabrication steps of the self-powered photodetector based on Si nanowires.....   | 36 |
| Figure 2.10 | Schematic of the uncooled near-infrared photodetector based on PbSe nanocrystals.....  | 37 |
| Figure 3.1  | Measurement of the optical absorbance of the dispersed nanocrystals.....   | 39 |
| Figure 3.2  | Process of producing monochromatic light using diffraction gratings.....   | 40 |
| Figure 3.3  | Sketch of the PL measurement setup using Bomem FTIR.....   | 42 |
| Figure 3.4  | Sketch of the spectral response measurement using Bruker FTIR.....   | 43 |
| Figure 3.5  | Setup of the EQE measurement.....  | 45 |
| Figure 3.6  | Setup of the photocurrent map measurement.....   | 46 |
| Figure 4.1  | Absorbance spectra of the synthesized PbSe nanocrystals. Reprinted with permission from Nusir <i>et al</i> [45].....   | 49 |
| Figure 4.2  | Absorbance and PL spectra of the PbSe nanocrystals at room-temperature (Inset: Schematic of the interband transition with the band structure of the nanocrystals). Reprinted with permission from Nusir <i>et al</i> [83].....             | 51 |
| Figure 4.3  | Absorbance spectra of PbSe nanocrystals grown at different reaction times.....   | 52 |
| Figure 4.4  | <i>I-V</i> curves of photodetectors based on PbSe nanocrystals capped with oleic acid (red curves) and MAA ligands (black curves). Reprinted with permission from Nusir <i>et al</i> [45].....   | 54 |

|             |   |    |
|-------------|---|----|
| Figure 4.5  | <i>I-V</i> curves of photodetectors based on PbSe nanocrystals capped with EDT ligands.....   | 54 |
| Figure 4.6  | Spectral response of photodetectors based on PbSe nanocrystals capped with (a) MAA and (b) EDT ligands at 5 V bias. Reprinted with permission from Nusir <i>et al</i> [45].....   | 55 |
| Figure 4.7  | <i>I-V</i> characteristics of three devices based on PbSe nanocrystals capped with MAA ligands with different electrode spacing. Reprinted with permission from Nusir <i>et al</i> [83].....  | 58 |
| Figure 4.8  | Calculated detectivity of the near-infrared photodetectors based on PbSe nanocrystals with different electrode spacing.....   | 59 |
| Figure 4.9  | Time-resolved photocurrent curve at 5 V for device with electrode spacing of 10 $\mu\text{m}$ . Reprinted with permission from Nusir <i>et al</i> [83].....   | 60 |
| Figure 4.10 | Spectral response of the near-infrared photodetectors based on PbSe nanocrystals with different electrode spacing ( $d = 10, 20, 50 \mu\text{m}$ ) at 5 V bias combined with the absorbance spectrum of the nanocrystals. Reprinted with permission from Nusir <i>et al</i> [83]..... | 62 |
| Figure 4.11 | Spectral response of the near-infrared photodetector with electrode spacing of 10 $\mu\text{m}$ at different bias voltages. Reprinted with permission from Nusir <i>et al</i> [83]..  | 63 |
| Figure 4.12 | <i>I-V</i> characteristics of the self-powered near-infrared photodetectors based on semi-insulating GaAs and asymmetric interdigital electrodes spaced by (a) 5 and (b) 50 $\mu\text{m}$ . Reprinted with permission from Nusir <i>et al</i> [84].....                               | 64 |

|             |  |    |
|-------------|--|----|
| Figure 4.13 | EQE spectra of the self-powered near-infrared photodetectors based on semi-insulating GaAs and asymmetric interdigital electrodes with different electrode spacing at 0 V bias. Reprinted with permission from Nusir <i>et al</i> [84].  | 66 |
| Figure 4.14 | (a) Spectral response of the self-powered devices based on semi-insulating GaAs and asymmetric interdigital electrodes with different spacing at 0 V bias. (b) Spectral response of device with electrode spacing of 50 $\mu\text{m}$ and different forward/reverse bias voltages. Reprinted with permission from Nusir <i>et al</i> [84]. | 68 |
| Figure 4.15 | EQE spectra of self-powered photodetectors based on undoped Si with different interdigital electrode spacing at 0 V bias.  | 69 |
| Figure 4.16 | <i>I-V</i> curves of devices with electrode spacing of 50 $\mu\text{m}$ and metal pairs of (a) Au-Ti, (b) Ag/Ti, and (c) Ag/Au.  | 70 |
| Figure 4.17 | EQE spectra of devices with electrode spacing of 50 $\mu\text{m}$ and metal pairs of (a) Au-Ti, (b) Ag/Ti, and (c) Ag/Au.  | 71 |
| Figure 4.18 | Time-resolved photocurrent curve of the device based on semi-insulated GaAs and Au/Ti interdigital electrodes spaced by 5 $\mu\text{m}$ . Reprinted with permission from Nusir <i>et al</i> [84].  | 72 |
| Figure 4.19 | <i>J-V</i> characteristics of the self-powered near-infrared photodetectors based on undoped Si and Au-Ti interdigital electrodes spaced by 50 $\mu\text{m}$ .   | 73 |
| Figure 4.20 | EQE and spectral response spectra at 0 V of the self-powered near-infrared photodetectors based on undoped Si and Au-Ti interdigital electrodes spaced by 50 $\mu\text{m}$ .   | 74 |
| Figure 4.21 | EQE of the self-powered photodetector and solar cell based on Si at 0 V.   | 75 |
| Figure 4.22 | SEM images of Si nanowires grown using electroless etching.  | 76 |

|             |   |    |
|-------------|---|----|
| Figure 4.23 | SEM images of Si nanowires grown using nanosphere lithpography with O <sub>2</sub> plasma for 20 min and Au (15 nm) metal catalyst.....   | 76 |
| Figure 4.24 | SEM images of Si nanowires grown using nanosphere lithpography with O <sub>2</sub> plasma for 25 min and Ag (40 nm) metal catalyst.....   | 77 |
| Figure 4.25 | SEM images of the vertically-aligned Si nanowires used in the fabrication of the self-powered near-infrared photodetectors. Reprinted with permission from Nusir <i>et al</i> [85].....   | 78 |
| Figure 4.26 | <i>J-V</i> curves of the control device and the device with Si nanowires under dark conditions (dashed lines) and light (solid lines). Reprinted with permission from Nusir <i>et al</i> [85].....  | 79 |
| Figure 4.27 | EQE spectra of the control device and two devices with Si nanowires at 0 V bias.....  | 80 |
| Figure 4.28 | (a) Spectral response spectra of the control device and device with Si nanowires at 0 V bias. Reprinted with permission from Nusir <i>et al</i> [85]. (b) Spectral response of devices based on symmetrical electrodes spaced by 50 μm at 3 V bias with and without nanowires ..... | 81 |
| Figure 4.29 | Microscopic image of the array of Au thin-films as applied between planar electrodes on semi-insulating GaAs substrate.....   | 84 |
| Figure 4.30 | Photocurrent map at bias voltage of 5 V over an Au thin-film with thickness of 30 nm. Reprinted with permission from Nusir <i>et al</i> [86].....   | 85 |
| Figure 4.31 | Enhancement in (a) the photocurrent and (b) the spectral response after applying an array of Au thin-film with thickness of 50 nm. Reprinted with permission from Nusir <i>et al</i> [86].....  | 87 |

|             |   |    |
|-------------|---|----|
| Figure 4.32 | Photocurrent enhancement at different: (a) Au and (b) Ti thicknesses. Reprinted with permission from Nusir <i>et al</i> [86]..... | 89 |
| Figure 4.33 | Reflections of hot electrons at the interfaces between Au/GaAs and Au/Ti/GaAs.....  | 89 |

## I. Introduction

The electromagnetic spectrum in the optical regime can be divided into three main spectral regions: ultra-violet, visible, and near-infrared. The wavelength range of each spectral region is shown in figure 1.1. Several optoelectronic devices were designed to operate in the near-infrared including: solar cells, light emitting diodes, and photodetectors [1]–[3]. Detection of near-infrared light is essential for variety of applications ranging from remote sensing to non-invasive biomedical diagnostics [4]–[6]. Furthermore, near-infrared detection has expanded to cover sensitive military applications like: night vision, target acquisition, and surveillance [7]–[9]. This has urged researchers to find new materials for devices capable of efficiently detecting wider spectral range in the near-infrared region.

Optical fiber communication is considered as the most important application that operates at wavelengths of 1.3 and 1.55  $\mu\text{m}$ , where the fiber dispersion is minimized. Another application based on near-infrared is optocouplers that are used for noise isolation and transmission of data through harsh environment. In addition to biomedical imaging that utilizes near-infrared detection for neuroscience research and cognitive studying. Near-infrared detection is also used for thermal efficiency analysis, optical switches, and microwave photonics.

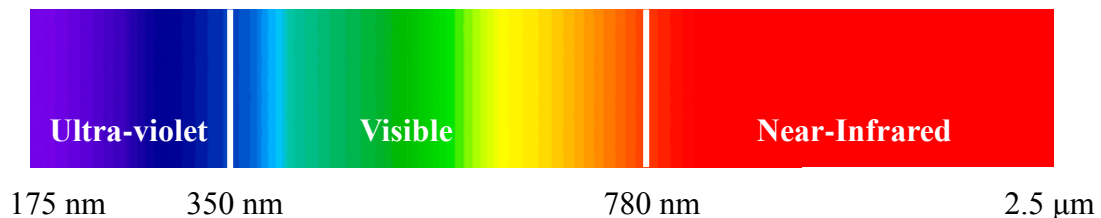


Figure 1.1 Electromagnetic spectrum in the optical region.

In the past years, the research on the investigation of semiconductor nanomaterials has gained a considerable attention [10]–[12]. Several nanostructures based on materials belonging to groups IV and III-V were studied to extract their optical, structural, and electrical characteristics [13], [14]. However, the incorporation of those nanomaterials with various optoelectronic devices is still not fully developed and requires further investigation.

Semiconductor nanomaterials, especially nanocrystals and nanowires, were widely investigated for future optoelectronic devices for their superior optical and electrical properties as compared to the bulk [15]. Examples on the optical properties of nanomaterials are: quantum confinement, bandgap tuning, antireflection property, and high optical absorption coefficient [16]–[18]. These properties are extremely useful for optoelectronic devices and could be exploited to improve on the performance of devices [19], [20]. The interband transitions between the conduction and valence bands within the confined band structure of the nanocrystals can be used in detecting a specific region within the near-infrared and to control the wavelength of emitted photons in light emitting diodes [21], [22]. Additionally, the antireflection property exhibited in nanowires can be used to enhance the light absorption and improve on the light-matter interaction in nanoscale devices [23], [24].

Chapter 1 is an introductory to the nanomaterials and their implementation in near-infrared detectors. This chapter discusses the optical and electrical properties of the nanomaterials used in this research. Furthermore, the chapter deals with the physics behind near-infrared photodetectors, Schottky junctions, and internal photoemission phenomena.

Chapter 2 is dedicated to discuss the approaches used in: synthesis of nanocrystals, ligand exchange, growth of nanowires, and the fabrication of devices. The fabrication techniques that



were used in this research are wet and dry etching, optical photolithography, and metal thin-film deposition.

Chapter 3 will discuss the techniques used to extract the optical and electrical characteristics of the grown nanomaterials and the fabricated devices. The optical properties were measured by using optical absorbance, photoluminescence, external quantum efficiency, and spectral response. The electrical properties of the devices were extracted by measuring the current-voltage characteristics under both dark and illumination conditions.

Chapter 4 presents and discusses the main outcomes of the research conducted to investigate the effect of nanostructures for optoelectronic devices. This chapter is divided into four main parts: PbSe nanocrystals and their application for photodetectors, self-powered near-infrared photodetectors, Si nanowires for enhancing the performance of near-infrared photodetectors, and hot electrons injection across Au thin-films.

Finally, in chapter 5 the research projects are summarized and concluded along with suggested future work.

## **A. Nanocrystals**

### Overview

Nanocrystals, also known as colloidal quantum dots, are useful for wide range of optoelectronic devices for their interesting optical and electrical properties. The bandgap of the nanocrystals can be easily controlled by varying the size of the nanocrystals [18]. This feature can be used to tune the spectral response of devices between the visible and infrared spectral regions depending on the applications [25]. Furthermore, the nanocrystals can be grown at low

temperatures and processed while suspended inside a solution [26]. This allows for the formation of thin-films of nanocrystals using non-vacuum deposition techniques like: drop cast, dip coating, and spin coating.

Nanocrystals are usually grown using colloidal growth, which involves mixing the precursors together and heating them at high temperature (150-300 °C) under inert gas atmosphere for a specific period of time [27]. The size of the grown nanocrystals depends on the growth temperature and the reaction time [21]. Usually longer reaction time will result in larger size of the nanocrystals. After the synthesis process, purifying the synthesized nanocrystals is essential to remove the reaction byproducts, unreacted components, and poorly capped nanocrystals. Finally the synthesized nanocrystals are dispersed inside a non-polar solvent for future processing and device fabrication. Nanocrystals grown by chemical routes are inherently n-type semiconductor.

Inorganic semiconductor nanocrystals are formed from binary, ternary, and quaternary elements belonging to several groups, like III-V and II-IV. For example, nanocrystals based on CdSe were investigated to control their size and shape [28]. Furthermore, optoelectronic devices based on binary compound nanocrystals were fabricated and characterized for photovoltaic applications, light emission, and photodetection [21], [29]. Nanocrystals can be capped with shells to improve on the photoluminescence and the emission of light, such as CdSe–ZnS core–shell, which is useful for light emitting diodes [30].

Nanocrystals based on ternary compound, such as CuInSe<sub>2</sub>, were investigated to replace the heavy metals, like lead and cadmium, and to be implemented in light harvesting applications for their high optical absorption coefficient [31]. Perovskite nanocrystal made from four

elements is another emerging discipline that caught the attention recently for the interesting optical properties. This includes high luminescence quantum yield and sharp and tunable emission peak [32].

### PbSe nanocrystals

Narrow-bandgap nanocrystals hold great potential for detecting the low energy part of the near-infrared spectral region (0.6-0.9 eV). And therefore can be used as a possible candidate in replacing the quantum wells for room-temperature near-infrared detection. Especially they are capable of detecting normal incident light and exhibit low dark current at room-temperature [33]. This feature enables photodetectors based on narrow-bandgap nanocrystals to operate without cooling down to cryogenic temperatures (77 K) in an attempt to reduce the thermal generation of carriers and consequently lower down the dark current [34].

Several narrow-bandgap nanocrystals were investigated for uncooled near-infrared detection including: PbS and HgTe [35], [36]. Among them is PbSe nanocrystals which possess interesting optical and electrical characteristics and therefore were implemented in various optoelectronic devices such as phototransistors, optical switches, and solar cells [37]–[39]. Lead selenide nanocrystals exhibit large Bohr exciton radius of 46 nm, which will allow in achieving extremely strong quantum confinement regime [40]. Size-tunable interband transition is another interesting property of PbSe nanocrystals that enables detecting wavelengths between 1 to 4  $\mu\text{m}$  [41]. In addition, PbSe is a direct bandgap material with bandgap of 0.26 eV in bulk [42]. Furthermore, multiple exciton generation in PbSe nanocrystals can help in achieving high power conversion efficiency for photovoltaic applications [38]. All of these optical and electrical

characteristics have made PbSe nanocrystals an interesting material for various optoelectronic devices that can be primarily used in near-infrared detection.

Several synthetic routes were proposed to grow high quality PbSe nanocrystals. Hot injection is one of the famous techniques in synthesizing PbSe nanocrystals [40]. It is based on the reaction between selenium stock solution and lead organic precursor at high temperature for a specific period of time. The selenium solution is prepared separately and it is injected into the lead precursor at temperature of 140 °C. Once the selenium is injected, nucleation occurs and continues to evolve into spherical PbSe nanocrystals that are capped with organic ligands. After the injection, the PbSe nanocrystals are allowed to grow between 20 seconds to four minutes. Further increase in the reaction time (>4 minutes) can result in the aggregations of the nanocrystals and will produce larger size with different shapes of nanocrystals like: square and star. The size of the synthesized PbSe nanocrystals can vary between 3 to 10 nm for reaction times less than 40 seconds. It is noted that larger size of PbSe nanocrystals will cause further narrowing in the bandgap and thus enables photodetectors to detect photons with lower energy. However, this will result in a significant increase in the dark current and will reduce the detectivity and the spectral response of the devices.

### Ligand Exchange

Nanocrystals grown using colloidal growth are capped with long organic ligands, such as oleic acid, which are made from long hydro-carbon chain. Those long organic ligands are extremely important to control the nucleation and the growth of the nanocrystals during the synthesis process [43]. Additionally, the ligands provide a chemical passivation for the nanocrystals, which is important to prevent aggregation and consequently the ability to

uniformly disperse the nanocrystals inside solvents. Therefore, the ligands enable nanocrystals to be dispersed inside a solution and thus creating thin-films of nanocrystals using spin or dip coating.

On the other hand, the ligands negatively impact the transport of carries between nanocrystals and consequently reduce the carrier mobility in the formed thin-films [44]. This is due to the fact that the ligands surrounding the nanocrystals are insulators and they prevent the photo-excited carriers from transportation between the nanocrystals under the influence of applied electric field. As a result, the long organic ligands should be exchanged with shorter and more conducting ones to enable the photo-excited carriers from tunneling between the nanocrystals [45]. The ligand exchange process is depicted in figure 1.2, and it shows how the long ligands are exchanged with shorter ligands that will reduce the spatial separation between adjacent nanocrystals.

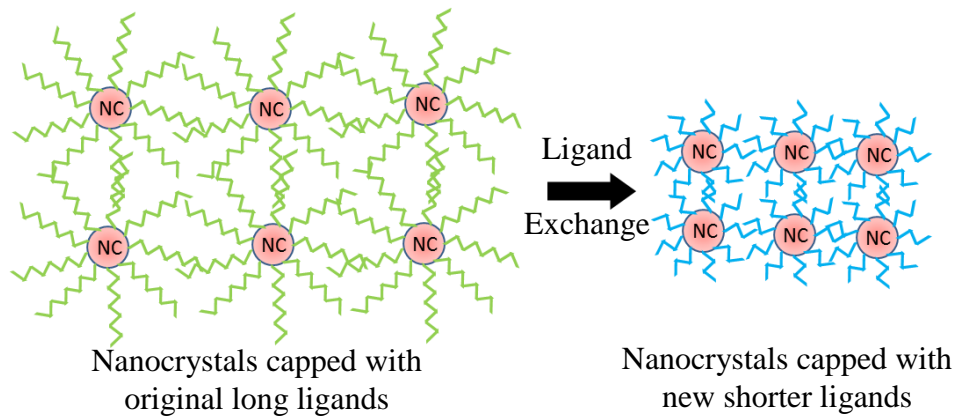


Figure 1.2 Ligand exchange process in nanocrystals grown using colloidal growth.

Example on the importance of ligand exchange on the performance of devices is CdSe nanocrystals [21], which are typically capped with oleic acid, an extremely long organic ligands consisting of 18 carbon atoms. Therefore the original ligands need to be exchanged with more

conducting ligands. For this purpose, the oleic acid was replaced with pyridine, which resulted in a significant improvement on the spectral response of the device with a photocurrent to dark current ratio of  $10^5$ . The new ligands (pyridine) allowed the photo-excited carriers in the nanocrystals to circulate between the electrodes of the device and generate high photocurrent as compared to the dark current.

### Quantum Confinement

Quantum confinement in nanocrystals results from the zero degree of freedom in the quantum dot nanostructure, similar to the situation of an electron trapped inside a box [46]. In such system, the electrons are treated as waves and allowed to exist in discretized energy levels, also called energy states. The wavelength ( $\lambda$ ) associated with electrons can be found by using the de-Broglie relation, which is expressed as the following:

$$\lambda = \frac{2\pi}{k} = \frac{h}{p} \quad (1.1)$$

where  $k$  is the wave number ( $\text{cm}^{-1}$ ),  $h$  is the Planck's constant, and  $p$  is the momentum. The momentum depends on the kinetic energy ( $E$ ) and can be found by  $E = p^2 / (2m^*)$ , where  $m^*$  is the effective mass of electrons. In nanoscale systems, the wavelengths associated with electrons cannot be neglected and are on the same order of the diameter of the nanocrystals. According to this, the wave properties of photons can be applied to electrons. The electrons are expressed by wave functions,  $\psi(r,t)$ , that can be found by solving a set of Schrodinger equations. The square of the electron wave function,  $|\psi(r,t)|^2 = \psi(r,t) \psi^*(r,t)$ , will give the probability of finding electrons at a certain point in time and space.

By solving Schrodinger equations for a confined system, such as nanocrystals, it will be found that electrons are allowed to stay in discrete energy states in both the conduction and valence bands, as shown in figure 1.3. Electrons can undergo transitions between energy states in the valence band to another energy states in the conduction band, which is called interband transition. Also electrons can do transitions between bound-to-bound or bound-to-continuum energy states within the conduction band, which is called intersubband transitions [46]. The bound-to-continuum intersubband transitions are important for devices, since the electron will become free and no more bound to the atom. According to this model, the effective bandgap is defined as the separation between the lowest energy state in the valence band and the lowest energy state in the conduction band. The effective bandgap ( $E_g^*$ ) is labeled in figure 1.3.

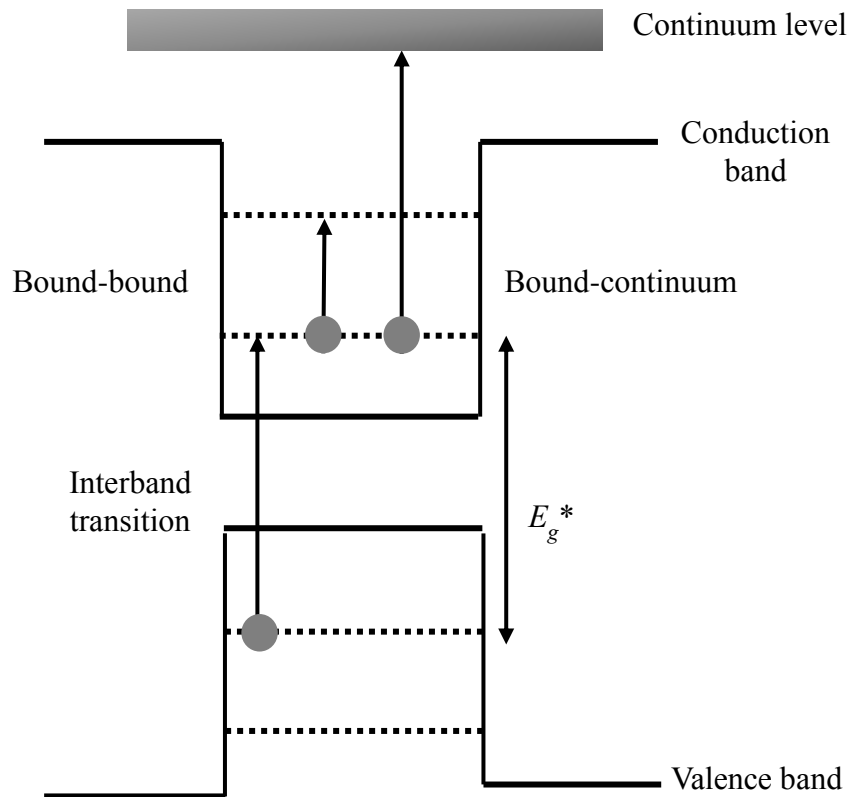


Figure 1.3 Sketch of the band structure of nanocrystals.

## Optical Properties

The optical properties of the nanocrystals greatly depend on their sizes. When the diameter of the nanocrystals is reduced, the energy separation between the discretized energy states becomes larger and fewer electronic transitions are obtained. This will result in increasing the bandgap. The effective bandgap ( $E_g^*$ ) of the nanocrystals can be found using [46]:

$$E_g^* = E_g + x^2 \frac{\pi^2 \hbar^2}{2m^* d^2} \quad (1.2)$$

where  $E_g$  is the bandgap in bulk,  $\hbar$  is the reduced Planck's constant,  $x$  is the reduced photon energy,  $m^*$  is the reduced effective mass, and  $d$  is the diameter of nanocrystals. According to equation 1.2, the effective bandgap of the nanocrystals is larger than the bulk bandgap and inversely proportional to square of the diameter of the nanocrystals. This means that a larger size of nanocrystals will shift the onset of the absorption spectrum into longer wavelength (less energy). To convert between energy (eV) into wavelength (nm) the relation  $\lambda=1240/E$  is used.

Another important factor that determines the optical property of the nanomaterials is the oscillator strength, which is the probability of obtaining an electronic transition between energy states [46]. Usually in nanocrystals, the oscillator strength associated with the interband transition between ground state in the valence band to ground state in the conduction band is the highest. This will result in stronger excitonic absorption of photons with energy equal to the effective bandgap of the nanocrystals.

The inverse of the absorption is called photoluminescence (PL). It is a radiative process and occurs after the electrons are excited into the conduction band by the absorption of photons with sufficient energy,  $E \geq E_g^*$ . In this process, when the electrons relax back from the



conduction band into the valence band, the energy is released as photons with wavelength of  $\lambda = h.c / E$ , where  $c$  is the speed of the light. It is noted that not all of the absorbed energy are emitted as photons; some of the energy is lost as vibrations to the atoms. This means that part of the energy is released in the form of generated phonons. As a result, the PL spectrum is shifted into lower energy (red shift) as compared to the absorption spectrum, which is called Stokes shift [46]. The typical optical absorbance and PL spectra of PbSe nanocrystals are plotted together in figure 1.4. This shows how the PL spectrum exhibits a red shift as compared to the absorbance due to the Stokes shift.

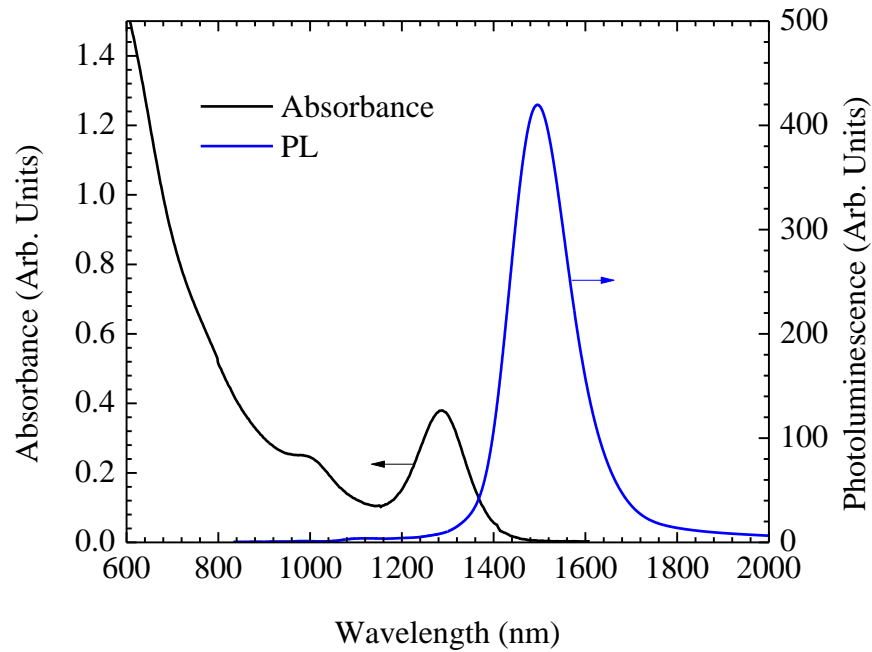


Figure 1.4 Absorbance and PL spectra of PbSe nanocrystals showing the Stokes shift.

## B. Nanowires

Nanowires exhibit one degree of freedom unlike the nanocrystals, which means that the charges are confined in two directions. Nanowires can be fabricated with diameters ranging

between 50 to 500 nm and using different materials, such as, ZnO, TiO<sub>2</sub>, and GaAs [47]–[49]. Many approaches were proposed to grow the nanowires like: sol-gel, vapor-liquid-solid, and top-down etching [50], [51]. Nanowires are used in variety of applications, like gate-all-around transistors, biosensors, antireflection coatings, and hydrophobic surfaces. For example, the nanowires can increase the aspect ratio of the active area of biosensors and therefore can increase the sensitivity of the device.

Silicon nanowires were implemented in optoelectronic devices for the interesting optical and electrical properties [52]–[55]. This includes enhanced light-matter interaction, quantum confinement, antireflection property, and efficient charge collection [56]–[58]. Silicon nanowires can be grown by using different top-down etching approaches based on metal-assisted wet etching, like electroless etching and nanosphere lithography [59]. In these methods, the surface of Si is coated with noble metals like silver or gold, which will catalyze etching the surface of Si in a faster rate as compared to uncovered areas [60]. Figure 1.5 is a top scanning electron microscopy (SEM) image showing Si nanowires grown by metal-assisted wet etching.

It is very important to control the dimensions of the Si nanowires, since the optical properties depend on the diameter and length of the nanowires. The spectral absorption can be tuned by changing the diameter of the Si nanowires [61]. In addition, the reflection from the surface depends on the length of the nanowires and decreases with longer ones [62]. Controlling the diameter of the nanowires is difficult using electroless etching. Therefore the other technique, nanosphere lithography, can be used to precisely control the diameter of the nanowires [63]. However, nanosphere lithography is more complex since it requires reactive ion etching. Both metal-assisted wet etching techniques were used in this research to grow vertically-aligned Si nanowires.

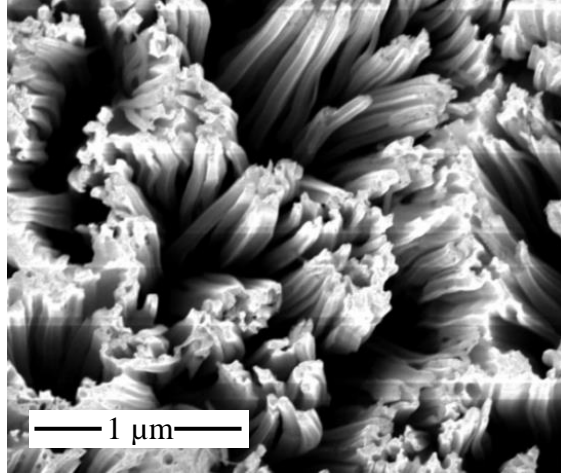


Figure 1.5 Top SEM image of Si nanowires grown using metal-assisted wet etching.

### C. Device Physics

#### Basics of Photoconductivity

A photoconductive material is made from a semiconductor that is capable of absorbing light with energy higher than the bandgap. The semiconductor material should have low intrinsic carrier concentration to reduce the amount of dark current (current without illumination). The basic concept of a photodetector made from a semiconductor slab and two electrodes biased at  $V_{\text{bias}}$  is shown in figure 1.6. Under incident radiation with sufficient energy, the semiconductor will absorb the incident photons and photo-excited carriers are generated, this will increase the total carrier concentration in the semiconductor.

If electric field is applied between the electrodes, the photo-excited carriers will circulate between the electrodes and generate a photocurrent as an output signal. The photocurrent ( $I_{\text{photo}}$ ) can be expressed using the drift current equation:

$$I_{\text{photo}} = \sigma EA = qlt(\mu_n \Delta n + \mu_p \Delta p)(V_{\text{bias}} / d) \quad (1.3)$$

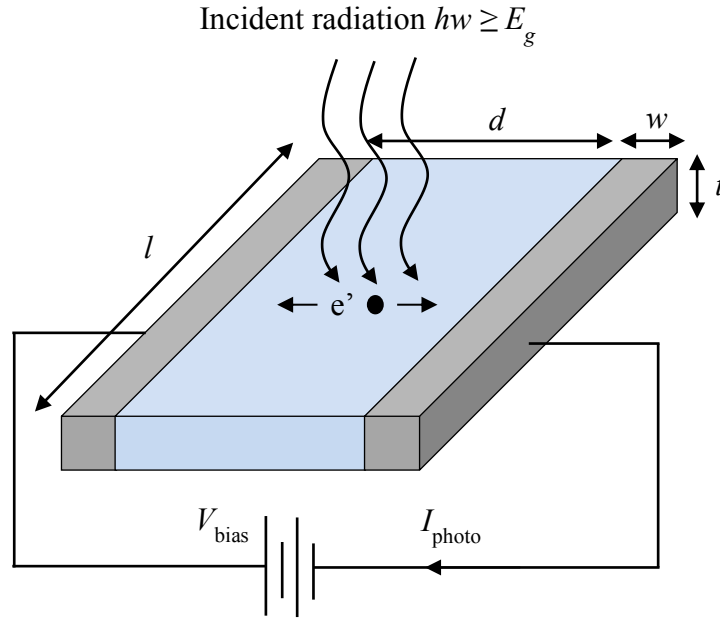


Figure 1.6 Generation of photo-excited carriers and the drift mechanism in photodetectors.

where  $\sigma$  is the conductivity,  $q$  is the electron charge,  $A$  is the cross section area of the electrodes and it is equal to  $l \times t$ ,  $\mu_n$  and  $\mu_p$  are the mobility of electrons and holes, respectively,  $\Delta n$  and  $\Delta p$  are the photo-excited carrier concentrations, and  $E$  is the applied electric field given by  $V_{\text{bias}}/d$ .

The active area of the photodetector where light is absorbed is equal to  $l \times d$ . Since the semiconductor material is intrinsic, the photo-excited carrier concentration is larger than the intrinsic carrier concentration ( $\Delta n \gg n_0$ ). The photo-excited carrier concentration can be expressed using:  $\Delta n = G_0\tau$ , where  $G_0$  is photo-excited carrier generation rate and  $\tau$  is the decay time constant of the carriers. The increase and decrease in the photo-excited carrier concentration under on/off light cycle is plotted in figure 1.7. When the light is switched off,  $\Delta n$  decreases exponentially with time. The value of  $G_0$  can be found using:

$$G_0 = \frac{cn\varepsilon}{2h\nu A} \phi \quad (1.4)$$

where  $c$  is the speed of light,  $n$  is the refractive index of semiconductor,  $\epsilon$  is the permittivity of the semiconductor,  $\nu$  is the frequency of incident light, and  $\phi$  is the sum of the square of local electric field. Increase in the device active area will increase  $\phi$  and more light will be absorbed.

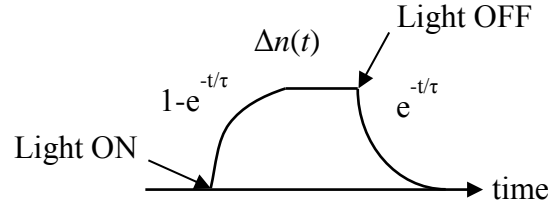


Figure 1.7 Plot of the phot-excited carrier concentration as function of time under on/off light cycle.

Another important factor in photodetectors is the photoconductive gain ( $G$ ), which is defined as the number of circulated carriers per incident photons. It is given by the following equation:

$$G = \frac{\tau}{\tau_{tr}} = \frac{\tau}{d^2 / (\mu_n V_{bias})} \quad (1.5)$$

where  $\tau_{tr}$  is the carrier transit time. As indicated from equation 1.5, the photoconductive gain can also be defined as the ratio between the recombination time and the carrier transit time. The carrier transit time is the time required for the photo-excited carriers to exist in the semiconductor before they are lost in recombination; the smaller  $\tau_{tr}$  is the higher  $G$ . The carrier transit time depends on the electrode spacing,  $d$ , and the bias voltage,  $V_{bias}$ , and can be reduced by reducing the electrode spacing or increasing the bias voltage. Also increasing the mobility of carriers will help in achieving higher values of photoconductive gain.

## Schottky Junctions

When a metal is in contact with the semiconductor, a Schottky junction is formed at the interface between the metal and the semiconductor. The Schottky barrier height ( $\phi_B = qV_B$ ) depends on the difference between the work function of the metal ( $\phi_m$ ) and the electron affinity of the semiconductor ( $\chi_s$ ). The barrier height energy is given by  $qV_B = \phi_m - \chi_s$  and the built-in potential energy is given by  $qV_{bi} = \phi_m - \phi_s$ , where  $\phi_s$  is the semiconductor work function. Figure 1.8 shows the formation of Schottky barrier at the interface between metal and n-type semiconductor. The width of the depletion region ( $W$ ) can be found using the following equation:

$$W = \left( \frac{2\epsilon V_{bi}}{qN_d} \right)^{0.5} \quad (1.6)$$

where  $N_d$  is the donor carrier concentration. It is noted that if the width of the depletion region is small enough, electrons can directly tunnel through the barrier between metal and semiconductor. Furthermore, by applying a positive bias voltage to the metal, the width of the depletion region reduces and current will flow through the forward biased junction. List of different metal work functions and electron affinities of semiconductors is shown in table 1.1.

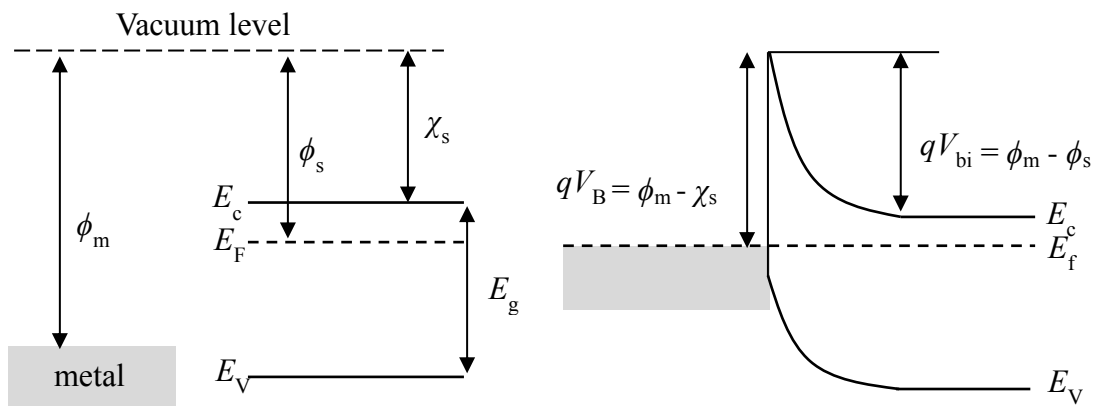


Figure 1.8 Formation of Schottky junction between metal and n-type semiconductor.

Table 1.1 List of metal work function ( $\phi_m$ ) and electron affinity of semiconductors ( $\chi_s$ ) [46].

| Metal | $\phi_m$ (eV) | Semiconductor | $\chi_s$ (eV) |
|-------|---------------|---------------|---------------|
| Au    | 5.10          | Si            | 4.01          |
| Ti    | 4.33          | GaAs          | 4.07          |
| Ag    | 4.26          | Ge            | 4.13          |
| Ni    | 5.15          | ---           | ---           |
| Al    | 4.28          | ---           | ---           |
| Cr    | 4.50          | ---           | ---           |
| W     | 5.55          | ---           | ---           |

The current density ( $J$ ) of the Schottky barrier device during forward bias can be expressed using:

$$J = J_s \left( e^{\frac{V_F}{k_B T / q}} - 1 \right) \quad (1.7)$$

where  $V_F$  is the forward bias voltage,  $k_B$  is the Boltzmann constant,  $T$  is the absolute temperature in kelvin, and  $J_s$  is the reverse saturation current density and given by:

$$J_s = A^* T^2 e^{\frac{-V_{bi}}{K_B T / q}} \quad (1.8)$$

where  $A^*$  is the effective Richardson constant and depends on the effective mass ( $m^*$ ) of electrons. The effective mass depends on the curvature of the  $E$ - $k$  band diagram ( $m^* \propto^{-1} d^2E/dk^2$ ). For carriers in GaAs, the effective mass is less than that for Si and therefore GaAs has higher mobility than Si. From equation 1.8, the reduction in the built-in potential will cause an increase

in the reverse saturation current of the device. Also an increase in temperature will increase the reverse saturation current, which is referred to thermionic emission of carriers above the Schottky barrier potential.

### Metal-semiconductor-metal Photodetectors

Various structural configurations of devices were fabricated by using p-n heterojunction and Schottky/ohmic contacts with vertical sandwich-like geometry and planar electrodes [64], [65]. Heterojunctions formed between two layers of different semiconductors were investigated for efficient optoelectronic conversion and collection of photo-excited carriers. On the other hand, metal-semiconductor-metal structure (MSM) can be considered for optoelectronic devices for its simplicity in fabrication and the ability to achieve high photoconductive gain [8]. Metal-insulator-semiconductor is another simple structure that was implemented for efficient near-infrared light harvesting [66]. The device is based on ITO/SiO<sub>2</sub>/Si nanowires interfaces. This requires the tunneling of photo-excited carriers through the SiO<sub>2</sub> layer in order to reach the metal contact (ITO). Furthermore, plasmonic waves were harnessed to enhance the near-infrared detection in metallic structures at the nanometer scale [67]. The surface plasmons generated in the metal will decay into energetic hot electrons that are injected into the semiconductor and consequently enhance the photocurrent.

The simplest structure of MSM photodetectors consists of two planar metallic electrodes deposited on a semiconductor, such as semi-insulating GaAs or undoped Si. The MSM photodetector has two symmetrical back-to-back Schottky junctions. With this configuration, the device requires external biasing in order to drive the photo-excited carriers and enable them to circulate. Under biasing, one Schottky junction will be forward biased while the other junction is



reversed biased. An increase in the bias voltage will increase the output signal by increasing the electric field applied between the electrodes.

Photodetectors based on MSM structure were fabricated using different materials that enabled detection in the ultra-violet, visible, and near-infrared spectral regions [8], [68], [69]. Furthermore, planar and vertical structures were investigated for MSM photodetectors. For example, ZnO was used to fabricate vertical MSM photodetectors capable of detecting wavelengths in the ultra-violet spectral region [70]. Additionally, CdSe nanocrystals were implemented in planar MSM photodetector with Au interdigital electrodes to detect wavelengths up to 730 nm, which covers the entire visible spectral region [21]. Additionally, InGaAs multiple quantum dots were used in MSM near-infrared photodetectors that can detect wavelengths up to 1  $\mu\text{m}$  [34].

As mentioned previously, the typical MSM photodetector consists of two symmetrical back-to-back Schottky junctions which require external biasing as a driving source. To allow photodetectors to operate without external biasing, junctions must be implemented in devices. Since the junction will create built-in electric field that is required to separate the photo-excited carriers. Schottky junctions are among the common types used in photovoltaic devices for their implantation simplicity. By using two different metal electrodes as contacts to the semiconductor, operation at 0 V bias can be possible [71]. The asymmetric Schottky junctions will create band bending due to the difference in Schottky barrier heights, which will generate the required built-in electric field.

Self-powered photodetectors are capable of detecting incident radiations at 0 V bias using internal photovoltaic effect and without consuming external power. This interesting feature will

make devices more reliable and will meet the demands of the energy-saving age. Self-powered devices operating in the ultra-violet region were fabricated using asymmetrical Schottky interdigital contacts [71]. However, these devices are based on wide bandgap materials like ZnO and therefore cannot detect visible and near-infrared radiations. The integration of asymmetrical interdigital electrodes with Si or GaAs will enable self-powered photodetectors to operate in the near-infrared region without biasing.

The self-powered near-infrared photodetectors can be realized by designing asymmetrical Schottky interdigital electrodes and depositing them on undoped Si or semi-insulating GaAs substrates. The use of two different metals, such as Ti and Au, in contact with the Si substrate will create different Schottky barriers at the Au/Si and Ti/Si interfaces, as shown in figure 1.9. The Schottky barrier energies at the Au/Si and Ti/Si interfaces were calculated to be 1.09 eV and 0.32 eV, respectively. This difference in the Schottky barrier energies will form band bending in Si similar to a regular p-n junction.

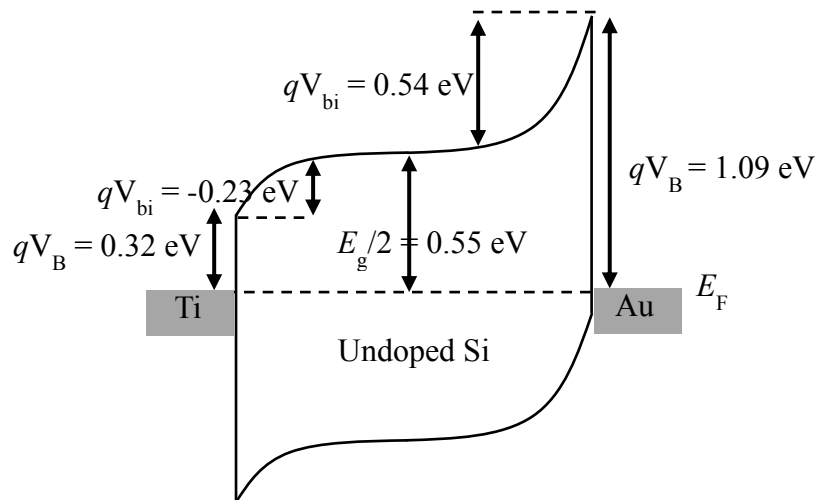


Figure 1.9 Sketch of the energy band diagram of self-powered near-infrared photodetector with structure of Au-undoped Si-Ti.

## Hot Electrons and Internal Photoemission

Metallic structures are used in optoelectronics devices like: photodetectors, solar cells, and light emitting diodes to enhance the device response and light-matter interaction [72], [73]. Metals are known for the high concentrations of free carriers that can become energetic by absorbing light and thus creating hot electrons. Hot electrons can also be excited by the plasmonic decay [74]. The hot electrons can be utilized in optoelectronic devices by the using Schottky contacts. The Schottky barrier energy ( $\phi_B = \phi_m - \chi_s$ ) formed at the interface between metal and semiconductor is used to detect photons with energy higher than the Schottky barrier energy,  $\hbar\omega \geq qV_B$ . In which hot electrons are created in the metal and injected across the Schottky barrier into the semiconductor. This phenomenon is known as internal photoemission [75], and the mechanism is shown in figure 1.10. Internal photoemission will allow absorbing photons with energy lower than the bandgap of the semiconductor ( $E_g \geq \hbar\omega \geq qV_B$ ). The Schottky junctions can be formed between metals and bulk semiconductor, like Si and GaAs, or two-dimensional materials, like graphene and MoS<sub>2</sub>.

Optical nanoantennas and nano-scale metallic structures were used to enhance the near-infrared detection of devices by generating hot electrons through the plasmonic decay [76]. However, the fabrication of those plasmonic structures is extremely difficult and requires nanoscale masking, which can be done by using electron-beam lithography and focused ion beam milling. The use of microscale metallic structures that can generate hot electrons will simplify the fabrication process since standard optical photolithography can be applied. Furthermore, it will enable absorbing more light as compared to the nanoscale structures and thus generating more hot electrons.

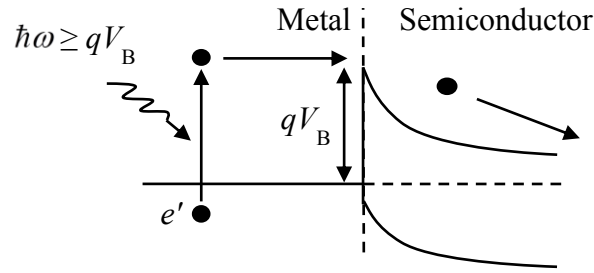


Figure 1.10 Internal photoemission mechanism in Schottky junctions.

In this research, an array of Au thin-films with microscale dimensions was deposited on GaAs and used to generate hot electrons. The generated hot electrons enhanced the photocurrent and spectral response in the near-infrared region. The formation of hot electrons was proved by measuring the photocurrent map as will be seen later in chapter 4 section E. The effect of increasing the thickness of the Au thin-film on the photocurrent enhancement was studied. Furthermore, the effect of adding Ti adhesive layer between the Au thin-film and GaAs on damping the photocurrent enhancement was also investigated.

#### D. Figures of Merits

Several figures of merits, like: responsivity, external quantum efficiency, and specific detectivity, are used in to measure the ability of photodetectors to detect light in an efficient manner. The key factor in obtaining high values of figures of merits is to achieve high signal-to-noise ratio (*SNR*). For photodetectors, the dark current is considered as the main source of noise while the photocurrent is considered as the signal to be detected. To obtain high *SNR*, the dark current needs to be minimized. One of the approaches to reduce the dark current is to passivate the surface of the nanocrystals during the ligand exchange process with functional capping group to control their electrical properties [45]. On the other hand, the photocurrent could be enhanced

by increasing both the device active area to absorb more light and the applied electric field to achieve higher photoconductive gain.

Responsivity ( $R$ ) is measured in the units of A/W and is defined as the ratio between the output photocurrent to the incident optical power. External quantum efficiency (EQE) is defined as the ratio between the collected electrons per incident photons. The EQE in percentage can be derived from  $R$  using the following equation:

$$\text{EQE} = \frac{R * 1240}{\lambda} \quad (1.9)$$

where  $\lambda$  is the wavelength of incident light in the units of nm. Both  $R$  and EQE are function of wavelength. For the specific detectivity ( $D^*$ ), it can be calculated in the units of  $\text{cm.Hz}^{0.5}/\text{W}$  using the following equation:

$$D^* = \frac{(A\Delta f)^{0.5} R}{N_s} \quad (1.10)$$

where  $A$  is the effective active of the photodetector,  $\Delta f$  is the electric bandwidth, and  $N_s$  is the noise spectral density. The noise consists of Shot noise, Johnson noise, and Flicker noise. The Shot noise resulting from the dark current is considered as the dominant source of noise in near-infrared photodetectors [77]. Since near-infrared detectors are based on narrow-bandgap materials with bandgap energy that is on the same order of the thermal energy ( $E_g \approx kT/q$ ). As a result, the thermally generated carries will increase the dark current and reduce the overall detectivity of the photodetectors. The spectral density of the shot noise can be found using  $N_s = (2q I_{\text{dark}} \Delta f)^{0.5}$ , where  $I_{\text{dark}}$  is the dark current of the device [77].

## **II. Nanomaterials Growth and Device Fabrication**

### **A. Introduction**

This chapter will present the methodology used in growing the nanomaterials and fabricating the optoelectronic devices. The PbSe nanocrystals were synthesized by colloidal growth and the vertically-aligned Si nanowires were grown by metal-assisted wet etching. On the other hand, the optoelectronic devices were fabricated inside class-100 cleanroom equipped with the facilities for photolithography, wet and dry etching, and thin-film deposition.

This chapter is divided into three main sections: nanocrystals growth, nanowires growth, and device fabrication. Section B is the nanocrystals growth and will discuss the synthesis of PbSe nanocrystals and the ligand exchange procedure. Section C is the nanowires growth and discusses the two methods used in growing the vertically-aligned Si nanowires, which are electroless etching and nanosphere lithography. The last part in this chapter is section D: device fabrication and will discuss the main fabrication techniques, which are standard optical photolithography, etching, and metallization.

### **B. Nanocrystals Growth**

#### Synthesis of PbSe Nanocrystals

The PbSe nanocrystals were synthesized by using hot injection technique, which involves mixing the precursors at high temperature under inert gas atmosphere. The growth reaction time will be varied depending on the desired diameter of the nanocrystals. Figure 2.1 shows a sketch of the synthesis setup which consists of a three-neck flask that contains the growth solution. A thermocouple is connected to a temperature controller and is used to sense the actual temperature

of the growth solution. The middle neck is connected to a Schlenk line condenser that supplies the  $N_2$  gas to the flask and the third neck is sealed with a rubber stopper. The three-neck flask is placed on a heating mantle that heats the growth solution to the desired temperature. Also a magnetic stirrer is placed inside the growth solution to agitate and mix the solution. After the synthesis is completed, the growth solution is quenched by placing the three-neck flask inside a water bath. This is important to reduce the variation in the diameter of the grown nanocrystals.

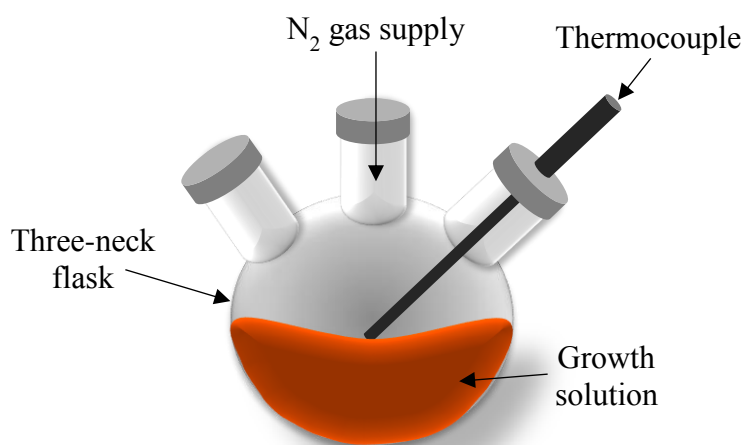


Figure 2.1 Sketch of the synthesis setup for growing the nanocrystals.

The synthesis procedure of PbSe nanocrystals was adopted from previous report with slight modifications to obtain nanomaterials with desired optical properties [44]. The modifications include: the amounts of the precursors, injection temperature, and the reaction time. First, the selenium precursor was prepared inside a glove box by dissolving 4 mmol (0.315 g) of selenium powder inside a mixture of 4 mL of n-trioctylphosphine (n-TOP) and 30  $\mu$ L of diphenylphosphine. The diphenylphosphine was used to increase the yield of the nanocrystals. Then the selenium mixture was left overnight for stirring at temperature of 60  $^{\circ}$ C. Second, the lead precursor was prepared by dissolving 1 mmol (0.223 g) of lead oxide (PbO) in 1.052 mL of

oleic acid and 5.3 mL of 1-octadecene (ODE) inside 50 mL three-neck flask. The lead precursor was gradually heated to a temperature of 140 °C. Once the lead oxide was dissolved the color of the mixture becomes slight yellow. Afterwards, the selenium was rapidly injected into the three-neck flask. This will result in changing the color of the reaction solution into dark brown. The nanocrystals were grown between 20 to 40 seconds after the injection. Finally, the synthesized nanocrystals were purified by adding acetone and centrifuging the mixture at speed of 6000 rev/min for 10 min. The synthesis procedure is summarized in figure 2.2.

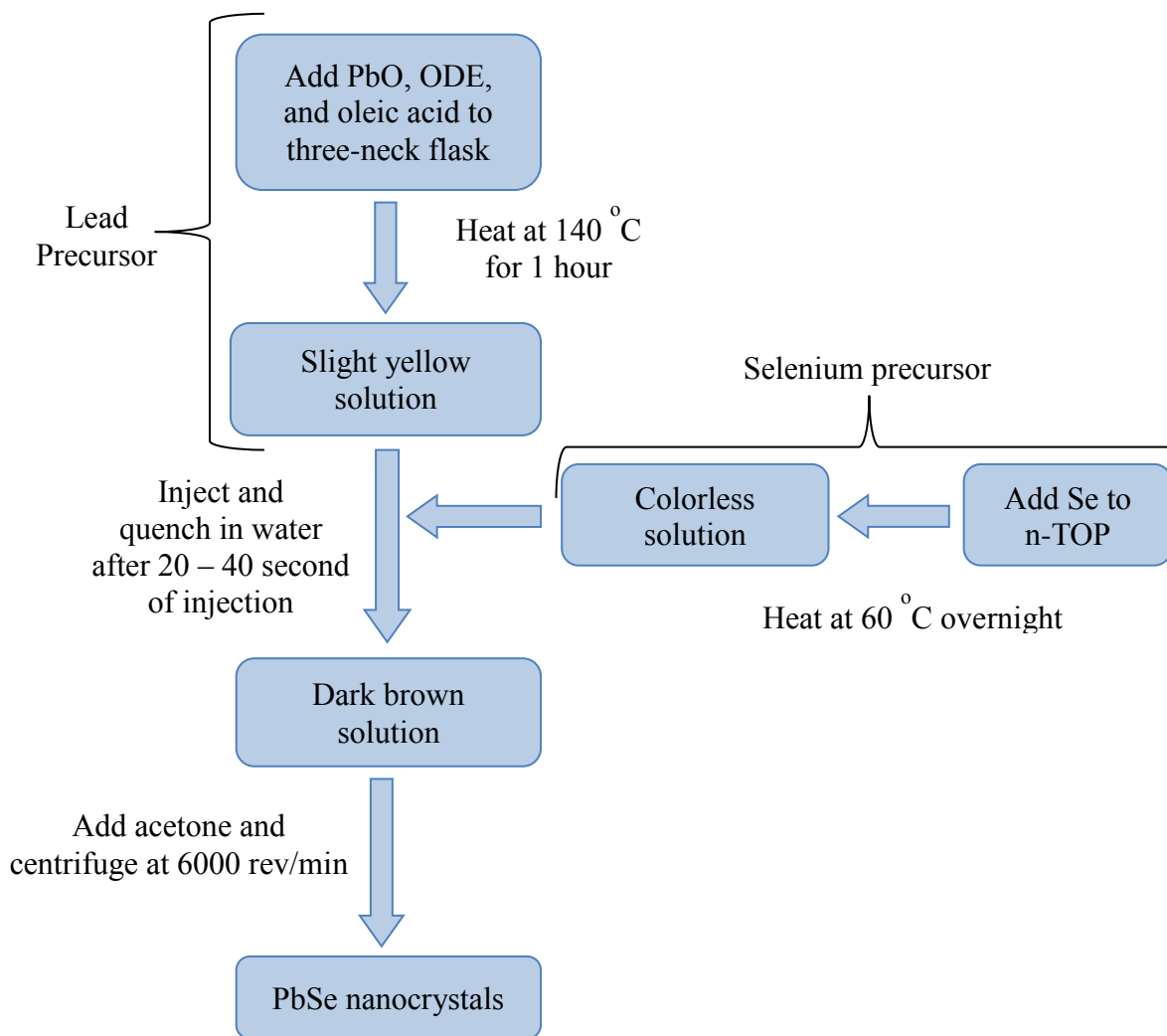


Figure 2.2 Synthesis procedure of the PbSe nanocrystals.



### Ligand Exchange Procedure:

After the nanocrystals were synthesized and purified, ligand exchange was performed on the synthesized nanocrystals to replace the original insulator ligands (oleic acid) with more conducting ligands. In this research, new ligands, such as, 1,2-ethanedithiol (EDT) and mercaptoacetic acid (MAA), were used to cap the synthesized PbSe nanocrystals. The effect of the new ligands on the electrical properties of the near-infrared photodetectors was investigated and the results will be presented in chapter 4, section B of this dissertation.

To cap the PbSe nanocrystals with the MAA ligands, the purified nanocrystals were dispersed in an excess solution amount of MAA and vigorously stirred inside glove box and under nitrogen gas atmosphere at temperature of 70 °C. The nanocrystals were left stirring inside the solution for two days to ensure maximum amount of the oleic acid was replaced with the MAA ligands. After the ligands exchange was performed, the PbSe nanocrystals are purified again with acetone and dried under vacuum overnight to evaporate the solutions. The final product of the nanocrystals was suspended in chloroform for future processing.

Ligand exchange with EDT can be performed by first spin coating the dispersed PbSe nanocrystals on a glass substrate [78]. The concentration of the dispersed PbSe nanocrystals is 55 mg/ml and the spin coating speed is 3000 rev/min. After the suspension solution was evaporated, the substrate was dipped inside 0.1 M EDT diluted in acetonitrile for several minutes to replace the original insulating, which is oleic acid ligands, and to reduce the spacing between adjacent nanocrystals. The dip coating process can be repeated several times to ensure full exchange of the oleic acid. The dip coating was done by using a dip coater. It is noted that the EDT smell is irritating and therefore extra caution should be taken.

## C. Nanowires Growth

### Metal-assisted Wet Etching

The metal-assisted wet etching is a top-down etching approach and is based on coating the surface of Si with noble metals, like Au and Ag, that will catalyze etching the surface of Si [59]. In this process, the area of Si that is covered with the metal will be etched in a faster rate as compared to other areas without noble metal coverage. Typically, the wet etchant consists of hydrofluoric (HF) acid and hydrogen peroxide ( $H_2O_2$ ). On the other hand, the use of less electronegative metal than Si, like chromium (Cr), will block this catalytic etching and therefore can be used as a hard mask to grow the nanowires in specific regions [79].

In metal-assisted wet etching, the surface of Si underneath the metal catalyst has higher concentration of holes ( $h^+$ ) [80]. This is because holes are injected either from the metal into the Si or electrons are transferred from the Si into the metal catalyst. As a result to the higher concentration of holes, oxidation and dissolution of Si will occur under the metals, as shown in figure 2.3. In other words, the metal will spare the Si with the holes necessary to complete the reaction inside the HF acid and Si will be lost as  $H_2SiF_6$ . The movement of the metal catalyst over the surface of the Si will affect the morphology of the etched surface.

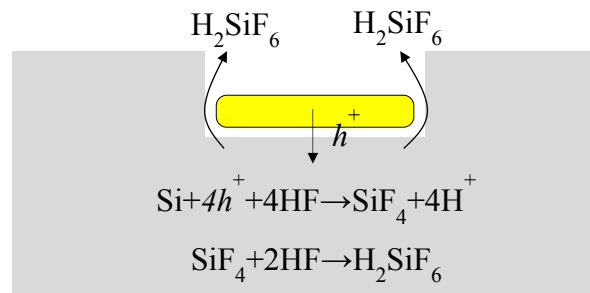


Figure 2.3 Mechanism of metal-assisted wet etching of Si in HF acid.

## Electroless Etching

Electroless etching approach is based on metal-assisted wet etching. It was widely used for growing vertically-aligned Si nanowires for its low cost and less complexity. The process of electroless etching is based on coating the surface of Si substrate with silver ions,  $\text{Ag}^+$  [81], [82]. And then etching the surface of Si by immersing it in an etchant containing HF acid and  $\text{H}_2\text{O}_2$ . The etching duration will determine the length of the grown nanowires. However controlling the diameters of the Si nanowires grown using this approach is difficult. From literature, the diameter of the nanowires grown using electroless etching can vary in the range between 50 to 150 nm [82]. To have a precise control over the diameter of the nanowires, other techniques based on metal-assisted wet should be used like: anodic aluminum oxide and nanosphere lithography [63], [79]. Undoped Si substrate with resistivity  $> 6000 \Omega\cdot\text{cm}$  was used in the fabrication of the Si nanowires. The use of intrinsic Si is to lower the dark current of the devices that are based on the grown Si nanowires.

The double polished undoped Si substrate was first cut into 1 x 1 cm samples. And then the samples were immersed in a mixture containing  $\text{H}_2\text{SO}_4(97\%):\text{H}_2\text{O}_2(35\%)$  with a volume ratio of 3:1 for 10 minutes at  $100^\circ\text{C}$  to clean the surface contamination. Afterwards, the samples were dipped in a solution of 5% HF acid for three minutes to strip the native oxide layer. Then the cleaned Si samples were coated with  $\text{Ag}^+$  by placing it in a solution of 4.8 M of HF and 0.005 M of  $\text{AgNO}_3$  under stirring for one minute. Next, the coated samples were immersed in an etchant containing 4.8 M of HF and 0.4 M of  $\text{H}_2\text{O}_2$  for 40 minutes to obtain nanowires with a length of 3  $\mu\text{m}$ . The remaining Ag particles were removed by using a diluted nitric acid  $\text{HNO}_3$ . The procedure of growing Si nanowires using electroless etching is summarized in figure 2.4.

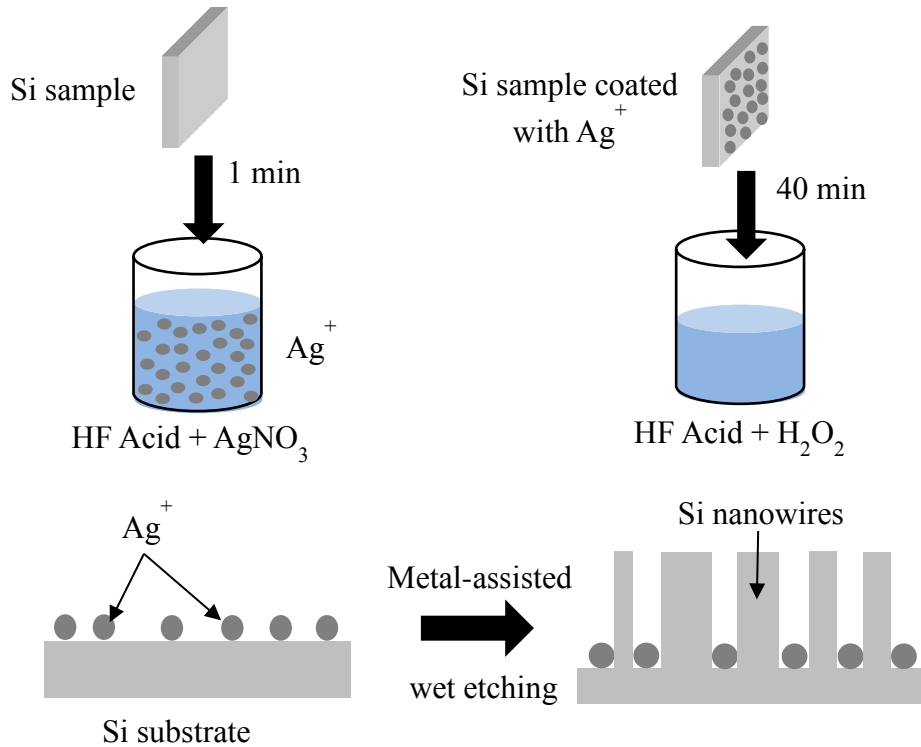


Figure 2.4 Growth of Si nanowires using electroless etching.

### Nanosphere Lithography

This method is used to grow vertically-aligned Si nanowires with controlled aspect ratio; diameter and length. It is based on coating the surface of Si with polystyrene nanospheres and then applying O<sub>2</sub> plasma etching using reactive ion etching (RIE) [58], [66]. The O<sub>2</sub> plasma is used to transform the close-packed nanospheres into none close-packed surface and to reduce the nanospheres diameter to the desired value which will determine the diameter of the Si nanowires. Afterwards, noble metal will be deposited on the patterned surface and metal-assisted wet etching will be performed to grow the Si nanowires. Finally, the residuals of the metal and the nanospheres will be removed. The nanosphere lithography procedure is summarized in figure 2.5.

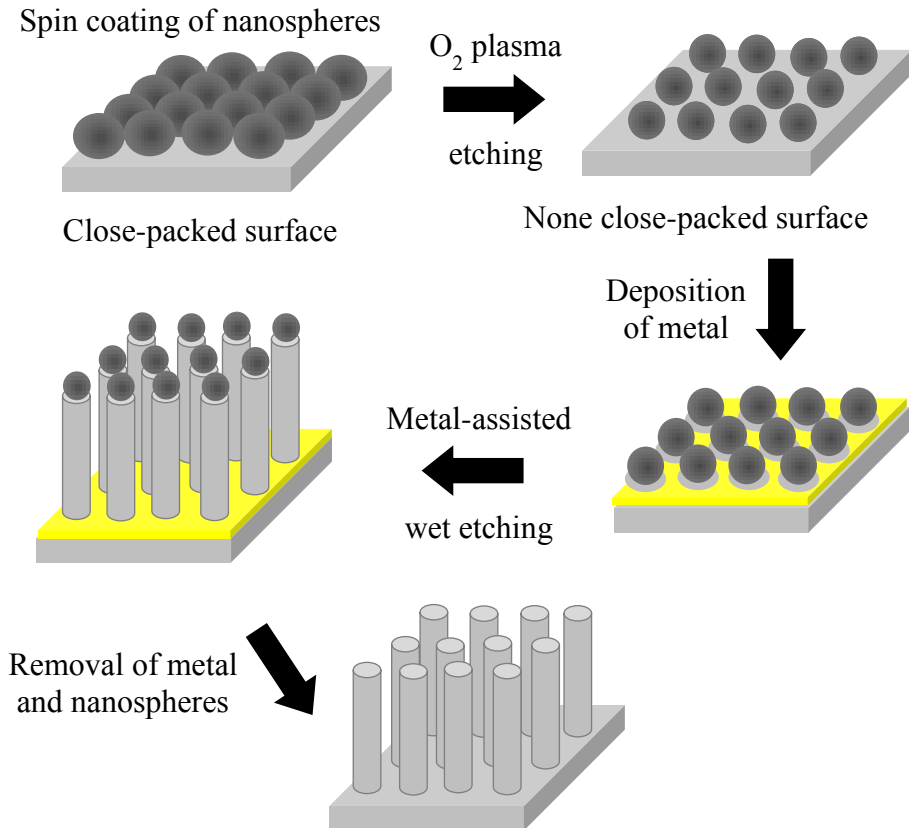


Figure 2.5 Growth of Si nanowires using nanosphere lithography.

In this procedure, the Si samples were cleaned using  $\text{NH}_3(70\%)/\text{H}_2\text{O}_2(30\%)/\text{H}_2\text{O}$  with volume ratio of 1:1:5 for 40 minutes at 100 °C. This cleaning process with ammonia is important to transform the surface of the Si sample into hydrophilic. Then polystyrene nanospheres with average diameter of 500 nm were spin-coated on the surface at speed of 3000 rev/min. The polystyrene nanospheres were purchased from Phosphorex Inc. The concentrated nanospheres were diluted by adding ethanol with volume ratio of 1:3. Once the nanospheres are coated on the surface, blue and green light reflections are obtained from the coated surface. Following the spin coating, the polystyrene nanospheres were etched isotopically using  $\text{O}_2$  plasma inside ICP-RIE (inductive coupled plasma-RIE). In the following is the etching parameters: RF power of 50 W,

ICP power 30 W, O<sub>2</sub> flow rate 50 sccm, chamber pressure of 100 mTorr, and time 20-25 minutes. The etching was performed by using Trion Minilock Phantom III ICP-RIE.

Once the none close-packed surface of the nanospheres is obtained, either Au or Ag with thickness of 15 and 40 nm, respectively was evaporated on the surface using electron-beam evaporator. Then the sample was wet etched using a solution containing 5 mL of 49% of HF acid, 1 ml of 30% H<sub>2</sub>O<sub>2</sub>, and 27 mL of H<sub>2</sub>O. The wet etching time will determine length of the Si nanowires. Finally, the nanospheres residuals were removed by immersing the sample in toluene for 10 minutes and the metal residuals were etched by using boiling aqua regia for five minutes. The aqua regia was prepared by mixing 5 mL of 40% HCl with 1 mL of 70% of HNO<sub>3</sub> then boiling the mixture at temperature of 80 °C. Once the aqua regia starts boiling, its color will change into slight red.

#### **D. Device Fabrication**

##### Optical Photolithography

In this research, patterning with photoresist was performed using standard optical photolithography procedures inside class-100 cleanroom. The photoresist was used as a mask for metallization or etching, which is necessary during the fabrication of devices. This requires designing a photomask with the desired shapes and dimensions of the patterns. The photomask was designed using AutoCAD software and then the design was sent to Advanced Reproduction Corporations for manufacturing. The designed photomask had two opposite tones: dark data-clear field and clear data-dark field. The photomask is manufactured on a soda lime glass substrate with a thickness of 0.09 inch and chrome as the bottom coating. The size of the photomask is 4 x 4 inch.

The optical photolithography procedure was performed by first spin coating of photoresist on a substrate at speed of 7000 rev/min for one minute. Positive photoresist with type of A4330 was used in the fabrication of all devices in this work. Prior to the spin coating of the photoresist, the substrates were cleaned using acetone, methanol, isopropyl alcohol, and DI water and then dried with nitrogen purge. After a uniform photoresist film with thickness around 2  $\mu\text{m}$  was formed on the substrate, the photoresist film was soft baked at temperature of 110  $^{\circ}\text{C}$  for three minutes to evaporate the solvent and adhere the photoresist to the substrate. Then the substrate was placed on the mask aligner and exposed at to UV light with intensity of 20  $\text{mW}/\text{cm}^2$  for five seconds using the designed photomask. Afterwards, the exposed part of the photoresist was developed by using AZ400K developer for 25 to 40 seconds. The developer was purchased from Integrated Micro Materials. The developer was diluted with DI water at a ratio of 1:3 to reduce its concentration. Before the substrate was loaded into the electron-beam for the evaporation of metals, the photoresist pattern was examined by using a microscope.

After patterning the sample with photoresist, metal will be deposited on the patterned substrate using Angstrom Nexdep electron-beam evaporator at pressure of  $1.5 \times 10^{-7}$  torr and room-temperature. The thickness of the deposited metal varies between 1 to 50 nm. The electron-beam evaporator provides a way to deposit high quality of metal films with a precise control over the deposition rate, however it has poor step coverage. During the metal deposition, the substrate was rotated at a speed of 20 rev/min to ensure uniform thickness in the deposited metal thin-film. In this research, different metals were used, such as Ti, Au, Ag, and Cr, to serve as a contact, adhesive layer, or a hard mask. After the metal was deposited, lift-off is performed by using acetone or photoresist stripper PRS-1000 purchased from J. T. Baker. The samples are gently agitated during the photoresist stripping by bubbling over the substrate using a pipette.

## Processing of Devices

The self-powered photodetectors based on asymmetrical interdigital contacts were fabricated by using two subsequent steps of patterning and deposition. The photomask that is used in the fabrication has two opposite tones that are aligned with each other. The first mask was used to create a comb-like shape of Au thin-film. The width of the Au electrodes is  $50\ \mu\text{m}$  with a spacing of  $150\ \mu\text{m}$  between the electrodes. Next, the second mask was applied to cover the Au electrodes with photoresist plus a  $50\ \mu\text{m}$  of the spacing between the Au electrodes from both sides. And then the second metal, either Ti or Ag, was deposited and lift-off was performed. This will create two asymmetrical interdigital electrodes spaced by a channel with width of  $50\ \mu\text{m}$ . Figure 2.6 shows microscopic images of the device after each fabrication steps. In this research, asymmetrical interdigital electrodes with different electrode spacing were fabricated, such as, 5, 10, 20, and  $50\ \mu\text{m}$ , as shown in figures 2.7 (a) and (b). Image of the markers that are used in the alignment between the first and the second masks is shown in figure 2.7 (c).

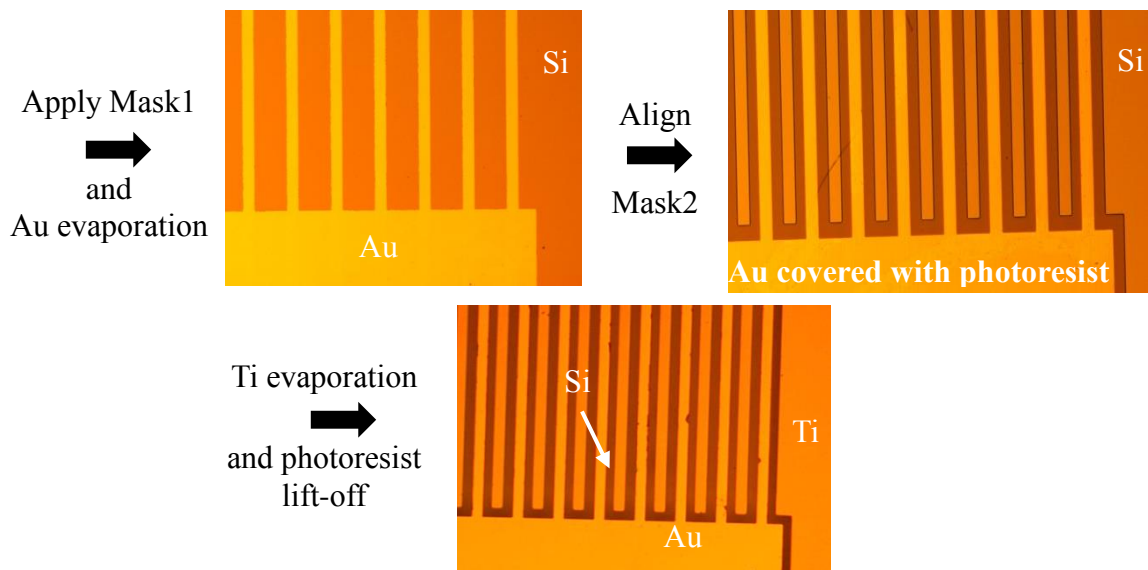


Figure 2.6 Microscopic images of the self-powered photodetector after each fabrication step.



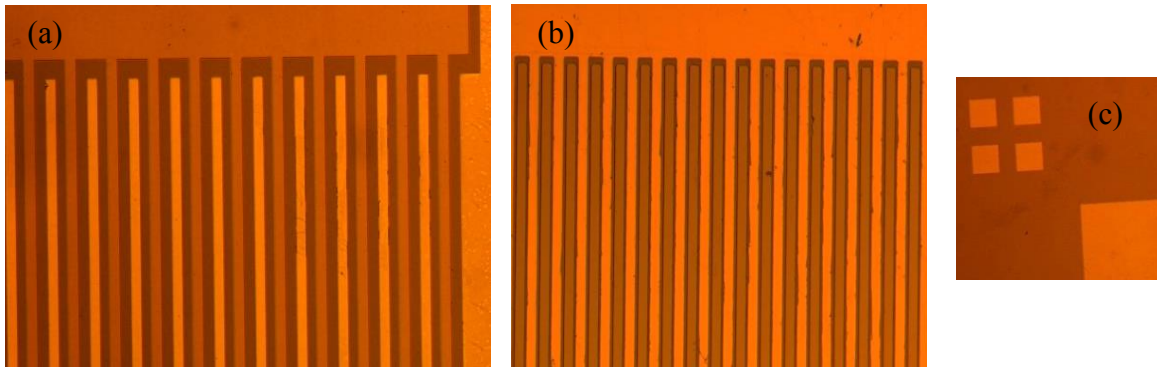


Figure 2.7 Microscopic images of asymmetrical interdigital electrodes spaced by a channel with width of (a) 50  $\mu\text{m}$  and (b) 5  $\mu\text{m}$ . (c) Image of the markers used in the alignment between the first mask and the second mask.

The structure of the self-powered photodetector based on Si nanowires consists of planar Au and Ti interdigital electrodes with Si nanowires integrated vertically between the Au/Ti electrodes. The electrodes are spaced by a channel with width of 50  $\mu\text{m}$ . First, Si fingers with thickness and width of 3 and 50  $\mu\text{m}$ , respectively, are prepared using wet etching and patterning with photoresist. The wet etchant consists of a mixture of HF(49%):HNO<sub>3</sub>(70%):H<sub>2</sub>O with a volume ratio of 6:10:40. The sample was immersed in the etchant for 45 minutes to obtain Si fingers with thickness of 3  $\mu\text{m}$ . The etch profile of the obtained Si fingers is shown in figure 2.8 and was measured by using Taylor Hobson optical profiler.

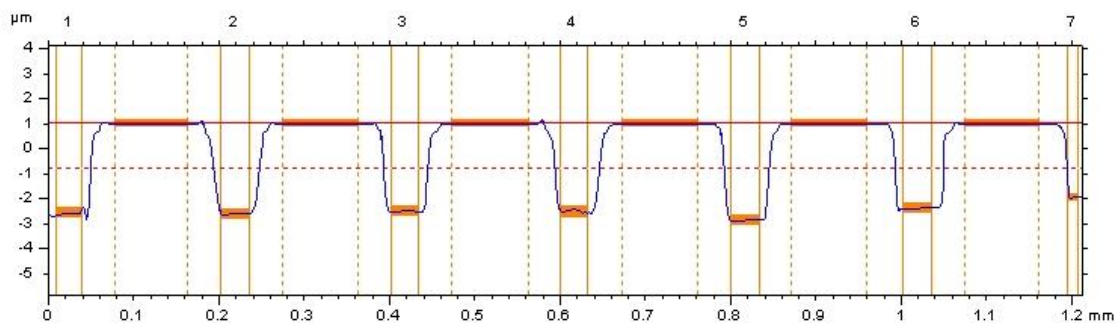


Figure 2.8 Etch profile of the prepared Si fingers using wet etching.

Second, the formed Si fingers were covered again with photoresist then Cr with thickness of 70 nm was deposited. The use of Cr is to protect the areas between the Si fingers where the final interdigital electrodes will be deposited. After stripping the photoresist, the Si fingers were transformed into nanowires using the electroless etching that was described previously in figure 2.4. And then the residuals of Cr were etched using chromium etchant. Finally, Au and Ti electrodes with thicknesses of 30 nm were deposited between the prepared Si nanowires by following the procedure presented in figure 2.6. The fabrication steps of the device based on Si nanowires are shown in figure 2.9.

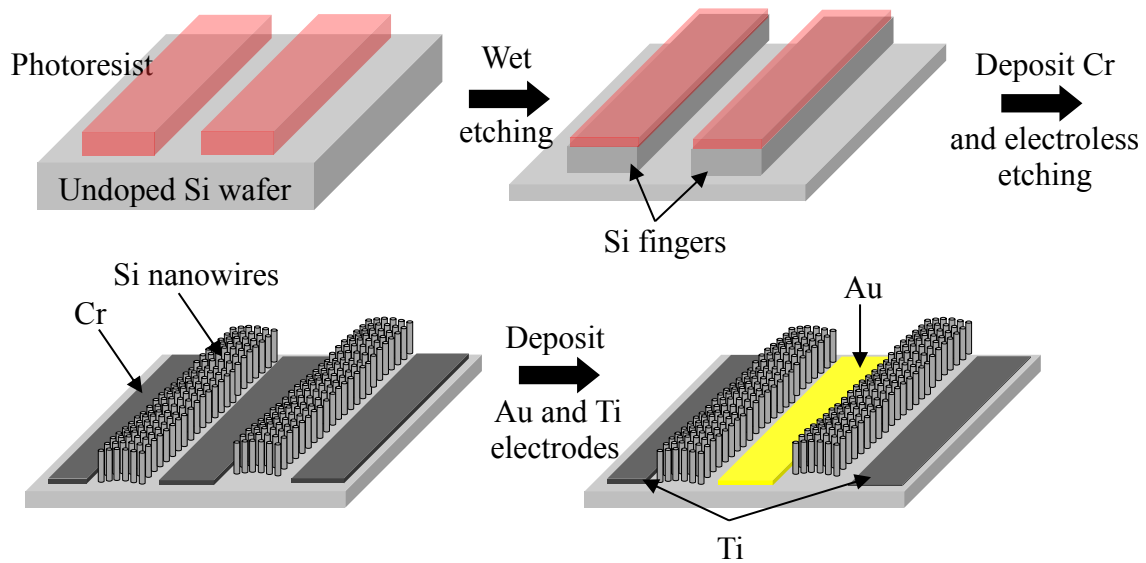


Figure 2.9 Fabrication steps of the self-powered photodetector based on Si nanowires.

On the other hand, the uncooled near-infrared photodetectors based on PbSe nanocrystals were fabricated by preparing symmetrical interdigital electrodes on a glass substrate. The interdigital electrodes are made of Ti adhesive layer with thickness of 30 nm followed by Au top contact with thickness of 50 nm. A glass substrate was used to insure that the electrodes are not electrically connected. Prior to the fabrication, the glass substrate was cleaned by immersing it in

5% HCl acid for three minutes and then washed by acetone, methanol, isopropyl and DI water. Interdigital electrodes with different electrode spacing were fabricated,  $d = 10, 20,$  and  $50 \mu\text{m}$ . All the interdigital electrodes had the same ratio of electrode width to electrode spacing,  $w = 2d$ . After the electrodes were prepared, the dispersed PbSe nanocrystals were spin-coated on the interdigital electrodes at speed of 1500 rev/min for one minute. The optimum concentration of the dispersed PbSe nanocrystals in chloroform was found to be 55 mg/mL. Afterwards, gold wires were bonded to the interdigital electrode to connect the device to external circuitry for characterization. The schematic of the uncooled near-infrared photodetector based on PbSe nanocrystals is shown in figure 2.10. With this structure, it is necessary to apply a voltage bias to create an electric field between the electrodes that will cause the drift of the photo-excited carrier.

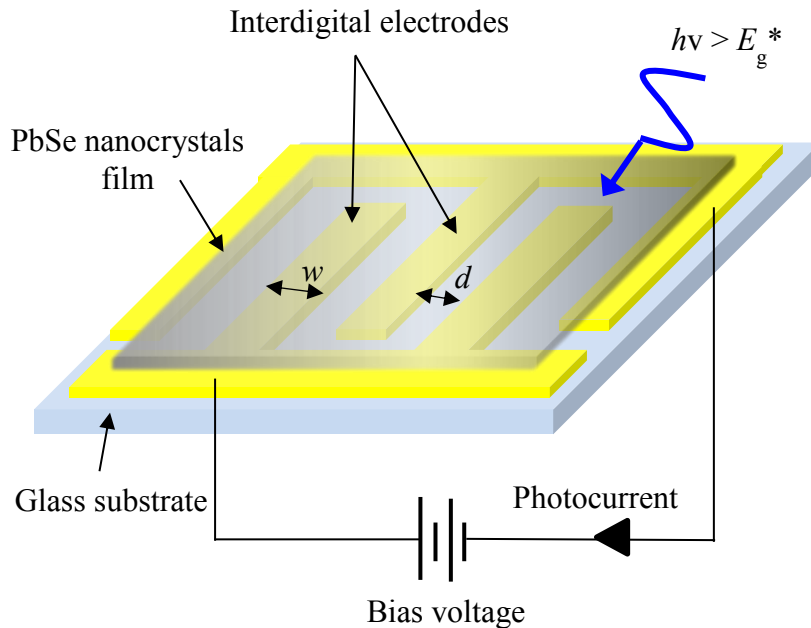


Figure 2.10 Schematic of the uncooled near-infrared photodetector based on PbSe nanocrystals.

### **III. Characterization Techniques**

#### **A. Introduction**

This chapter will present the characterization techniques that are used to extract the optical and electrical properties of the grown nanomaterials and the fabricated devices. The optical properties of the nanocrystals were measured by using the optical absorbance and the photoluminescence. For the optoelectronic devices, the optical properties were extracted by measuring the spectral response and the external quantum efficiency. The electrical properties of the devices were investigated by measuring the current-voltage characteristics under both dark and illumination conditions. Section B will discuss the various optical characterization techniques used in this research and section C will discuss the electrical characterization.

#### **B. Optical Characterization**

##### Optical Absorbance

The absorbance spectrum of the synthesized nanocrystals was measured in the ultra-violet, visible, and near-infrared regions by using Cary 500 UV-Vis-NIR spectrophotometer. This spectrometer can measure the optical absorbance of materials within the wavelength range of 175 to 3300 nm. The absorbance of the nanocrystals was measured while the nanocrystals were dispersed in a solvent (chloroform). The dispersed nanocrystals were placed inside a quartz cuvette during the absorbance measurement. Before the measurement, the absorbance spectrum was corrected by measuring the absorbance of the chloroform and setting it as the baseline. Figure 3.1 shows a sketch of the setup used in the measurement of the optical absorbance. The absorbance was measured for nanocrystals synthesized at different growth time to investigate the change in the size of the nanocrystals.

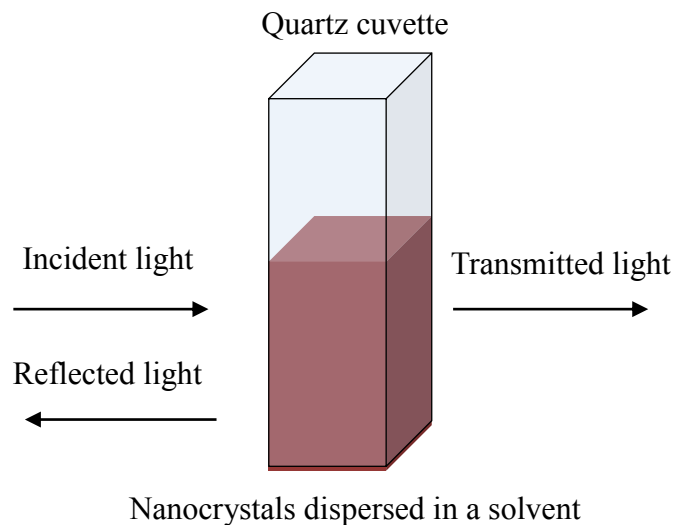


Figure 3.1 Measurement of the optical absorbance of the dispersed nanocrystals.

As the light travels through a medium, part of the energy is lost by the absorbance or the reflectance of the incident light. The optical absorbance ( $A$ ) in arbitrary units can be found using Beer-Lambert law:

$$A = \text{Log}(1/T) = \text{Log}(I_o / I) = \alpha d \quad (3.1)$$

where  $T$  is the transmittance,  $I$  and  $I_o$  are the intensities of the incident and transmitted light, respectively,  $\alpha$  is the absorption coefficient, and  $d$  is the optical path length. It is noted, that the reflected photons in this setup are not measured and therefore integrated sphere should be used in order to measure the reflectance from the surface. When the energy of the incident photons is less than the bandgap of the nanocrystals, the nanocrystals will not absorb the incident photons and they are either reflected or transmitted. On the other hand, when photons with energy higher than the bandgap of the nanocrystals are radiated, they will be absorbed and electrons are excited inside the nanocrystals. The excited electrons perform an interband transition from the valence

band into the conduction band, which will result in an excitonic peak in the obtained absorbance spectrum.

In Carry 500, the wavelengths of incident radiations are varied by using a double monochromator and the intensities of both the incident and transmitted light are recorded at each wavelength. Double monochromator means that two mechanical diffraction gratings are used; one is dedicated for the near-infrared region and the other is for the visible region. Gratings are used to diffract the incident light and the wavelength of the diffracted light depends on the diffraction angle, as depicted in figure 3.2. The monochromatic light will be focused into the sample using a focusing mirror. As the diffraction grating rotates, the wavelength of the monochromatic light incident on the sample will change.

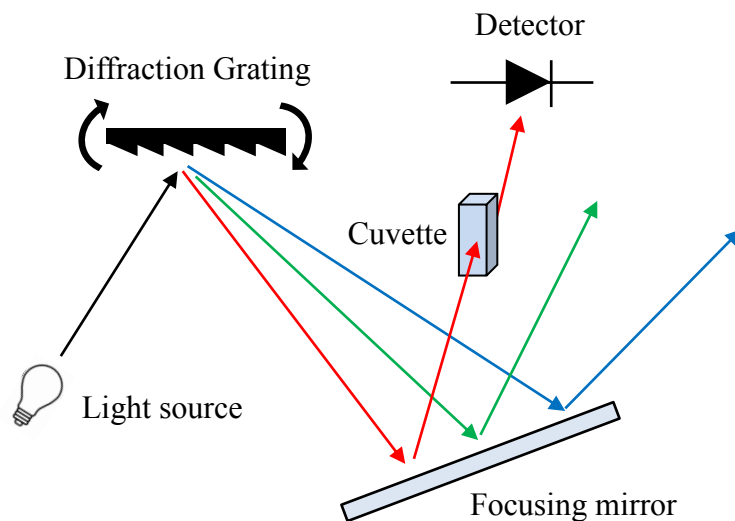


Figure 3.2 Process of producing monochromatic light using diffraction gratings.

### Photoluminescence

The photoluminescence (PL) is a reversed process as compared to the optical absorbance. It is based on the emission of photons that occurs when the excited electrons decay back from the

conduction band into the valence band. The PL spectrum of the nanocrystals was measured by using a Bomem DA8 Fourier transform infrared (FTIR) spectrometer. The PL spectrum of the nanocrystals was measured at room-temperature after depositing the dispersed nanocrystals on a glass substrate and evaporating the solvent.

In the PL measurements, a red laser with energy higher than the bandgap energy of the nanocrystals is used as the excitation source. The emitted photons from the nanocrystals are scattered back into the FTIR spectrometer and are detected by using a silicon avalanche detector or InSb detector. The InSb detector is cooled down to 77 K using liquid nitrogen to reduce the thermal noise. The sample was placed inside a Janis cryostat, which can be connected to a temperature controller. The PL intensity of the nanocrystals was measured in arbitrary units and plotted as function of wavelength. From the PL spectrum different information can be extracted, like the effective bandgap and the size distribution of the nanocrystals. The PL setup used in this research is shown in figure 3.3.

The Bomem FTIR spectrometer is based on Michelson interferometer and consists of a beam splitter and scanning and movable mirrors. In this FTIR spectrometer, the PL signal emitted from the sample is split into two beams that will be directed into the scanning and the fixed mirrors. The two beams will reflect from the mirrors and are combined again on the beam splitter. This will create an interference since the beams have traveled different optical paths and experienced different phase changes. For example, if the beams were  $180^\circ$  out of phase, the recombined beam will be zero. As the position of the scanning mirror changes, the interference changes accordingly and it is transformed into the spatial coordinate by using Fourier transform. The Fourier transform is performed by a computer and the PL spectrum will be plotted as function of wavelength.

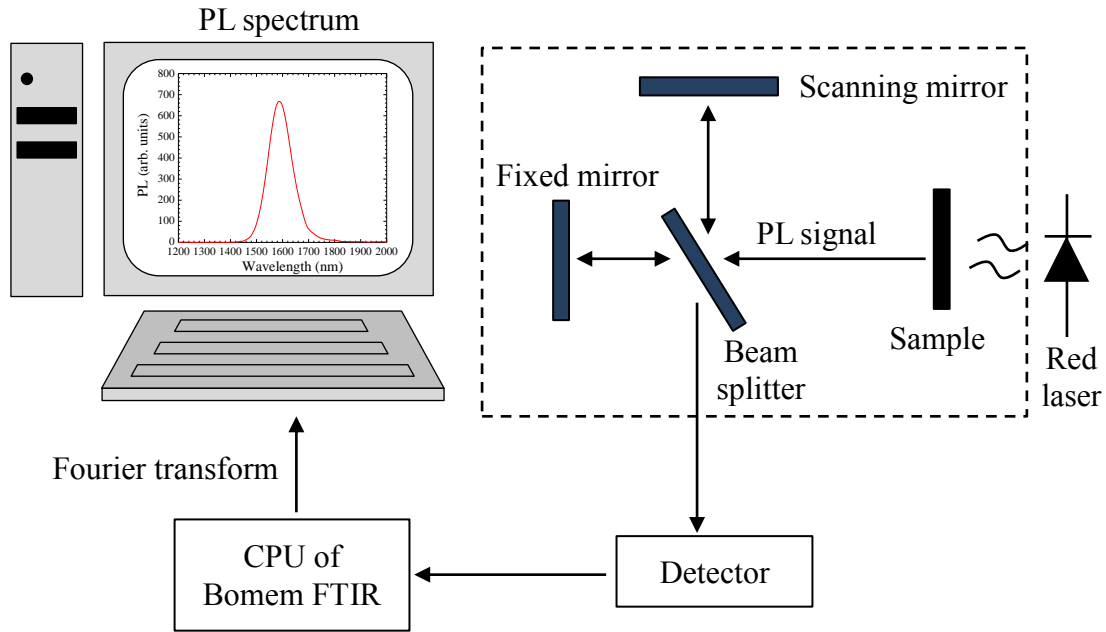


Figure 3.3 Sketch of the PL measurement setup using Bomem FTIR.

### Spectral Response

Spectral response, also known as photoresponse, is an optical characterization of optoelectronic devices and it is defined as the ratio of the light-generated current to the incident optical power. The spectral response was measured by using Bruker 125 HR FTIR spectrometer in conjunction with Keithley 428 current preamplifier. The preamplifier can enable biasing the devices at different voltages during the measurement. The measured spectral response is expressed in arbitrary units and plotted as function of wavelength. Essentially, the spectral response of devices resembles the absorbance spectrum of the material. This is because no photocurrent is generated when the incident light energy is less than the bandgap of the material used in the device. Therefore the spectral response is limited at low incident light energy by the bandgap of the semiconductors. And it is limited at high incident light energy by the front surface recombination, in the case of photovoltaic devices.



Similar to the Bomem FTIR, the Bruker consists of a beam splitter, a scanning mirror and a fixed mirror. The beam splitter splits the beam coming from the quartz halogen source into two separate beams. The split beams will travel different paths and are reflected from the fixed and the scanning mirrors. When the reflected beams are recombined on the beam splitter, interference will occur due to the difference in the traveled optical paths. The recombined beam will be directed into the device and will be used as the illumination source. The position of the movable mirror is tracked by using a HeNe laser. The devices were placed inside Janis cryostat. The quartz halogen source is used as a broadband light source that covers the spectral range between 400 to 2000 nm. Quartz TiO<sub>2</sub> coated beam splitter is used in the FTIR spectroscopy and it causes decay in the spectral response spectrum in the energy region higher than 1.67 eV. The spectral response measurement was performed under vacuum of 10<sup>-5</sup> Torr using an Edward roughing pump. Figure 3.4 shows a sketch of the Bruker FTIR spectroscopy. The size of the beam illuminating the device was chosen to cover the entire area of the device and oval beam shape was used. The Bruker FTIR spectrometer was calibrated using a built-in avalanche Si photodiode.

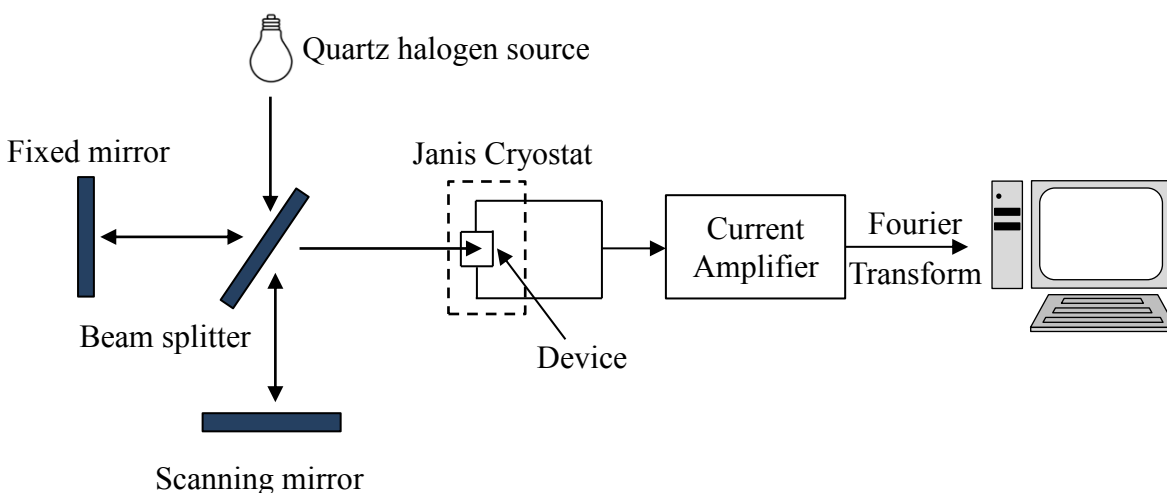


Figure 3.4 Sketch of the spectral response measurement using Bruker FTIR.

## External Quantum Efficiency

The external quantum efficiency (EQE) is defined as ratio of the collected charges to the number of incident photons. The EQE in the spectral range between 380 to 1300 nm was measured by using a Newport Oriel IQE-200. This system is based on using 250 W QTH lamp as the illumination source. The system can also measure the internal quantum efficiency; ratio between collected electrons and absorbed photons. In Oriel spectrometer, the light is chopped using an optical chopper with frequency of 30 Hz to reduce the flicker noise and then is dispersed through monochromator. The diffracted light from the monochromator is split by using a beam splitter into three beams: one is incident on the device to be tested and the two other beams are delivered into two different pre-calibrated detectors. One of the detectors is the reflectance detector and will measure the reflected photons from the surface of the device, which is only used in the case of internal quantum efficiency measurement. And the other detector is the reference detector and will measure the intensity of the incident light, which is used to determine the number of incident photons. Therefore, the three-way beam splitter is used to direct the light simultaneously into the device and to the two detectors. The device is connected to a lock-in amplifier to measure the output current. The external quantum efficiency is found by using the following equation:

$$EQE(\lambda) = \frac{hcI_{cell}(\lambda)}{e\lambda I_{ref}(\lambda)R(\lambda)} \quad (3.2)$$

where  $h$  is Planck's constant,  $c$  is the speed of the light,  $I_{cell}$  is the device output current, and  $I_{ref}$  and  $R$  are the current and the responsivity measured from the reference detector, respectively. A computer is used to control the monochromator, lock-in amplifier, and a multiplexer that is used for data acquisition from the two detectors and the lock-in amplifier, as shown in figure 3.5.

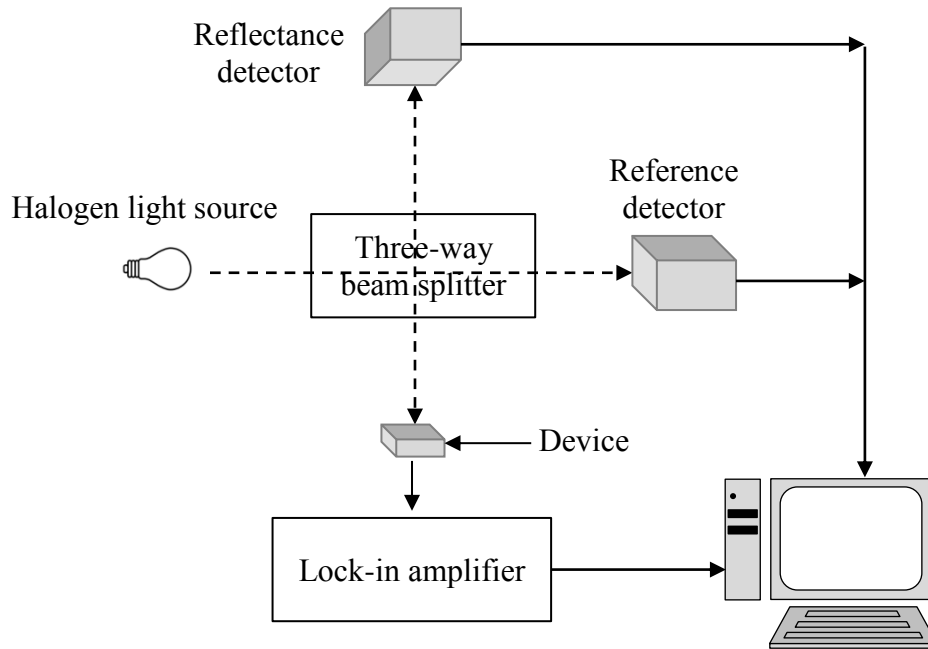


Figure 3.5 Setup of the EQE measurement.

### C. Electrical Characterizations

#### Current-Voltage Characteristics

The current-voltage ( $I$ - $V$ ) characteristics of the optoelectronic devices were extracted by using Keithley 4200 SCS semiconductor parameter analyzer. The dark current was measured while the device is placed inside a dark chamber. The photocurrent was measured under the illumination of a broadband light source that covers the wavelength spectral range between 360 and 1800 nm with a power density of  $100 \text{ mW/cm}^2$ . The light intensity is covering the entire area of the device and is calibrated using a reference solar cell from Newport Inc. This  $I$ - $V$  characterization system is based on applying a bias voltage and measuring the current simultaneously. The voltage can be swept between -15 to 15 V with an interval as low as 0.01 V. The bias voltage is applied through high resistive probes and the current is measured through

different measuring probes with lower resistance. In this four probe measurements, the error obtained in the  $I$ - $V$  measurement will be minimized.

### Photocurrent Map

Photocurrent map was used to plot the photocurrent of optoelectronic devices as function of the position of a focused light. The focused light will be swept over the device and used as the illumination source. This characterization was used particularly to confirm the optical enhancement based on hot electrons injections in Schottky thin-films. In this measurement, a red laser with wavelength of 632 nm and power of  $400 \mu\text{W}$  was swept over the thin-films at constant speed and the photocurrent was measured using the Keithley as function of time. The device was biased at constant voltage of 5 V and the red laser was focused by using a lens with numerical aperture of 0.55. The time in the x-axis was multiplied by the laser sweep speed to plot the photocurrent as function of position of the red laser. Figure 3.6 shows the schematic of the setup used in photocurrent map measurement.

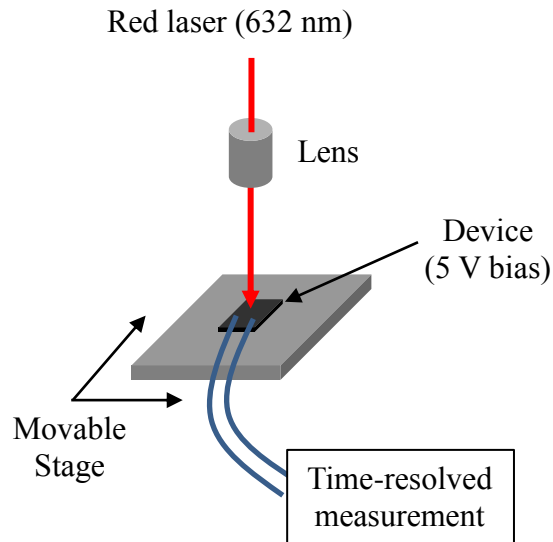


Figure 3.6 Setup of the photocurrent map measurement.

## **IV. Result and Discussion**

### **A. Introduction**

This chapter will discuss the main outcomes of the research conducted to investigate nanostructures for optoelectronic devices. The experimental results discussed in this chapter include the optical and electrical characterization of the nanomaterials and the devices. The nanomaterials were grown chemically in the lab to tune their optical characteristics and then were integrated with the metal contacts to form a high performance optoelectronic device. This chapter is divided into four sections: uncooled PbSe nanocrystals photodetector, self-powered photodetectors, photodetectors based on Si nanowires, and hot electrons in Au thin-films.

The first section will discuss the optical properties of the synthesized PbSe nanocrystals, the effect of ligand exchange, and the device optical and electrical performance. The results presented in this section were published in 2016 IEEE Sensors and IEEE Transaction on Nanotechnology [45], [83]. The second section will discuss the optimization and the performance of self-powered near-infrared photodetectors based on asymmetrical interdigital electrodes. The results presented in this section were published in IEEE Electron Device Letters [84]. The third section will discuss the characterization of vertically-aligned Si nanowires and their integration with asymmetrical interdigital electrodes. The results that report the enhancement on the performance of self-powered photodetector using Si nanowires were published in Applied Physics Letters [85]. Finally, the last section will discuss the utilization of hot electrons in thin-film Schottky barriers to enhance near-infrared detection. In this study, the effect of Au thin-films thickness was investigated along with the effect of adding Ti adhesive layer. All the results were published in IEEE Photonics Technology Letters [86].

## **B. PbSe Nanocrystals Photodetectors**

### Optical Properties

The optical absorption of the synthesized PbSe nanocrystals in the wavelength range between 200 to 2000 nm was measured by using Cary 500 UV-Vis. The absorbance spectrum in arbitrary units of the nanocrystals is plotted in figure 4.1 as function of wavelength. The absorbance spectrum was measured while the PbSe nanocrystals were dispersed in chloroform. Baseline correction was performed by measuring the absorbance of chloroform without nanocrystals suspension. It is noted that the PbSe nanocrystals were grown at temperature of 140 °C for 20 seconds after the injection of the selenium stock solution into the lead precursor.

As can be seen in figure 4.1, the absorption spectrum of the synthesized nanocrystals consists of four distinct excitonic peaks labeled: A1, A2, A3, and A4 and positioned at 0.8, 1.15, 1.5, and 2 eV, respectively. The third exciton has approximately twice the confinement energy of the first exciton, which is in consistency with the literature [87]. The optical absorption spectrum has an onset at wavelength of 1600 nm which corresponds to bandgap energy of 0.78 eV. These excitonic peaks result from the absorption of photons energy and the excitation of electrons between the discretized energy states, i.e. interband transitions. This behavior is caused by the extreme quantum confinement exhibited in the PbSe nanocrystals and the large Bohr exciton radius.

The peak labeled A1 results from the interband transition between the ground state in the valence band into the ground state in the conduction and it exhibits the strongest absorbance as compared to the other peaks. This is mainly because the oscillator strength accompanied with the ground-to-ground interband transition is the strongest. The oscillator strength is reduced for

interband transitions between larger energy states, which will cause weaker absorbance. A larger size of the nanocrystals will cause the excitonic peaks to occur at lower energy since the energy is inversely proportional to the square of the diameter of the nanocrystals.

By applying an electric field to the nanocrystals, a shift in the absorption spectrum will occur. Franz-Keldish theory allows predicting the magnitude of the electric field required to cause a certain energy shift in the absorption spectrum. The constant electric field results in the tunneling of the density of states into the fundamental bandgap, which allows photons with lower energies to be absorbed [46]. Therefore, an external applied voltage is expected to create a shift in the absorption spectrum which is known as a Stark's shift. A shift will be observed between the optical absorption of the nanocrystals and the spectral response of the device, as will be seen later in this section.

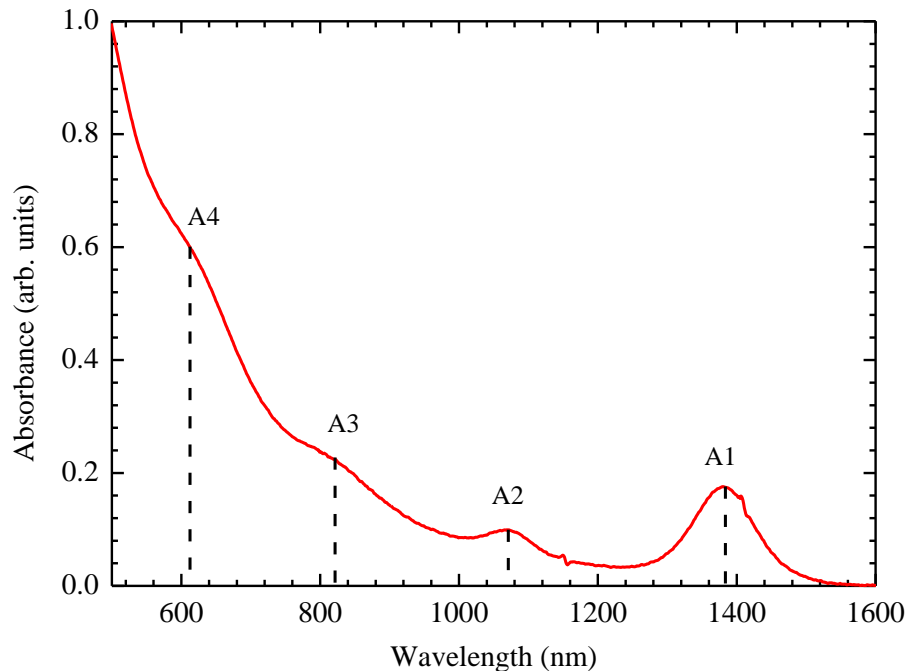


Figure 4.1 Absorbance spectra of the synthesized PbSe nanocrystals. Reprinted with permission from Nusir *et al* [45].

The optical absorbance and the photoluminescence (PL) spectra of the synthesized PbSe nanocrystals are plotted together versus wavelength in figure 4.2. Both spectra were measured at room-temperature. The absorbance spectrum was measured in the solution form while the nanocrystals were dispersed inside the solvent. The PL spectrum was measured in the solid form after depositing the nanocrystals on a glass substrate and evaporating the solvent. Inset of figure 4.2 shows a schematic of the interband transitions and the corresponding excitonic peaks. The strong excitonic peak labeled A1 is due to the ground-to-ground interband transition. The presented absorbance and PL results in figure 4.2 are for PbSe nanocrystals capped with oleic acid. The nanocrystals were purified with acetone three times before measuring the absorption and PL spectra.

As can be shown from the PL spectrum of the nanocrystals, it consists of a single and narrow peak centered at wavelength of 1600 nm. The full width at half maximum (FWHM) of the PL peak is 105 nm. This indicates that a single dominant size of nanocrystals was obtained and the size variation was minimized. The control over the size of the synthesized nanocrystals was obtained by using a modified synthesis procedure. In which the growth solution was rapidly quenched in a water bath after 20 seconds of injecting the selenium into the lead precursor. Furthermore, the temperature of the growth solution during the synthesis of the nanocrystals was held constant at 140 °C by wrapping the three-neck flask with thermal insulators.

The PL peak in figure 4.2 results only from the ground-to-ground interband transitions. However the position of the PL peak is shifted into a higher wavelength (lower energy) as compared to the first excitonic peak labeled A1. This can be attributed to the Stoke's shift especially not all of the absorbed photons energy are emitted, part of the energy is lost as vibration to lattice and the generation of phonons. This will result in a PL peak shifted to lower



energy as compared to the absorbance spectrum. Furthermore, the solid-state bandgap (PL) can be different from the solution-based bandgap (absorbance) due to the closer proximity of the dried nanocrystals, and thus greater potential for overlapping between wave functions.

From the results presented in figure 4.2, we conclude that high quantum confinement in the synthesized PbSe nanocrystals was obtained. Additionally, the size of the nanocrystals was tuned to cover most of the near-infrared spectral region. The bandgap of the nanocrystals can be further lowered by increasing the reaction time beyond 20 seconds. However in this research only nanocrystals with growth time of 20 seconds are used in the device fabrication since a further decrease in the bandgap energy is expected after the ligand exchange step.

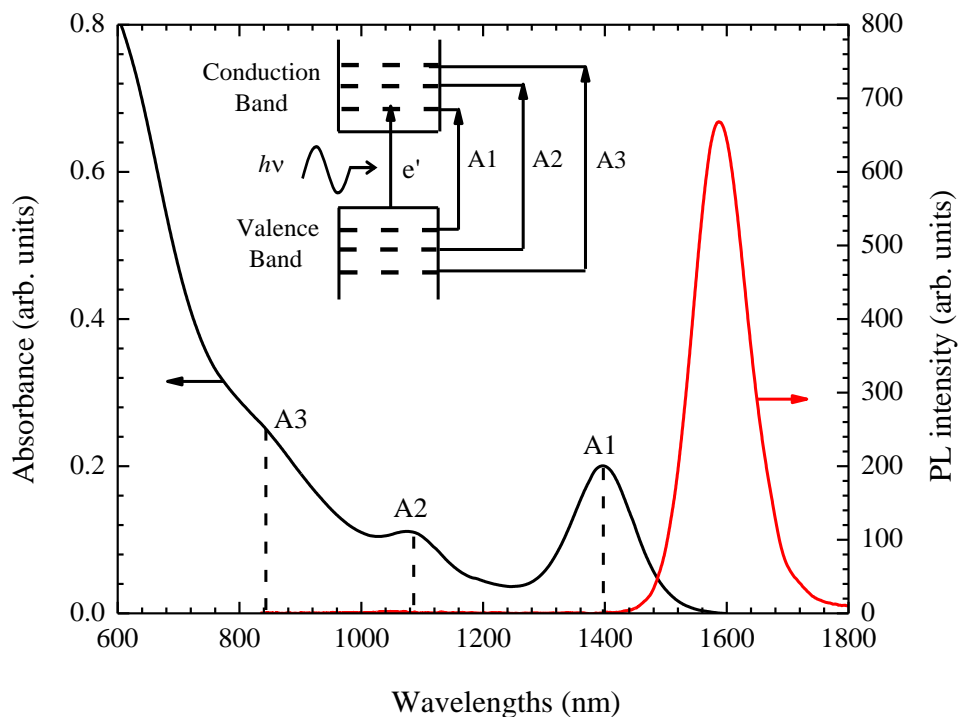


Figure 4.2 Absorbance and PL spectra of the PbSe nanocrystals at room-temperature (Inset: Schematic of the interband transition with the band structure of the nanocrystals). Reprinted with permission from Nusir *et al* [83].

The effect of increasing the growth reaction time on the size of the nanocrystals was investigated by synthesizing PbSe nanocrystals at different reaction times: 20 and 40 seconds. The absorbance spectra of the synthesized nanocrystals are plotted together in figure 4.3. By further increasing the growth time 20 seconds, the first excitonic peak exhibits a red shift of 400 nm to longer wavelength as indicated in figure 4.3. This is mainly due to the increase in the size of the synthesized nanocrystals caused by the longer reaction time. And as indicated in equation 1.2, the effective bandgap is inversely proportional to the square of the diameter of the nanocrystals. The first exciton energy can be used to estimate the diameter of the synthesized PbSe nanocrystals and it was found to be around 7 and 10 nm for reaction times of 20 and 40 seconds, respectively [41]. The spike at wavelength of 1690 nm is due the instability of the solvent (chloroform) that is used to disperse the nanocrystals.

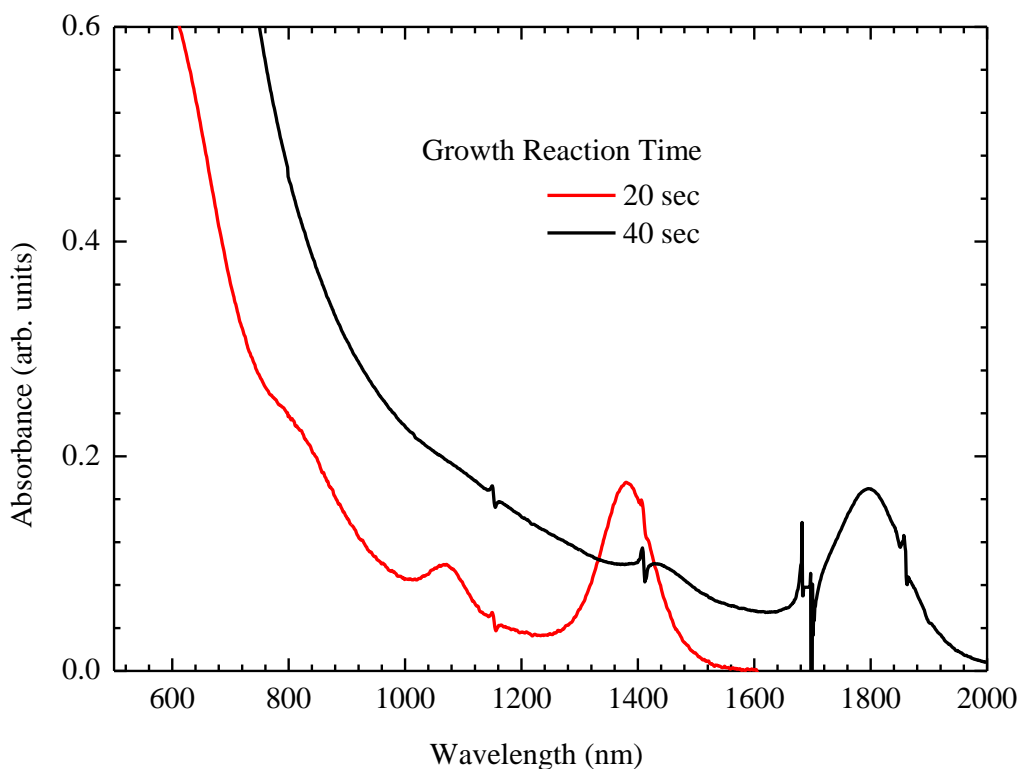


Figure 4.3 Absorbance spectra of PbSe nanocrystals grown at different reaction times.

## Ligand Exchange Effect

The effect of ligand exchange on the device optical and electrical properties was examined by measuring the current-voltage (*I-V*) characteristics and the spectral response. Several photodetectors based on PbSe nanocrystals capped with different ligands were fabricated. The effect of ligand exchange was investigated by using different ligands, such as, oleic acid, 1,2-ethanedithiol (EDT) and mercaptoacetic acid (MAA). The fabricated photodetectors used in this investigation consist of interdigital electrodes spaced by a channel with width of 50  $\mu\text{m}$  and are made from Ti (30 nm) / Au (50 nm) deposited on a glass substrate. As mentioned previously, the nanocrystals are capped with oleic acid during the synthesis process. These original ligands are insulator and will hamper the transportation of the photo-excited carriers between nanocrystals under the influence of the externally applied electric field. In this research, the oleic acid ligands were exchanged with new ligands like MAA and EDT.

Two devices were fabricated by using PbSe nanocrystals capped with oleic acid and MAA ligands. The devices were characterized by measuring the *I-V* characteristics under dark and illumination conditions and the results are plotted in figure 4.4. The photodetector that is based on nanocrystals capped with oleic acid exhibits very low dark current, on the order of  $10^{-11}$  A, and without a significant difference between the photocurrent and the dark current. On the other hand, the photodetector based on PbSe nanocrystals capped with MAA exhibits higher dark current, on the order of  $10^{-7}$  A, and a photocurrent larger than the dark current by one order of magnitude. Figure 4.5 shows the *I-V* characteristics of a photodetector based on PbSe nanocrystals capped with EDT ligands. The dark current of the device with EDT ligands is higher than that for the device with MAA, and the photocurrent to dark current ratio is 7.8 at 5 V bias, while in the case of MAA ligands the photocurrent to dark current ratio is 12.6 at 5 V bias.

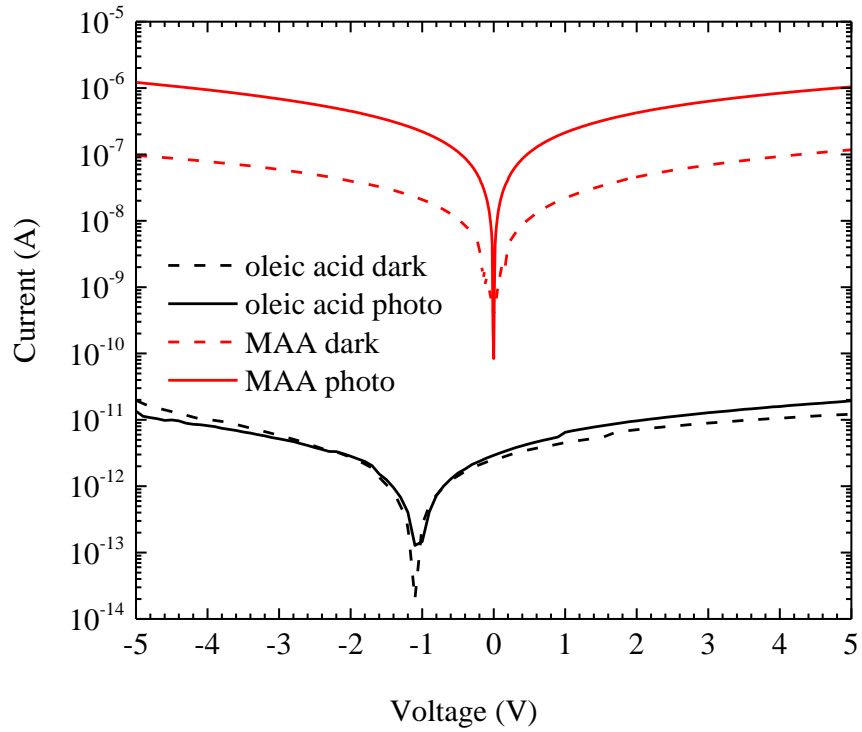


Figure 4.4  $I$ - $V$  curves of photodetectors based on PbSe nanocrystals capped with oleic acid (red curves) and MAA ligands (black curves). Reprinted with permission from Nusir *et al* [45].

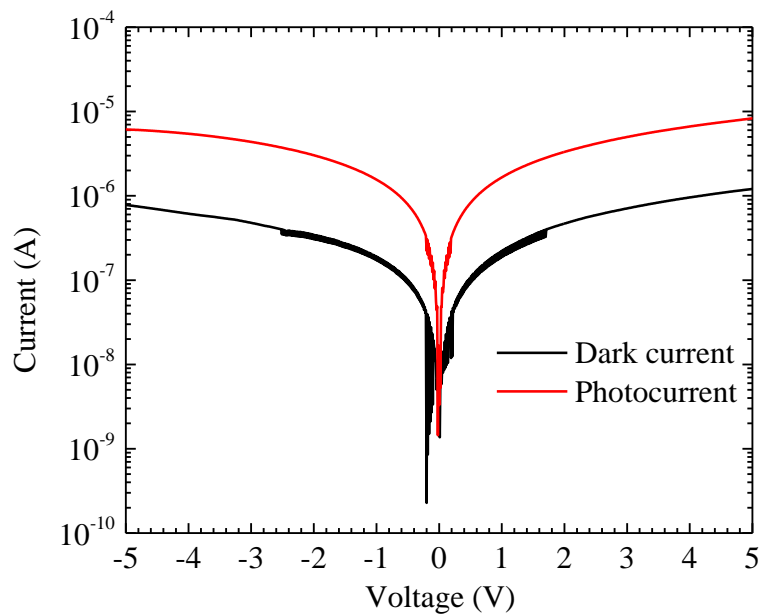


Figure 4.5  $I$ - $V$  curves of photodetectors based on PbSe nanocrystals capped with EDT ligands.

The spectral response of the two photodetectors based on PbSe nanocrystals capped with MAA and EDT ligands are plotted in figures 4.6 (a) and (b), respectively. The spectral response was measured in arbitrary units for the two devices at bias voltage of 5 V and using a beam covering the entire area of the devices. Moreover, the spectral response was measured in the spectral range between 600 to 2000 nm. Same current gain was applied to the devices during the spectral response measurement.

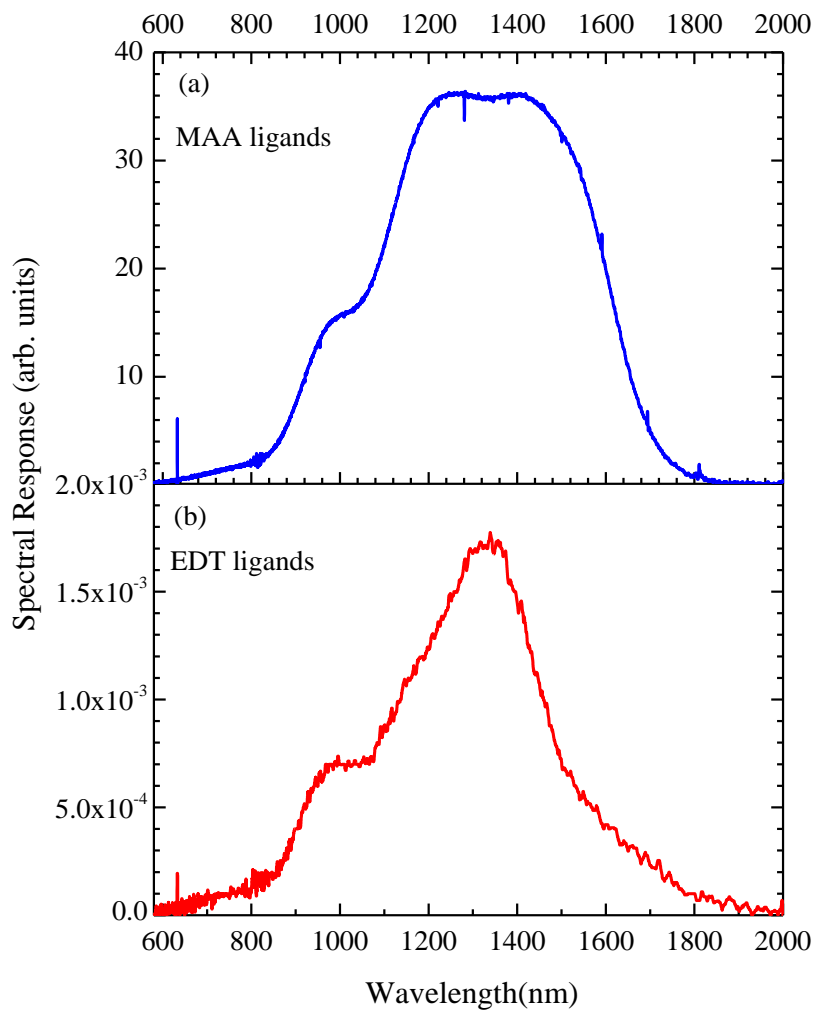


Figure 4.6 Spectral response of photodetectors based on PbSe nanocrystals capped with (a) MAA and (b) EDT ligands at 5 V bias. Reprinted with permission from Nusir *et al* [45].

From the results presented in figure 4.4, we conclude that the original ligands capping the PbSe nanocrystals are insulator and obstruct the drift of photo-excited carriers under illumination and biasing conditions. The  $I$ - $V$  curves in figure 4.4 showed increase in the dark current of devices from  $10^{-11}$  A to  $10^{-7}$  A after exchanging the original ligands with MAA ligands. Furthermore, the  $I$ - $V$  characteristics showed a significant increase in the photocurrent as compared to the dark current after the ligands exchange. The devices based on MAA ligands exhibit larger photocurrent to dark current ratio and stronger spectral response in the near-infrared spectral region as compared to the other devices based on EDT ligands, as shown in figures 4.4, 4.5, and 4.6.

The dark current is significantly lower than the photocurrent since the drift current depends on the carrier concentration, according to equation 1.3, which represents the drift current between electrodes. Under dark conditions, the carrier concentration is mainly dominated by the thermally generated carriers especially that the bandgap energy of the nanocrystals is narrow. On the other hand, the carrier concentration will increase under illumination to a higher value since the nanocrystals will be flooded by photo-excited carriers. This explains the significant increase in the current after illuminating the nanocrystals with sufficient light energy.

The mechanism of generating photocurrent is based on the circulation of the photo-excited carriers between the electrodes which requires hopping of the carriers between the nanocrystals. Since the nanocrystals are surrounded by ligands, this implies that the carriers need to tunnel through the ligands. The oleic acid ligands consist of a long hydro-carbon chain which is made from 18 carbon atoms. This will increase the tunneling distance and traps the photo-excited carriers inside the nanocrystals. The exchange of oleic acid with new shorter ligands will allow the photo-excited carriers to tunnel between the nanocrystals and generating a significant

amount of photocurrent. However the thermally generated carriers can tunnel between the nanocrystals as well, which will increase the dark current.

As indicated in figures 4.5 and 4.6, the devices based on PbSe nanocrystals that are capped with MAA ligands showed stronger spectral response and larger photocurrent to dark current ratio as compared to the other device with EDT ligands. This can be explained by looking at the compositions of each ligand. The single EDT ligand consists of dual thiols, which is a functional group consisting of hydrogen and sulfur, while the MAA ligand consists of a single thiol. This indicates that at least a single EDT ligand can link two adjacent nanocrystals, while two MAA ligands are required to link the nanocrystals. This will shorten the tunneling distance and causes the dark current to increase generating more noise, while in the case of the MAA ligands the dark current is still kept at a low level.

### Device Photoresponse

The results of the devices presented in this section were fabricated by using PbSe nanocrystals grown for 20 seconds and capped with MAA ligands. The photoresponse of the uncooled near-infrared photodetectors were investigated by measuring the  $I$ - $V$  curves under dark and light conditions. The  $I$ - $V$  curves are plotted in figure 4.7, the solid line is the photocurrent and the dashed line is the dark current. However, the electrode spacing,  $d$ , between the interdigital electrodes was varied from 10 to 50  $\mu\text{m}$ . The  $I$ - $V$  curves of each device with different electrodes spacing are plotted together in figure 4.7.

The  $I$ - $V$  results in figure 4.7 indicate that as the electrodes spacing reduces from 50 to 10  $\mu\text{m}$ , the dark current increases however the photocurrent to dark current ratio increases as well. For example, the device with electrode spacing of 50  $\mu\text{m}$  has a dark current of 0.1  $\mu\text{A}$  and a

photocurrent of  $1.2 \mu\text{A}$  at 5 V bias. While the device with electrodes spacing of  $20 \mu\text{m}$  exhibits a dark current and photocurrent of 0.2 and  $2.6 \mu\text{A}$ , respectively at 5 V bias. And for  $d = 10 \mu\text{m}$ , the dark current was  $3.1 \mu\text{A}$  and photocurrent was  $73 \mu\text{A}$  at 5 V. The photocurrent to dark current ratio for the devices was found to 23.6, 13.0, and 12.0, for devices with electrode spacing of 10, 20, and  $50 \mu\text{m}$ , respectively at 5 V bias. The increase in the photocurrent to dark current ratio as the electrode spacing reduces is due to the increase in the applied electric field between the interdigital electrodes with reference to equation 1.3. The electric field is directly proportional to the applied voltage bias and inversely proportional to the electrode spacing. Furthermore, a reduction in the electrode spacing will increase overall length of electrodes under illumination which will further increase the device active area and the photocurrent.

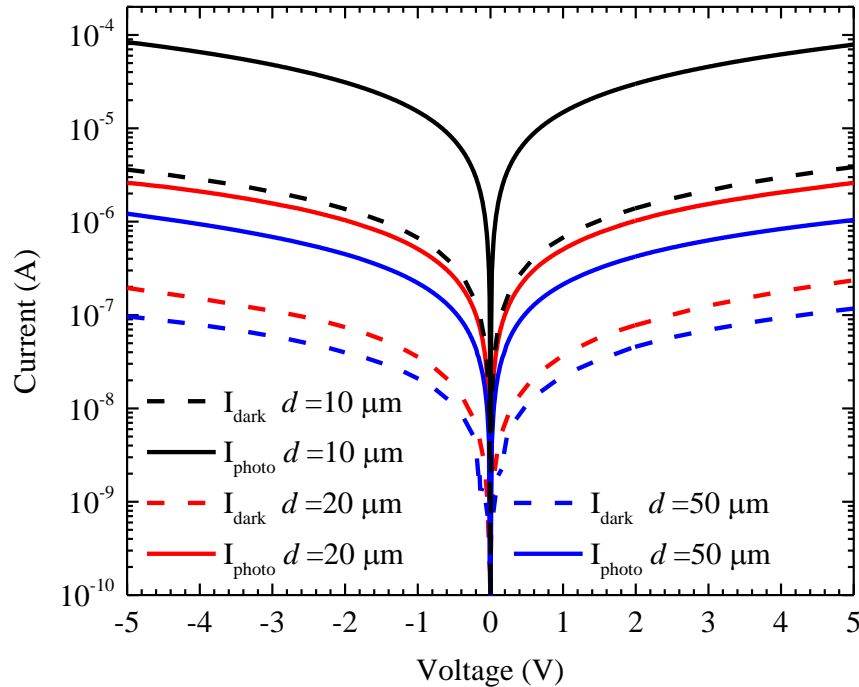


Figure 4.7  $I$ - $V$  characteristics of three devices based on PbSe nanocrystals capped with MAA ligands with different electrode spacing. Reprinted with permission from Nusir *et al* [83].



The detectivity ( $D^*$ ) of the three devices were calculated by using the  $I$ - $V$  curves in figure 4.7 and equation 1.10. The calculated detectivity of each device is plotted in figure 4.8 as function of the applied bias voltage. The detectivity of the device with electrode spacing of 10  $\mu\text{m}$  is on the order of  $2.13 \times 10^9 \text{ cm.Hz}^{0.5}/\text{W}$  at bias voltage of 5 V, while the devices with larger electrode spacing had lower detectivity. This is because of the increase in the signal to noise ratio, which depends on the photocurrent to dark current ratio, as the electrode spacing reduces. The responsivity,  $R$ , of the devices can also be calculated by dividing the photocurrent by the incident optical power. The responsivity at room-temperature for the device with  $d = 10 \mu\text{m}$  was found to be 20 mA/W at bias voltage of 5 V.

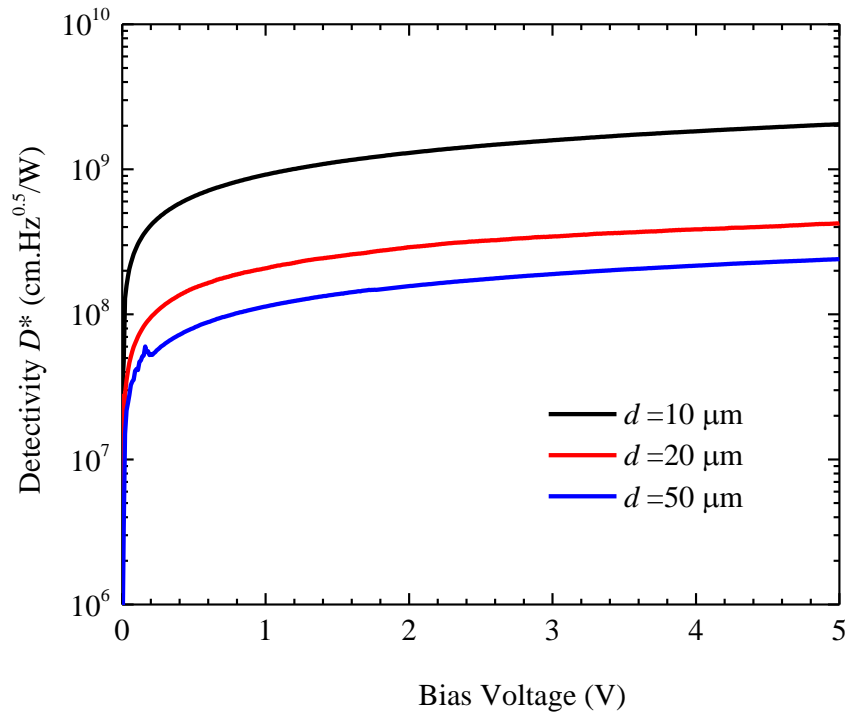


Figure 4.8 Calculated detectivity of the near-infrared photodetectors based on PbSe nanocrystals with different electrode spacing.

The transient response of the photodetectors can be found by measuring the time-resolved photocurrent under multiple on/off illumination cycles. The time-resolved photocurrent of the device with electrode spacing of 10  $\mu\text{m}$  at 5 V is shown in figure 4.9. The recovery time constant of the photodetectors can be estimated by fitting the curve with the equation  $I = I_0 e^{-t/\tau}$ , where  $\tau$  is the recovery time constant and it was found to be 0.16 seconds for the device with  $d = 10 \mu\text{m}$ . The rise time constant was also found to be 40 msec. The increase in the electrode spacing from 10 to 50  $\mu\text{m}$  did not cause a significant change in the recovery time constant. Since the recovery time depends on both the carrier transient time and the RC delay [88]. An increase in the electrode spacing will increase the carrier transient time, with reference to equation 1.5, however the capacitance between the electrodes will reduce which will decrease the RC delay time. The decay in the photocurrent while the light is on could be due to the overheating of the device.

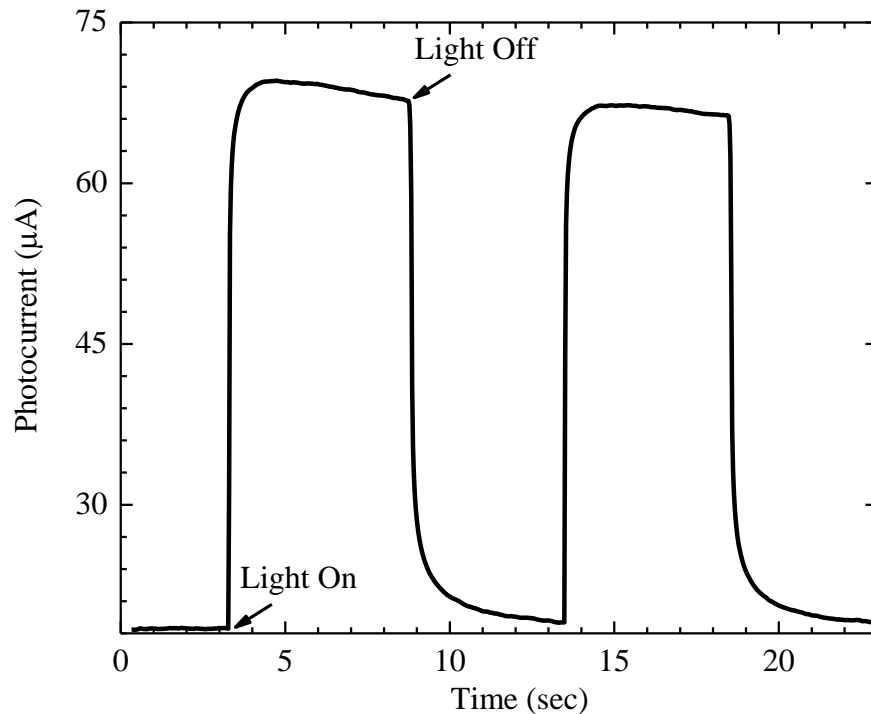


Figure 4.9 Time-resolved photocurrent curve at 5 V for device with electrode spacing of 10  $\mu\text{m}$ . Reprinted with permission from Nusir *et al* [83].

The last characterization of the near-infrared photodetectors based on PbSe nanocrystals is the spectral response, which shows how the photocurrent changes with the wavelength of light. The spectral response was measured for devices with different electrode spacing and at bias voltage of 5 V. The spectral response spectra of each device are plotted in figure 4.10 and combined with the absorbance spectrum of the nanocrystals. The spectral response consists of three strong and separate peaks covering the near-infrared region. Those peaks result from electrons undergoing interband transitions, similar to the absorption spectrum of the nanocrystals. The spectral response results are in consistence with the  $I-V$  characteristics and both showed that the higher response was obtained from the device with electrode spacing of 10  $\mu\text{m}$  as compared to the other devices with larger electrode spacing ( $d = 20$  and  $50 \mu\text{m}$ ). Furthermore, the spectral response exhibits a wavelength selectivity feature that is extended into longer wavelengths in the near-infrared region ( $1.8 \mu\text{m}$ ). Unlike the spectral response spectra reported for other photodetectors based on PbSe nanocrystals which showed a single peak positioned at lower wavelength ( $\sim 1.4 \mu\text{m}$ ) [77], [89], [90]. This implies that the device can be used in all of the applications based on near-infrared. The wavelength selectivity feature results from the quantum confinement in the nanoscale regime and it is appealing for applications that require detection at a particular wavelength.

With reference to figure 4.10, by comparing the spectral response of the devices and the absorbance spectrum of the nanocrystals we will find that the spectral response resembles the absorbance spectrum. However, the excitonic peaks in the spectral response experienced a red shift and are positioned at longer wavelength when compared with the absorbance. This can be explained according to Stark's shift especially that the absorbance was measured without voltage biasing and the spectral response was measured under the influence of applied electric field.

Another reason is the state of the nanocrystals, in which the absorbance was measured while the nanocrystals were in liquid state and the spectral response was measured while the nanocrystals are in solid state. The third reason could be due to the effect of ligands exchange. The absorbance spectrum is for PbSe nanocrystals capped with the original long ligands and the spectral response is for the PbSe nanocrystals capped with new shorter ligands. All of those reasons will affect the overlap between wave functions and affect the bandgap. The effect of changing the applied electric field on the spectral response of the device is shown in figure 4.11. Increase in the applied voltage bias will increase the spectral response since the photocurrent is proportional to the applied electric field.

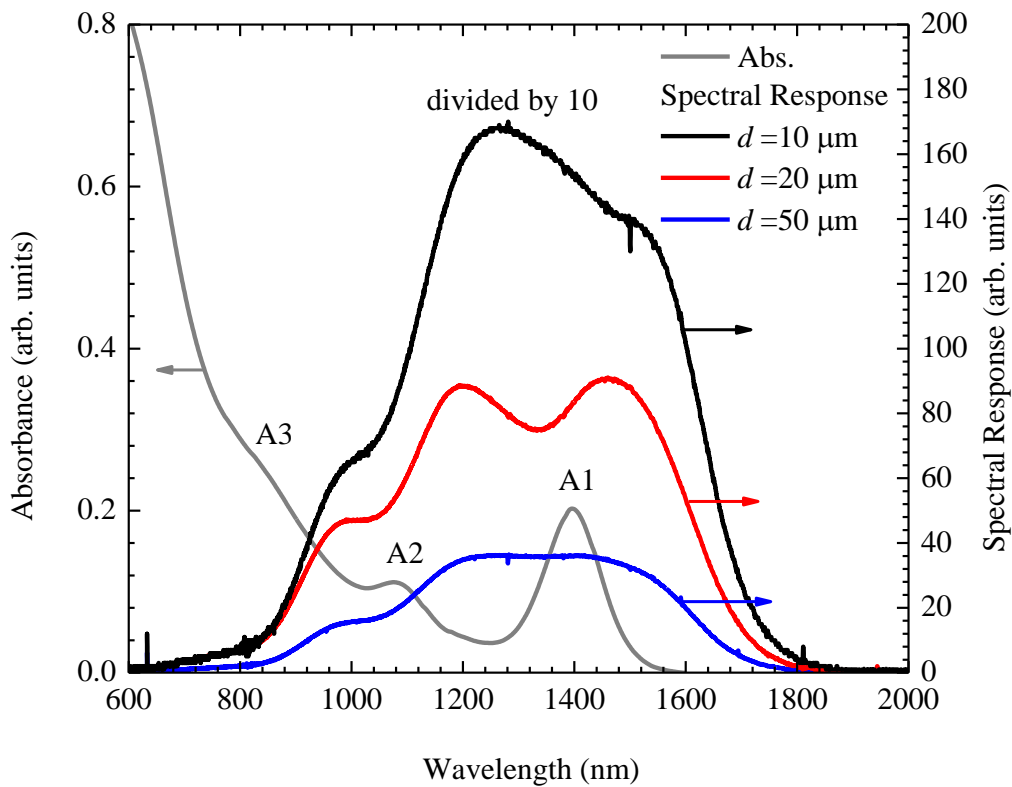


Figure 4.10 Spectral response of the near-infrared photodetectors based on PbSe nanocrystals with different electrode spacing ( $d = 10, 20, 50 \mu\text{m}$ ) at 5 V bias combined with the absorbance spectrum of the nanocrystals. Reprinted with permission from Nusir *et al* [83].

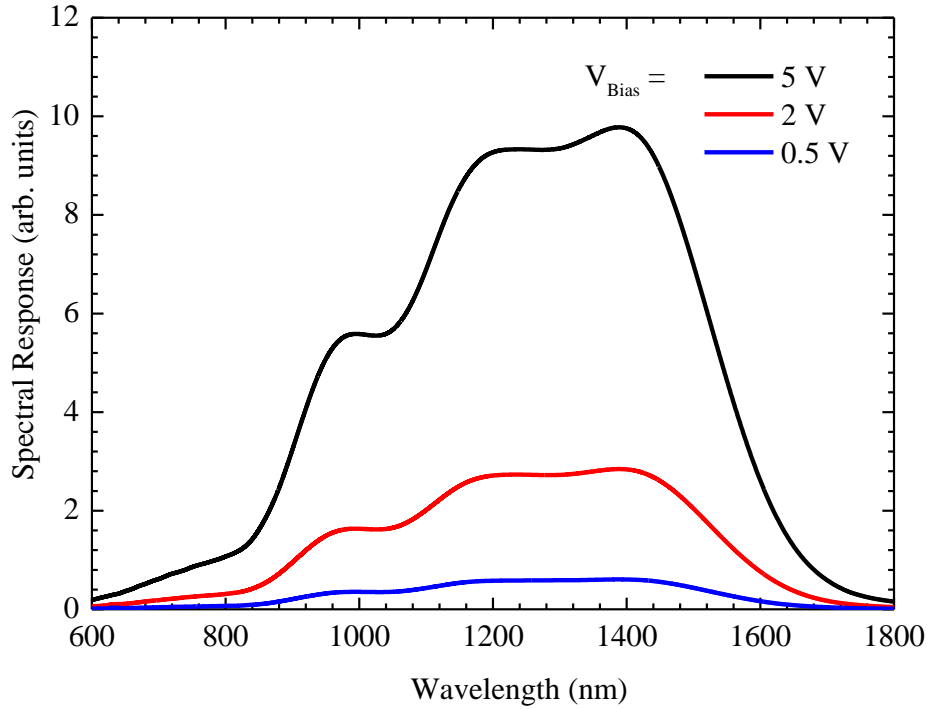


Figure 4.11 Spectral response of the near-infrared photodetector with electrode spacing of  $10\ \mu\text{m}$  at different bias voltages. Reprinted with permission from Nusir *et al* [83].

### C. Self-powered Photodetectors

#### Device Optimization

The self-powered photodetectors are based on asymmetric interdigital electrodes integrated with semi-insulating GaAs and undoped Si substrates. The devices are realized by fabricating two different metals in contact with the semiconductor, which will create asymmetric Schottky barrier at the interface between each metal and the semiconductor. In order to optimize the performance of the devices, the type of the metal contacts and the dimensions of the interdigital electrodes were varied. Figures 4.12 (a) and (b) show the  $I$ - $V$  characteristics of two self-powered photodetectors based on semi-insulating GaAs with interdigital electrodes spacing of  $5\ \mu\text{m}$  and  $50\ \mu\text{m}$ , respectively.

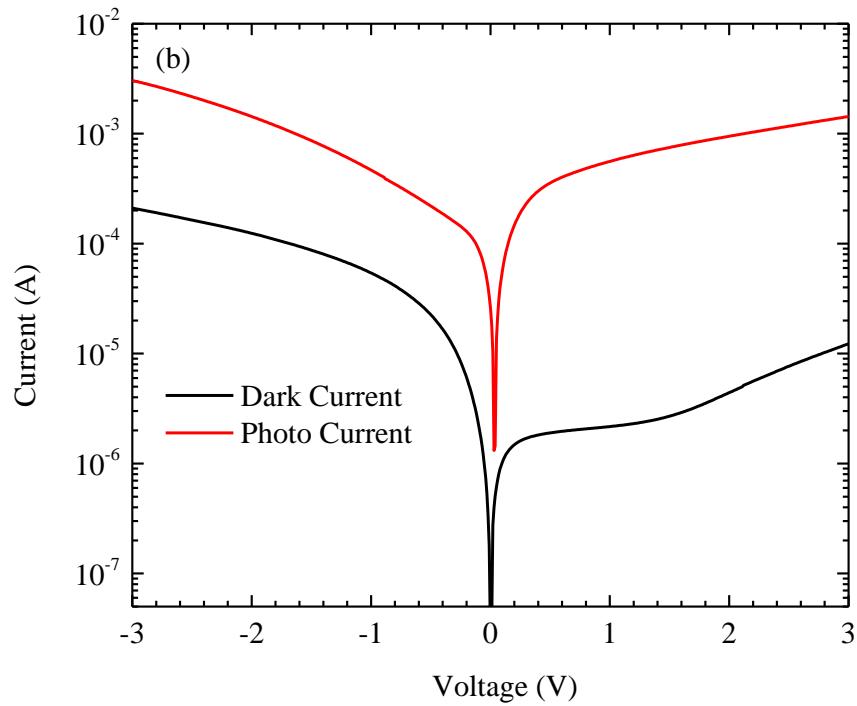
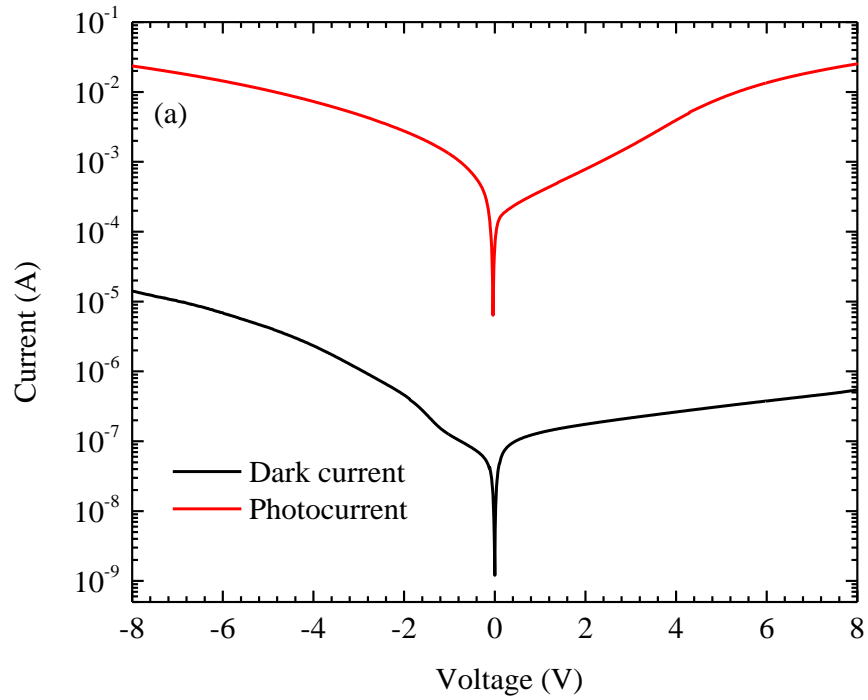


Figure 4.12  $I$ - $V$  characteristics of the self-powered near-infrared photodetectors based on semi-insulating GaAs and asymmetric interdigital electrodes spaced by (a) 5 and (b) 50  $\mu\text{m}$ . Reprinted with permission from Nusir *et al* [84].

The semi-insulating GaAs substrate has a resistivity of  $2.2 \times 10^8 \Omega \cdot \text{cm}$  and carrier concentration of  $5 \times 10^6 \text{ cm}^{-3}$ . The results in figures 4.12 (a) and (b) show significant enhancement in the devices performance after reducing the spacing between the interdigital electrodes. For the device with electrode spacing of  $50 \mu\text{m}$ , the photocurrent to dark current ratio is  $8 \times 10^2$  at 0 V, while for the device with electrode spacing of  $5 \mu\text{m}$ , the ratio is  $5 \times 10^4$  at 0 V. The detectivity of the devices can be extracted from the  $I$ - $V$  curves and using the equation 1.10, and it was found to be  $1.4 \times 10^{11}$  and  $9 \times 10^8 \text{ cm} \cdot \text{Hz}^{0.5} / \text{W}$  at 0 V bias for the devices with electrode spacing of 5 and  $50 \mu\text{m}$ , respectively. The asymmetric  $I$ - $V$  curves under dark conditions are due to the formation of the Schottky junctions, in which it is reversed biased during the positive voltage scan and forward biased for the negative voltages. While the  $I$ - $V$  curves under light conditions are symmetric due the generation of the photo-excited carriers.

The self-powered devices with different electrode spacing were further investigated by measuring the external quantum efficiency (EQE) in the visible and near-infrared regions. The EQE spectra of the devices with different electrode spacing and at 0 V bias are plotted in figure 4.13. Enhancement in the EQE was achieved as the electrode spacing reduces from  $50$  to  $5 \mu\text{m}$ . The EQE spectra of the devices exhibit a rapid increase in the wavelength region below  $870 \text{ nm}$  ( $1.43 \text{ eV}$ ), since the illumination energy in this region is higher than the bandgap of GaAs. The step observed at wavelength of  $720 \text{ nm}$  in the EQE spectra is due the change in gratings in the Oriel spectrometer.

At a wavelength of  $800 \text{ nm}$ , the self-powered device with electrode spacing of  $5 \mu\text{m}$  has an EQE of 1% which is equivalent to responsivity of  $6.45 \text{ mA/W}$ . The relationship between the responsivity and the EQE were found by using equation 1.9. This obtained responsivity is higher when compared with the responsivity of other devices based on GaAs nanocone/Graphene and

InAs/GaAs heterojunction [91], [92]. The value of EQE could be further improved by using antireflection coating to reduce the reflection from the surface and increase the absorption of light [93]. Further enhancement in the device performance can be achieved by employing plasmonic effect in sub-micron electrode spacing and optical antenna [94].

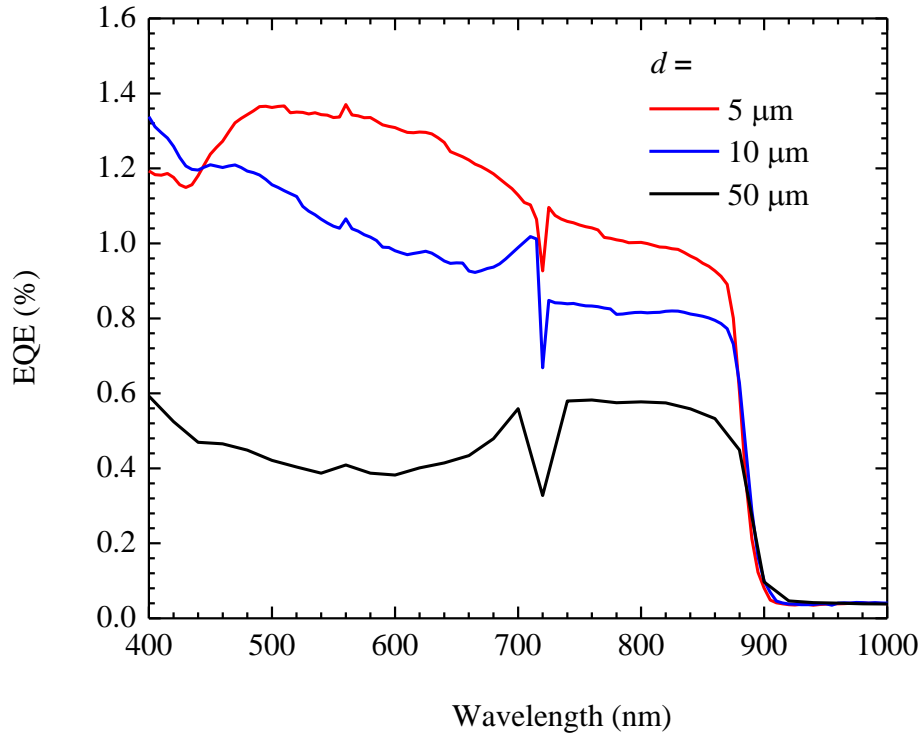


Figure 4.13 EQE spectra of the self-powered near-infrared photodetectors based on semi-insulating GaAs and asymmetric interdigital electrodes with different electrode spacing at 0 V bias. Reprinted with permission from Nusir *et al* [84].

The effect of varying the electrode spacing was further investigated by measuring the spectral response of the devices, the results are plotted at figure 4.14 (a). Enhancement in the spectral response was obtained as the electrodes spacing reduces in the same behavior shown in the *I-V* curves and EQE spectra. However, a rapid decay in the spectra response in the wavelength region below 870 nm was attained, this is mainly due to the response of the quartz



beam splitter in the FT spectrometer. On the other hand, the EQE spectra plotted in figure 4.13 do not exhibit a rapid decrease because Oriel spectrometer is a double monochromator and beam splitter is not required.

Figure 4.14 (b) shows the effect of biasing the asymmetric Schottky junction on the spectral response. By applying a positive bias to the devices, the spectral response was reduced. Since the applied electric field will oppose the junction built-in electric field and the overall electric field will be reduced as a result. On the other hand, when a negative bias was applied, the spectral response is enhanced. This is because the applied electric field is on the same direction of the built-in electric field and the overall electric field will be enhanced. The built-in electric field of the self-powered photodetector with electrode spacing of 50  $\mu\text{m}$  could be estimated from figure 4.14 (b). The built-in electric field can be found by dividing the applied forward bias at zero spectral response by the electrode spacing and it was found to be 35 V/cm. Since at zero spectral response, the applied electric will be equal in magnitude and opposite in direction to the built-in electric field. The built-in electric field could be further enhanced by using interdigital electrodes spaced by shorter channel.

The operation of devices at 0 V bias is due to the band bending, which is caused by the formation of different Schottky barrier heights at Au/GaAs and Ti/GaAs interfaces. This band bending will create built-in electric field. All the results presented in figures 4.12-4.14 are in consistence and showed that stronger photoresponse is obtained from the devices as the electrode spacing is reduced. Several factors affect the photocurrent as electrode spacing is reduced. The total length of the interdigital electrodes increases as the electrode spacing is reduced. Since smaller electrode spacing will increase the density of electrodes under illumination and consequently increase the total length of the electrodes. This will increase the photocurrent since

it is directly proportional to the electrode dimensions. Another factor that causes an increase in the photocurrent is the electric field between the interdigital electrodes. When the electrode spacing is reduced the electric field increases since it is based on an inverse relationship.

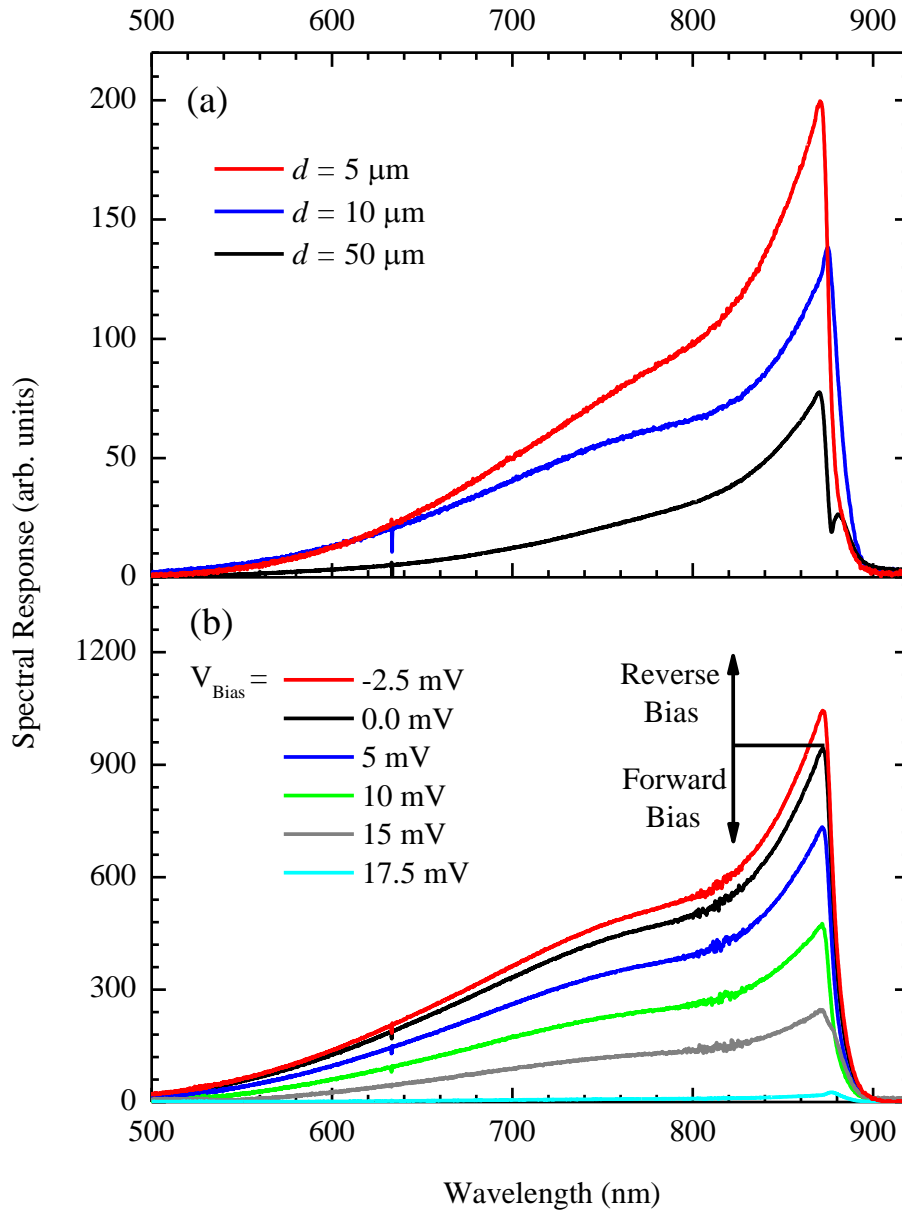


Figure 4.14 (a) Spectral response of the self-powered devices based on semi-insulating GaAs and asymmetric interdigital electrodes with different spacing at 0 V bias. (b) Spectral response of device with electrode spacing of  $50 \mu\text{m}$  and different forward/reverse bias voltages. Reprinted with permission from Nusir *et al* [84].

The asymmetric interdigital electrodes were integrated with undoped Si to fabricate self-powered photodetectors. The undoped Si substrate used in the fabrication of the devices has a resistivity higher than  $6000 \Omega\cdot\text{cm}$ . The effect of varying the electrode spacing of the asymmetric electrodes on the performance of self-powered devices based on undoped Si was studied. The EQE spectra at 0 V bias are plotted in figure 4.15 for devices with electrode spacing of 30 and 50  $\mu\text{m}$ . The types of the metal contacts used in the devices are Au and Ti with a thickness of 30 nm. The device with electrode spacing of 30  $\mu\text{m}$  showed stronger EQE than the other device with electrode spacing of 50  $\mu\text{m}$ . The EQE results are consistent with the results obtained from devices based on semi-insulating GaAs and both showed stronger response with lower spacing between electrodes.

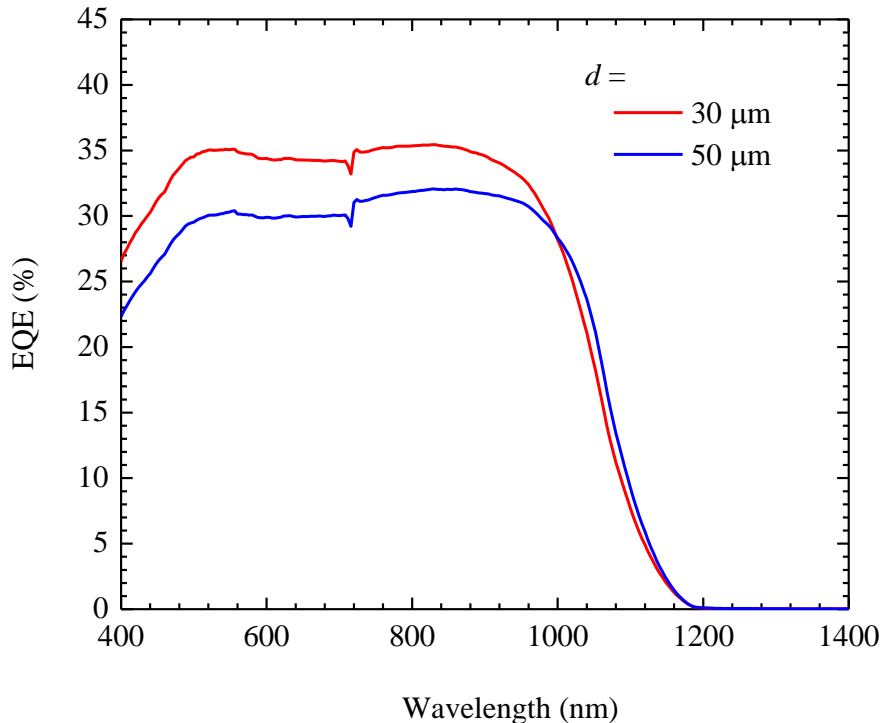


Figure 4.15 EQE spectra of self-powered photodetectors based on undoped Si with different interdigital electrode spacing at 0 V bias.

The effect of using asymmetric interdigital electrodes with different metal pairs was further investigated by measuring the  $I$ - $V$  characteristics and the EQE spectra, the results are plotted in figures 4.16 and 4.17, respectively. Three devices were fabricated with the same electrode spacing,  $d = 50 \mu\text{m}$ , but with different metal pairs of Au/Ti, Au/Ag, and Ag/Ti. All the metal contacts had the same thickness of 30 nm and deposited on undoped Si substrate.

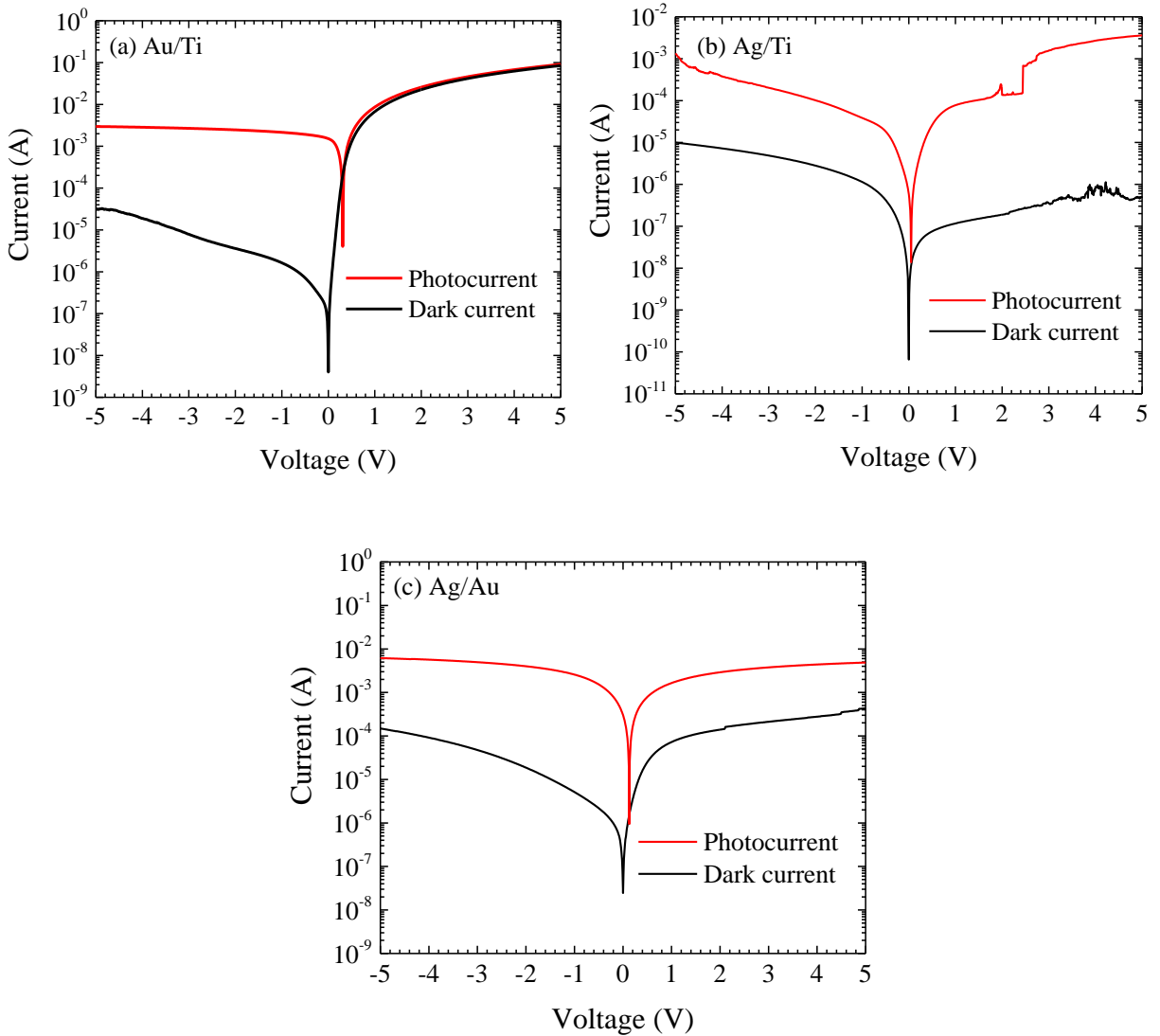


Figure 4.16  $I$ - $V$  curves of devices with electrode spacing of 50  $\mu\text{m}$  and metal pairs of (a) Au-Ti, (b) Ag/Ti, and (c) Ag/Au.

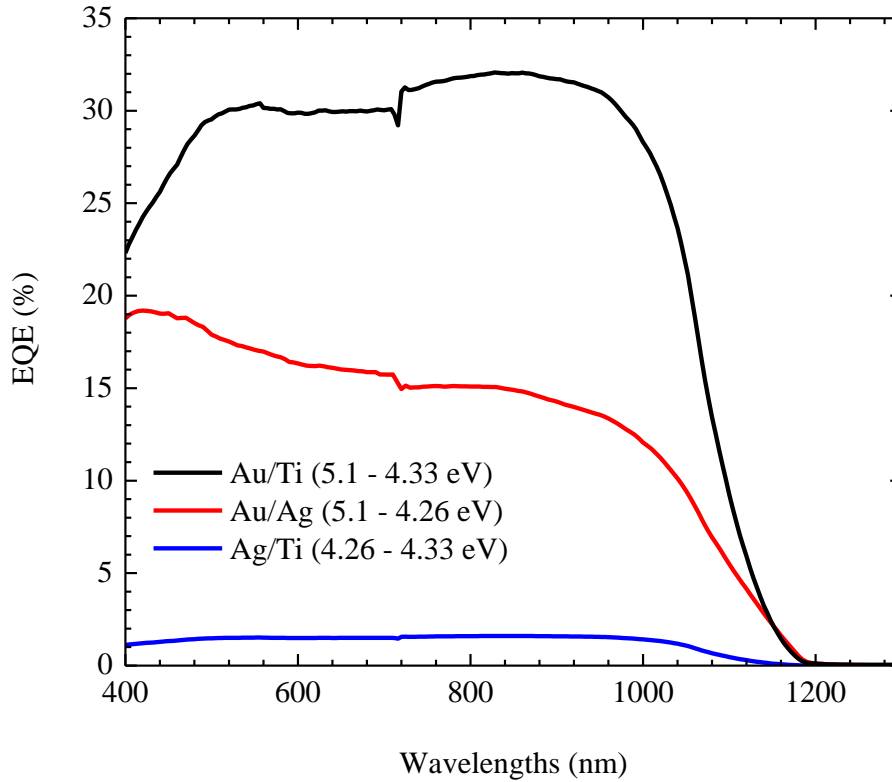


Figure 4.17 EQE spectra of devices with electrode spacing of 50  $\mu\text{m}$  and metal pairs of (a) Au-Ti, (b) Ag/Ti, and (c) Ag/Au.

From the  $I$ - $V$  results in figure 4.16, the values of the open circuit voltage are 0.04, 0.1, and 0.2 V for devices with metal pairs of Ag/Ti, Au/Au, and Au/ Ti, respectively. The EQE results in figure 4.17 showed that the strongest response was obtained from the device with metal pair of Au/Ti and the weakest response was obtained from the device with metal pair of Ag/Ti. This can be explained by correlating the values of the open circuit voltages and the EQE of each device. The device based on Au/Ti contact exhibits the largest open circuit voltage and the strongest EQE as compared with other devices with Au/Ag and Ag/Ti contacts. This large open circuit voltage will increase the amount of light generated current. Another key factor in the effect of using different metal pairs as contacts to Si is the Schottky barrier height at the interface between the metal and the semiconductor. The Au will create a Schottky contact with the Si,

while Ti and Ag will create an ohmic contact with Si and therefore the response is the weakest in the case of Ag and Ti as metal contacts.

### Device Performance

The dynamic behavior of the self-powered photodetectors was investigated by measuring the photocurrent under multiple on/off illumination cycles and at bias voltage of 5 V. The device is based on Au/Ti interdigital electrodes spaced by 5  $\mu\text{m}$  on semi-insulating GaAs substrate. The time-resolved photocurrent curve is plotted in figure 4.18. The recovery time constant at which the photocurrent decreases by 36% ( $1/e$ ), can be calculated by fitting the curve with the exponential expression:  $I = I_{\text{photo}} \exp(-t/\tau_d)$  where  $\tau_d$  is the recovery time constant and it was found to be 0.19 sec.

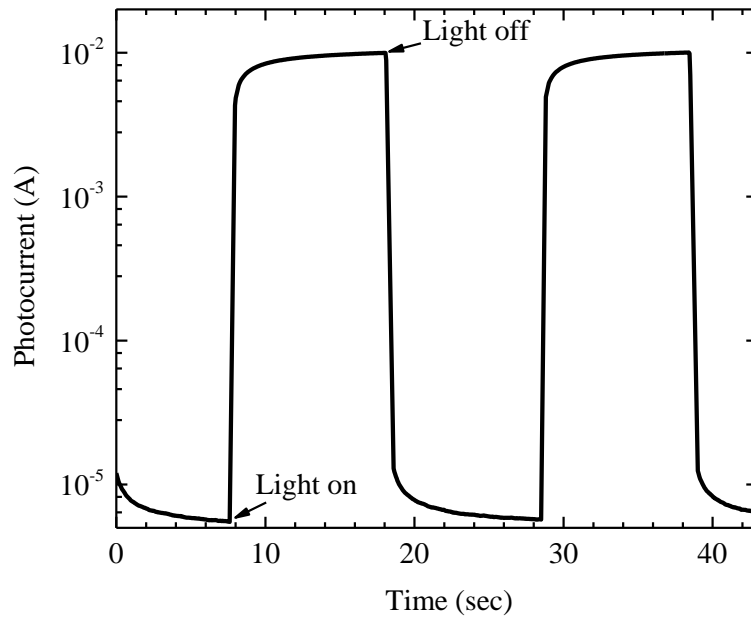


Figure 4.18 Time-resolved photocurrent curve of the device based on semi-insulated GaAs and Au/Ti interdigital electrodes spaced by 5  $\mu\text{m}$ . Reprinted with permission from Nusir *et al* [84].

The current density-voltage ( $J$ - $V$ ) characteristics of self-powered photodetectors based on undoped Si and Au-Ti interdigital electrodes spaced by  $50\ \mu\text{m}$  is plotted in figure 4.19. The current density in the units of  $\text{mA}/\text{cm}^2$  was found by dividing the current by the active area of the device, which is designed to be  $0.13\ \text{cm}^2$  for a device with electrode spacing of  $50\ \mu\text{m}$ . As shown in the  $J$ - $V$  curves, the device has a diode current behavior and under illumination the current shifts downwards by the value of light-generated current. This behavior is similar to the  $J$ - $V$  characteristics of a solar cell. Under illumination, the device exhibits an open-circuit voltage of  $V_{\text{oc}} = 0.32\ \text{V}$  and short-circuit current density of  $J_{\text{sc}} = 18.55\ \text{mA}/\text{cm}^2$ . Furthermore, the power conversion efficiency of the self-powered device was found to be 2.18% and the fill factor is 36.72%.

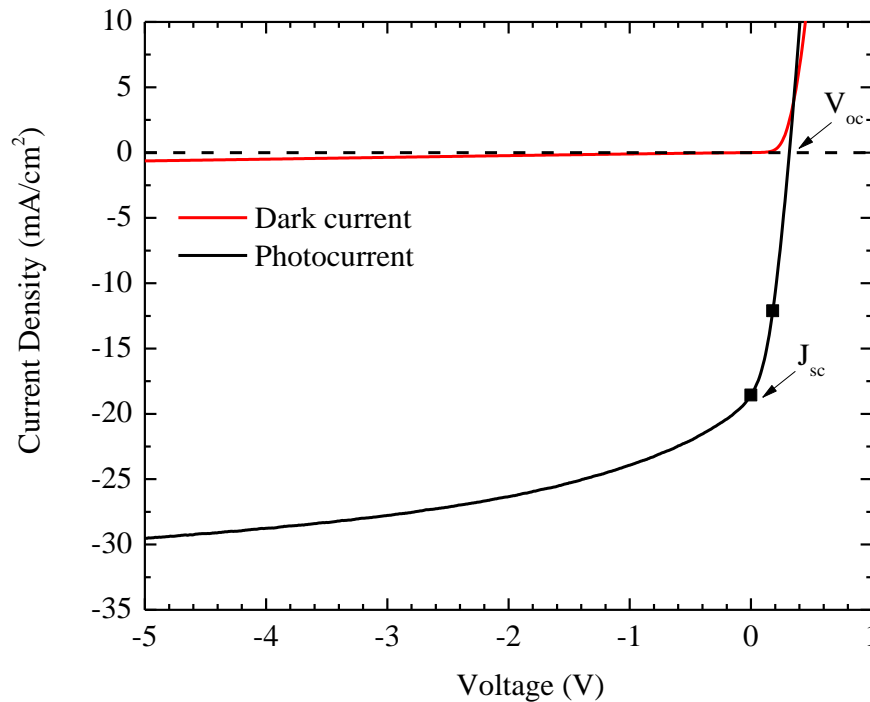


Figure 4.19  $J$ - $V$  characteristics of the self-powered near-infrared photodetectors based on undoped Si and Au-Ti interdigital electrodes spaced by  $50\ \mu\text{m}$ .

The EQE and the spectral response in photovoltaic mode of the self-powered device are plotted together as function of wavelength in figure 4.20. The EQE and spectral response measurements are for the same device with the  $J$ - $V$  characteristics in figure 4.19. The EQE of the self-powered device has an onset at wavelength of 1200 nm, which corresponds to the bandgap of Si, and an average EQE of 30% in the visible and near-infrared regions. On the other hand, the spectral response exhibits the same threshold as the EQE but has a rapid decay in the higher energy region. This is due to the response of the beam splitter in the FT spectrometer. The responsivity of the device can be extracted from the EQE spectrum and using equation 1.9. The responsivity of the device was found to be 0.23 A/W at wavelength of 1000 nm and bias voltage of 0 V. A comparison in the performance between the self-powered photodetector based on undoped Si and a typical Si p-n junction solar cell is shown in figure 4.21.

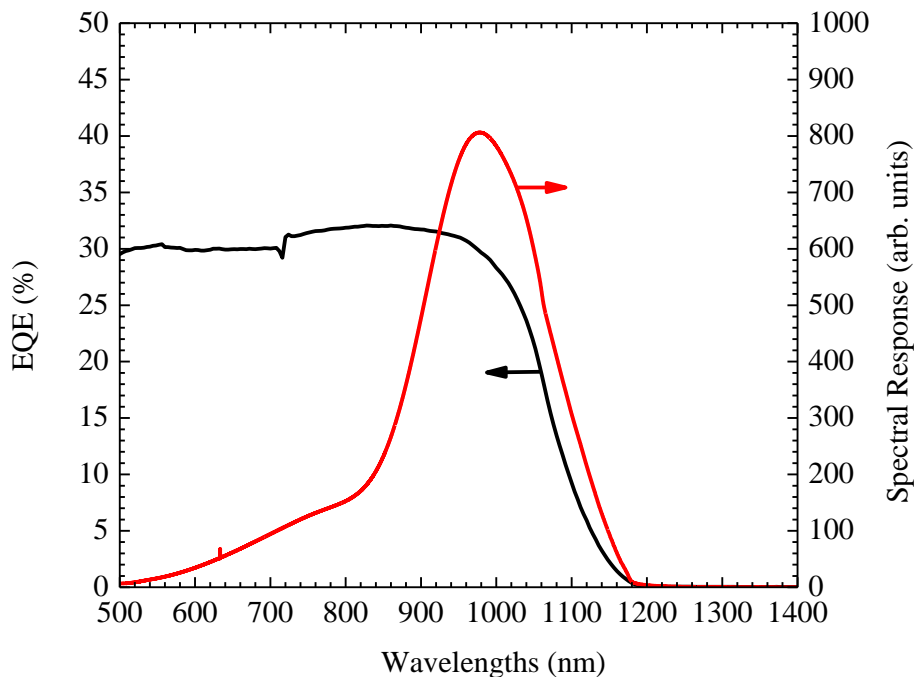


Figure 4.20 EQE and spectral response spectra at 0 V of the self-powered near-infrared photodetectors based on undoped Si and Au-Ti interdigital electrodes spaced by 50  $\mu$ m.



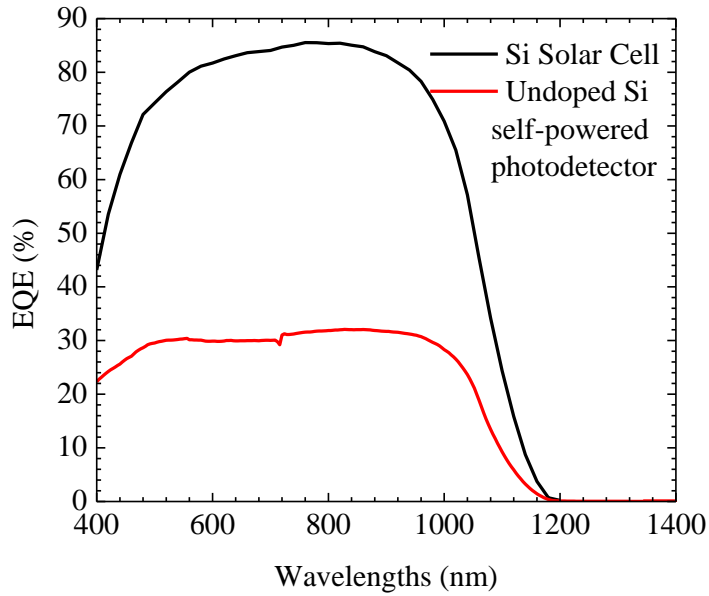


Figure 4.21 EQE of the self-powered photodetector and solar cell based on Si at 0 V.

#### D. Photodetectors Based on Si Nanowires

##### SEM Images

The SEM images of the Si nanowires grown using electroless etching are shown in figure 4.22. The procedure to grow the Si nanowires was described in details in section C of chapter 2. According to this procedure, the diameter of the grown Si nanowires can vary in the range between 50 to 150 nm [82]. The nanowires length can be controlled by varying the etching time. This procedure is very simple to implement since it does not require the use of plasma etching but its drawback is the difficulty to precisely control the diameter of the grown Si nanowires.

To have a better control over the diameter of the grown Si nanowires, nanosphere lithography can be implemented. All the details about the growth are listed in section D of chapter 2. The SEM images of the grown Si nanowires using this procedure are shown in figures 4.23 and 4.24. The oxygen plasma etching time was varied between 20 to 25 minutes. The SEM

images in figure 4.23 are for Si nanowires grown using oxygen plasma etching time of 20 min and Au (15 nm) as the metal catalyst. On the other hand, the SEM images in figure 4.24 are for Si nanowires grown using oxygen plasma etching time of 25 min and Ag (40 nm) as the metal catalyst. The average diameters of the grown Si nanowires are 150 and 120 nm for the nanowires depicted in figures 4.23 and 4.24, respectively.

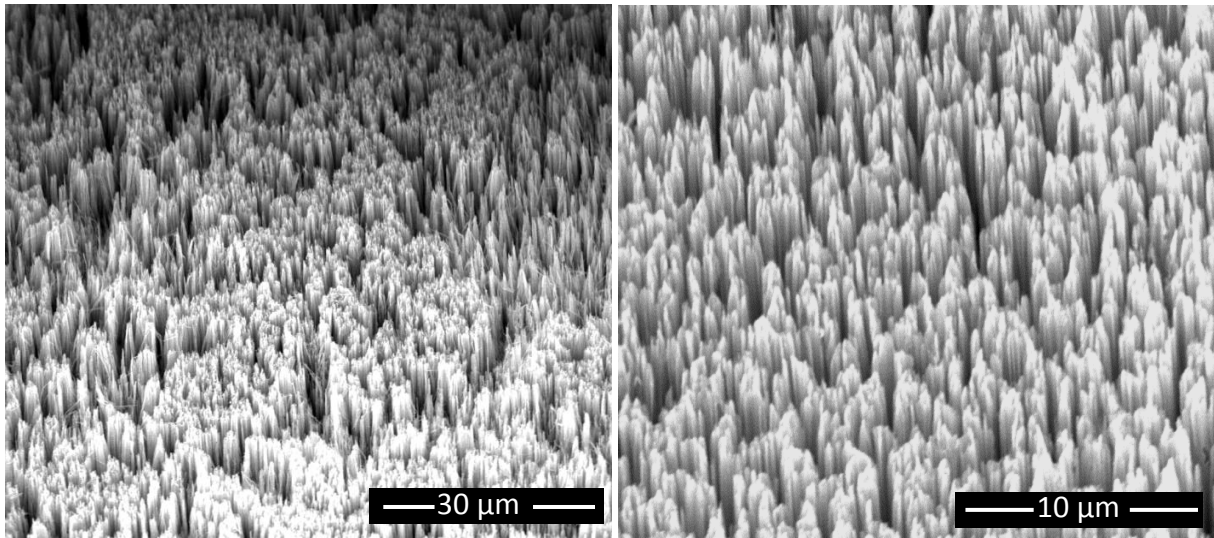


Figure 4.22 SEM images of Si nanowires grown using electroless etching.

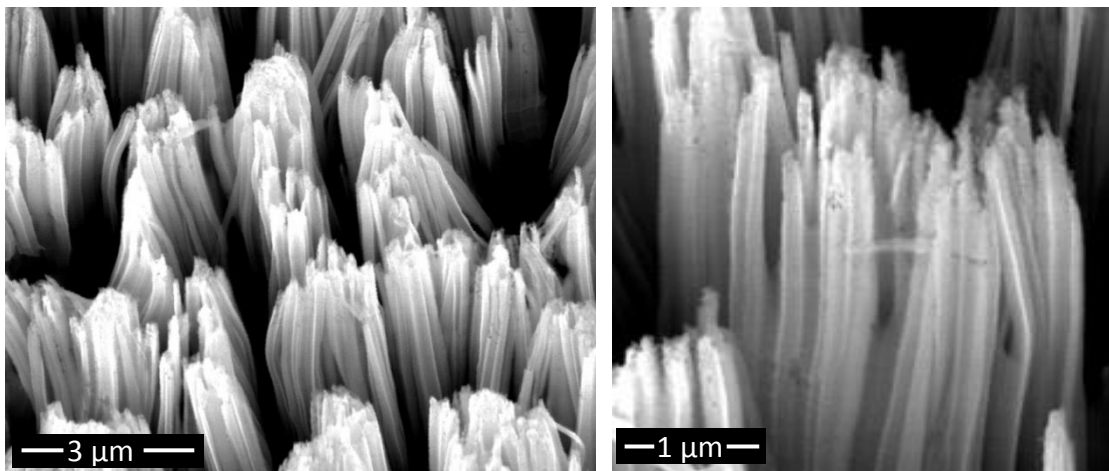


Figure 4.23 SEM images of Si nanowires grown using nanosphere lithography with O<sub>2</sub> plasma for 20 min and Au (15 nm) metal catalyst.

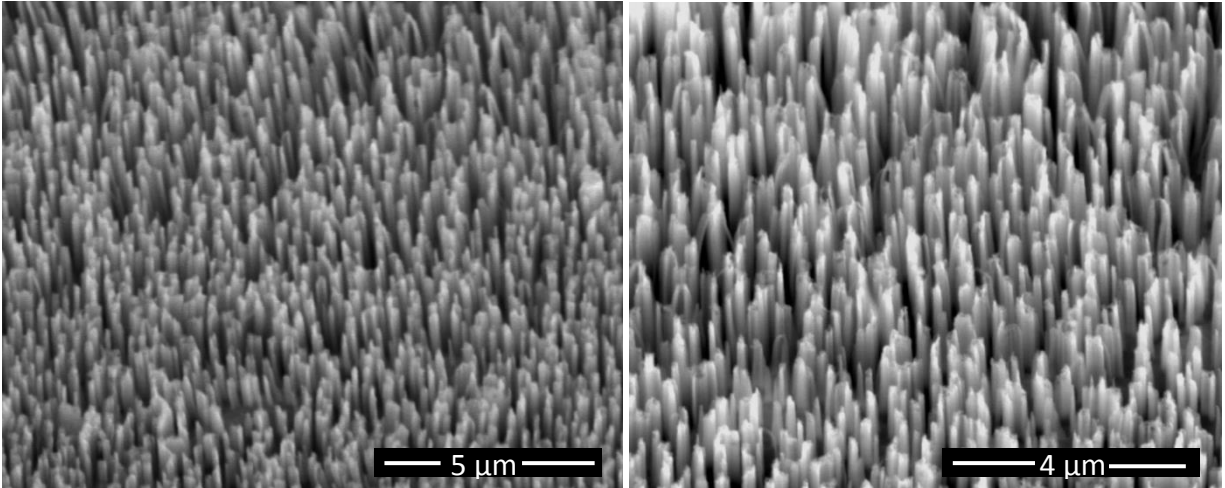


Figure 4.24 SEM images of Si nanowires grown using nanosphere lithography with O<sub>2</sub> plasma for 25 min and Ag (40 nm) metal catalyst.

The SEM images of the Si nanowires used in the fabrication of the self-powered near-infrared photodetectors are shown in figure 4.25. The vertically-aligned Si nanowires were grown using electroless etching. From the SEM images, the diameters of the Si nanowires were found to vary in the range between 89 to 165 nm with an average diameter of 125 nm. From the cross-sectional SEM image in figure 4.25, the length of Si nanowires was controlled to be 3 μm. This length of the nanowires was achieved by setting the etching time in the HF acid to be 40 minutes. The length of the nanowires can be increased by etching the samples in the HF acid for longer times. Longer nanowires can reduce the reflection from the surface and increase the absorption of light. The obtained diameter and length of the nanowires are in consistency with previous report on Si nanowires grown using electroless etching with the same procedure [81]. The SEM images show also that high density of nanowires was obtained over large areas along with vertical alignment of the nanowires. The color of the surface of the sample will turn into deep black after the formation of the nanowires.

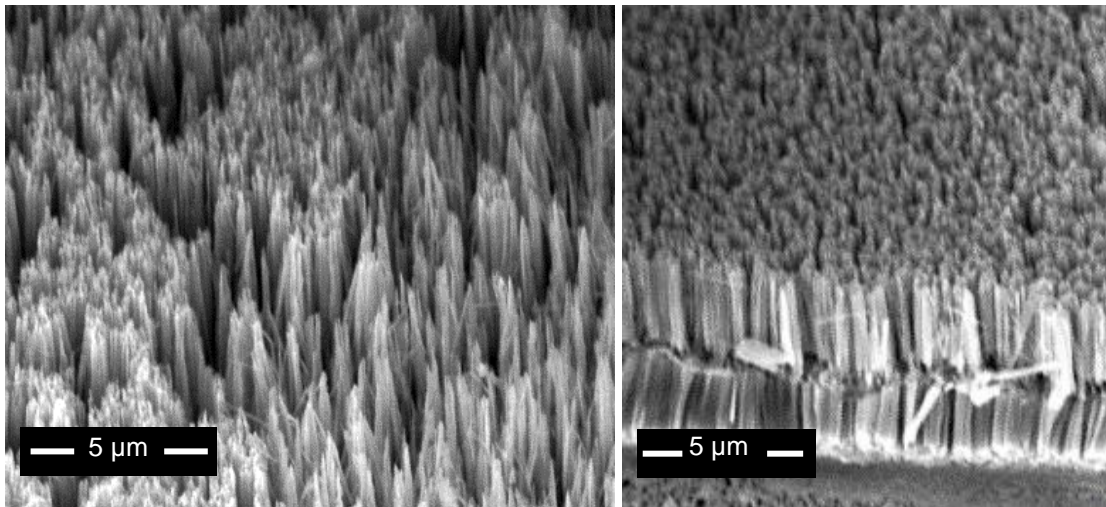


Figure 4.25 SEM images of the vertically-aligned Si nanowires used in the fabrication of the self-powered near-infrared photodetectors. Reprinted with permission from Nusir *et al* [85].

### Device Performance

To investigate the effect of Si nanowires on the performance of self-powered near-infrared photodetectors, control device was used. The control device consists of Au and Ti interdigital electrodes with thickness of 30 nm and spaced by 50  $\mu\text{m}$  channel and without Si nanowire in the channel between the electrodes. The  $J$ - $V$  characteristics of the control device and the device with Si nanowires are plotted together in figure 4.26. Similar to the  $J$ - $V$  curves in figure 4.19, the devices has a diode rectifying behavior and the photocurrent curve shifts by the value of light-generated current under light conditions. The control device has an open-circuit voltage of 0.23 V and short-circuit current density of 11.6  $\text{mA}/\text{cm}^2$ . After applying the Si nanowires in the channel between the interdigital electrodes, the short-circuit current density increases to 15.3  $\text{mA}/\text{cm}^2$ , which corresponds to an enhancement of 32% in the short-circuit current.

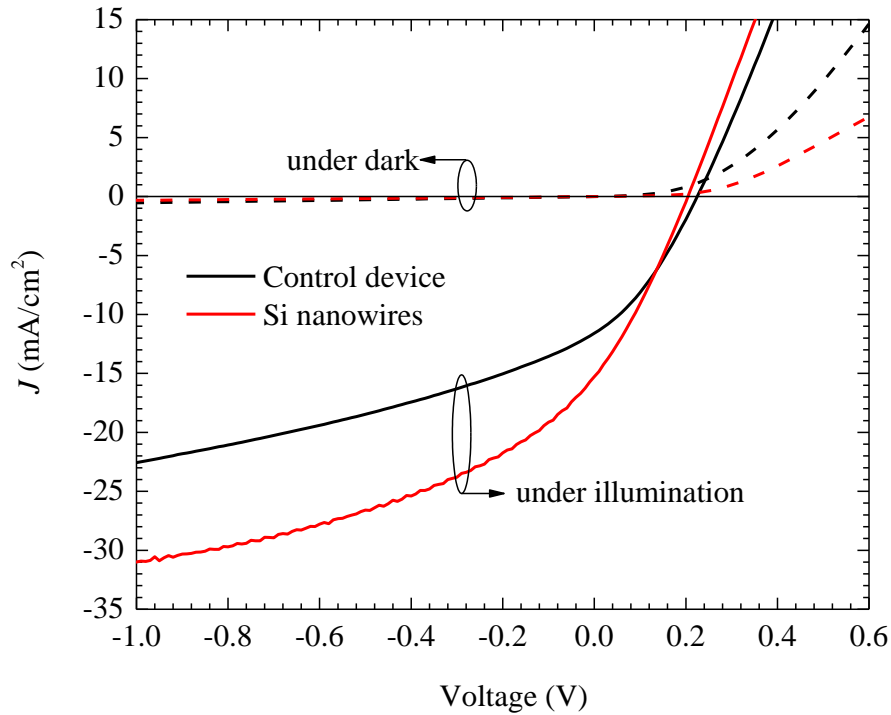


Figure 4.26  $J$ - $V$  curves of the control device and the device with Si nanowires under dark conditions (dashed lines) and light (solid lines). Reprinted with permission from Nusir *et al* [85].

The EQE spectra of the control device and two devices with Si nanowires are plotted in figure 4.27 at 0 V bias. The two devices with Si nanowires have the same dimensions of the interdigital electrodes and metal thickness as the control device. The control device exhibits an average EQE value of 5.4% in the visible and near-infrared spectral regions with an onset at wavelength of 1200 nm. After applying the Si nanowires in the channel between the interdigital electrodes, significant enhancement in the EQE was obtained. The enhancement covers the wavelength spectral range between 800 to 1200 nm. The peak in the EQE spectrum of the Si nanowires device D1 is ranging from the visible to the near-infrared with an average value of 10.3% at 965 nm and FWHM of 450 nm. The EQE values of both devices with nanowires exhibit the same decay behavior in the higher energy region. The EQE peak of the device D2 is slightly broader than the EQE peak of the device D1.

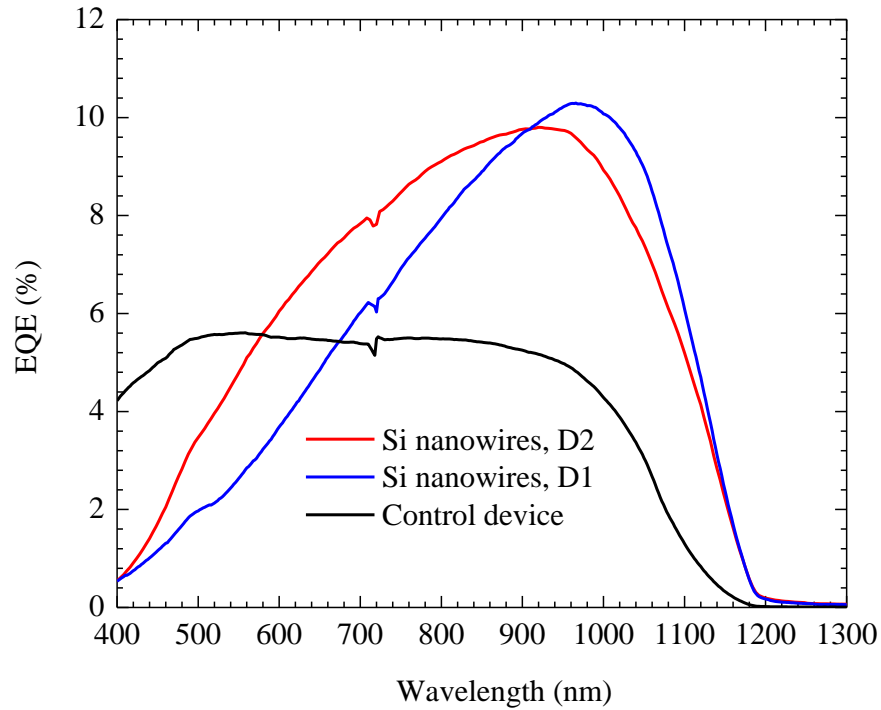


Figure 4.27 EQE spectra of the control device and two devices with Si nanowires at 0 V bias.

The effect of applying Si nanowires on the spectral response was further investigated. The spectral response spectra are plotted in figure 4.28 (a) for both the control device and a device with Si nanowires. Enhancement and broadening was achieved in the spectral response after applying the Si nanowires. The spectral response was measured in photovoltaic mode for both devices. The spectral response results in figure 4.28 (a) are in consistence with the EQE measurements in figure 4.27. The spectral response of the device with Si nanowires increases rapidly above the bandgap of Si (1.1 eV) as compared to the control device without nanowires. The effect of Si nanowires on the performance of devices based on symmetrical interdigital electrodes spaced by 50  $\mu\text{m}$  and Ti contacts was investigated and the results are plotted in figure 4.28 (b). Similar enhancement and broadening was obtained with the symmetrical contacts as compared to the devices with asymmetrical contacts in figure 4.28 (a).

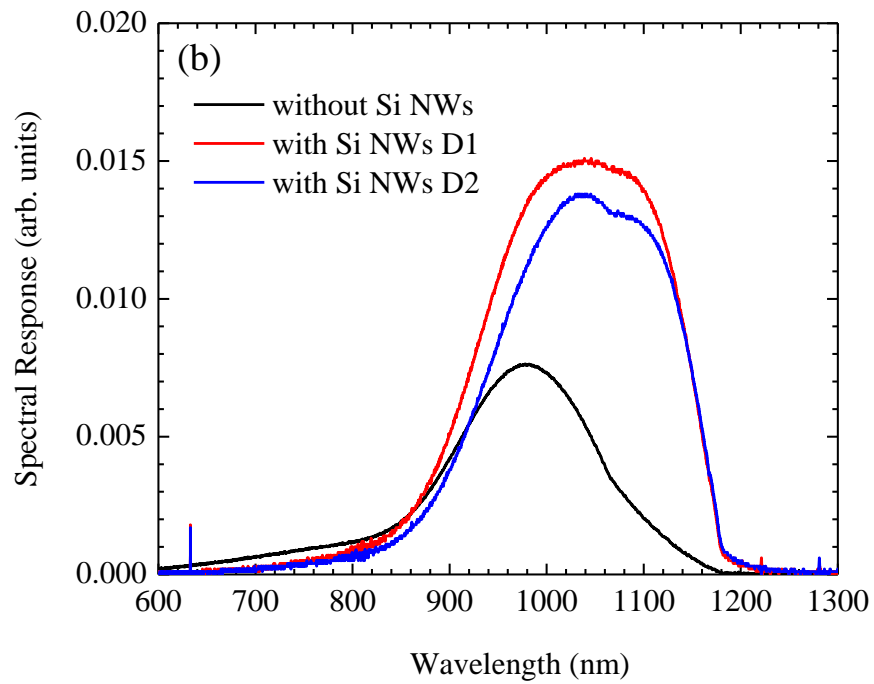
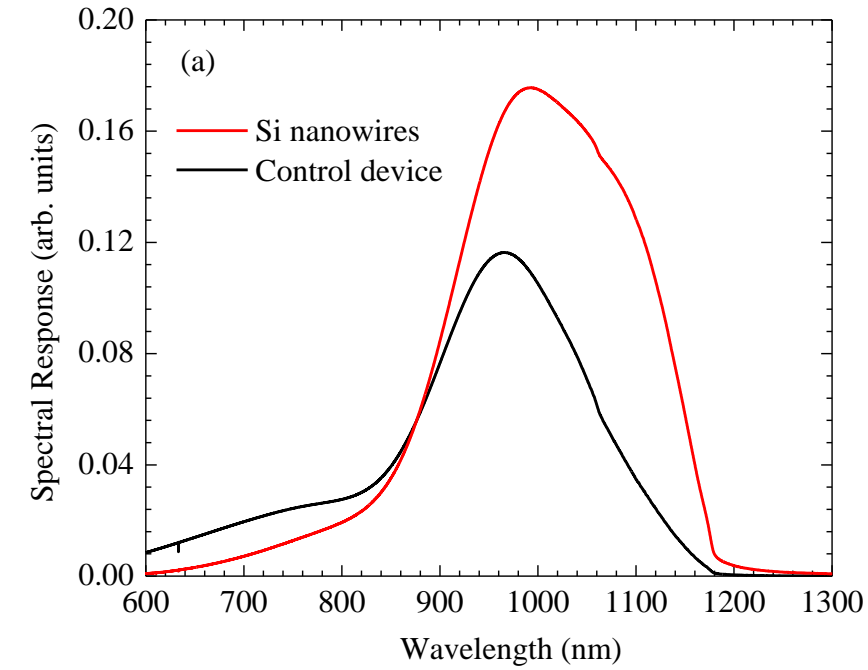


Figure 4.28 (a) Spectral response spectra of the control device and device with Si nanowires at 0 V bias. Reprinted with permission from Nusir *et al* [85]. (b) Spectral response of devices based on symmetrical electrodes spaced by 50  $\mu\text{m}$  at 3 V bias with and without nanowires.

The vertically-aligned Si nanowires can enhance the absorption of light through suppressing the reflection of light from the surface [82], [95]. This anti-reflection property will provide stronger absorption of light and therefore will lead into enhancement in the photoresponsivity of the devices based on nanowires. The reflection of light from the surface strongly depends on the length of the nanowires; longer nanowires exhibits lower reflection from the surface. As a result, further enhancement in the photoresponsivity of the devices is expected using longer nanowires. Additionally, the Si nanowires have larger aspect ratio which will allow for absorbing larger amount of light. It is noted that the implementation of nanowires with asymmetrical interdigital electrodes spaced by smaller channel will further enhance the device performance by increasing the electric field inside the channel, with reference to figure 4.15.

As mentioned previously, the operation at 0 V bias is the result of using asymmetric Schottky barriers, Au and Ti, in contact with the Si substrate. This will create band bending in the Si and will create a built-in electric field. The built-in electric will separate the photo-excited carriers and generates a photocurrent at 0 V. The Schottky barrier height at the Au/Si and Ti/Si interfaces are calculated to be 1.09 and 0.32 eV, respectively, as was shown previously in figure 1.8. An increase in the Schottky barrier height will further strengthen the built-in electric field. The formation of the Schottky junction can be confirmed from the diode rectifying behavior, which was obtained from the  $J$ - $V$  curves of the devices in figure 4.26.

As shown previously from the EQE results of devices with Si nanowires, the spectrum consists of a peak centered at wavelength of 965 nm. This peak in the EQE is the result of the quantum confinement in the Si nanowires and is due to the intrinsic transition above the band-edge of Si [96]. It is also noted that the EQE spectrum with nanowires exhibits a reduction in the higher energy region ( $> 1.8$  eV). This reduction is due to the excessive surface recombination of



the photo-excited carries over the surface of the Si nanowires. The surface recombination is caused by the large surface-to-volume ratio of the Si nanowires [97]. This reduction in the EQE in the higher energy region was also reported in another photovoltaic devices based on Si nanowires [53], [96].

The responsivity of the devices with Si nanowires can be extracted from the EQE spectrum in figure 4.27. The maximum responsivity the device was found to be 0.08 A/W at 965 nm and 0 V bias. This obtained responsivity at 0 V is on the same order of that obtained from photodetectors with similar planar structure (metal-Si nanowires-metal) and biased at -10 V [98], [99]. Other photodetectors with vertical structure of ITO-Si nanowires-Al showed responsivity of 0.3 A/W at 800 nm and -2 V [100]. The self-powered photodetectors based on Si nanowires in this work showed a responsivity of 0.05 A/W at the same wavelength and 0 V bias. An applied reverse bias voltage to the devices will enhance the built-in electric field and consequently increase the responsivity of the device, as was shown in figure 4.14 (b).

#### **E. Hot Electrons in Au Thin-films**

The hot electrons generated in Au thin-films were utilized to enhance the photocurrent and the spectral response of photodetectors based on semi-insulating GaAs. The enhancement was studied as function of Au thin-film. Furthermore, the effect of adding Ti adhesive layer between Au and GaAs on the injection of the hot electrons was investigated. For this propose an array of the Au thin-films was designed and fabricated using optical photolithography. The array consists of pairs of square metallic pads, each of 20 x 20  $\mu\text{m}$  and spaced by 2  $\mu\text{m}$  channel, as shown in figure 4.29. The thickness of the thin-film was varied in the range between 1 to 50 nm. The horizontal and vertical spacing between the pairs of metallic pads are 40 and 100  $\mu\text{m}$ ,

respectively. The rationale behind designing pads with these dimensions is set by the minimum resolution of patterns than can be fabricated in Optoelectronics Research Lab. With these dimensions, this metallic array will cover 4% of the total active area between the electrodes. The array of thin-films was applied between electrodes spaced by 0.95 mm and the performance of the device was measured before and after applying the array.

As mentioned previously, the metals have higher carrier concentration as compared to the semiconductor. However the carriers are confined by the Schottky barrier formed at the interface between the semiconductor and the metal, as was shown in figure 1.9. If the metallic array is illuminated with energy higher than the Schottky barrier energy, internal photoemission of hot electrons will occur and this will increase the overall photocurrent between the electrodes. A voltage bias is applied to create an electric field between the electrodes that will allow the photo-excited carriers and the hot electrons to circulate generating a photocurrent.

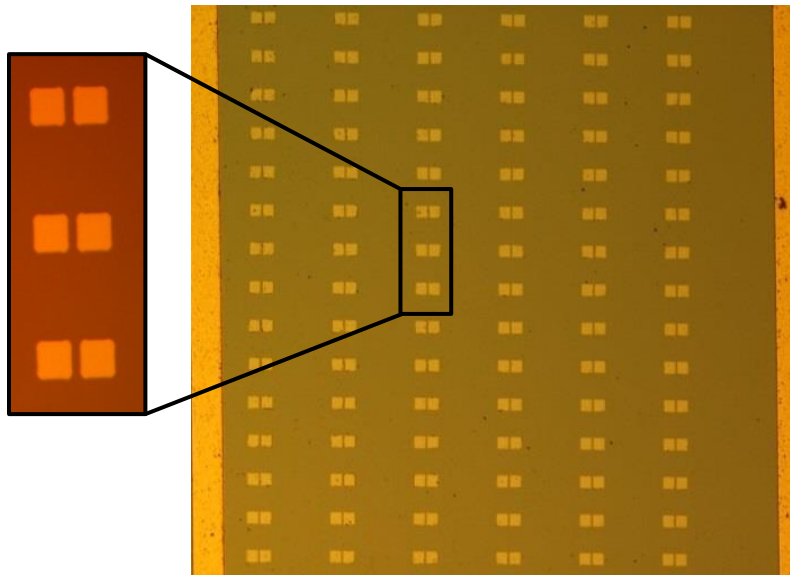


Figure 4.29 Microscopic image of the array of Au thin-films as applied between planar electrodes on semi-insulating GaAs substrate.

## Photocurrent Map

To provide a further understanding of the mechanism of hot electron generation and their subsequent injection into the semiconductor, photocurrent map was measured. The setup of the photocurrent map experiment was discussed previously in chapter 3 section C. In this experiment, a focused red laser with energy higher than the Schottky barrier energy was swept over the Au thin-films and the photocurrent between the electrodes was measured and plotted as function of the laser position. The photocurrent map is plotted in figure 4.30 for an Au thin-film with thickness of 30 nm and at bias voltage of 5 V. The photocurrent map was measured for both vertical and horizontal scans of the red laser over the thin-film.

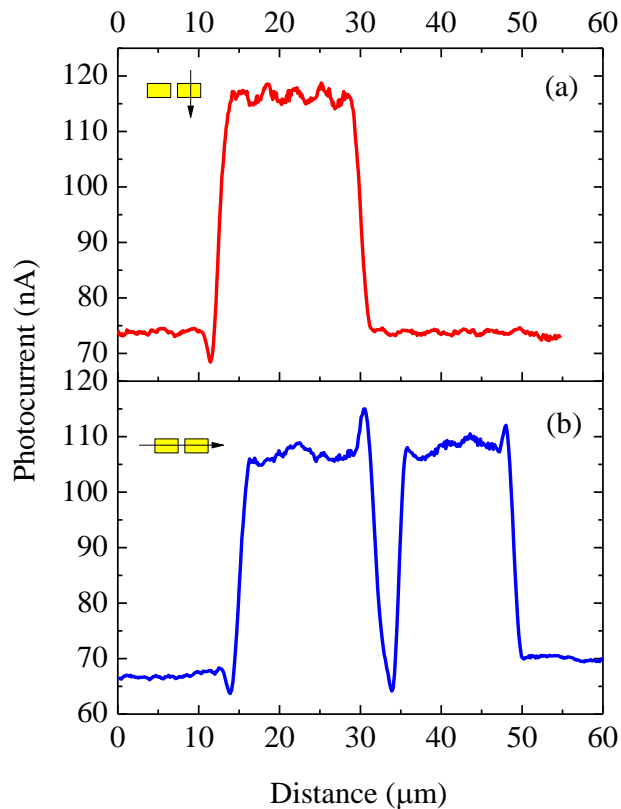


Figure 4.30 Photocurrent map at bias voltage of 5 V over an Au thin-film with thickness of 30 nm. Reprinted with permission from Nusir *et al* [86].

In the vertical scan plotted in figure 4.30 (a), the photocurrent was limited to 74 nA when the laser was focused on the semiconductor. And as the laser was swept over the Au thin-film, the photocurrent increased to 118 nA. This increase in the photocurrent is due to the excitation and injection of hot electrons. Figure 4.30 (b) shows the photocurrent map for a horizontal scan across the same pair of Au thin-film. The drop in the photocurrent in the middle is due to the gap between the pair of pads. The red laser energy of 1.96 eV is higher than the energy of the Schottky barrier, which is calculated to be 0.96 eV, and therefore it excites hot electrons in the Au thin-film. The hot electrons will be injected into the semiconductor and will drift under the influence of the electric field applied between the electrodes. These injected hot electrons will contribute in enhancing the overall photocurrent.

#### Photoresponsivity Enhancement

The  $I$ - $V$  characteristics under light illumination were measured before and after depositing the thin-film metal array onto the device. The  $I$ - $V$  results are plotted in figure 4.31 (a). The thickness of the Au thin-film was set to 50 nm and without a Ti adhesive layer between the metal and the semiconductor. After applying the metal thin-film array, the photocurrent at 5 V increased from 12.45  $\mu$ A to 24.5  $\mu$ A, which corresponds to an enhancement of 97% in the photocurrent. The same device was characterized by measuring the spectral response at bias voltage of 5 V with and without the array of Au thin-film. The results are plotted in figure 4.31 (b). Enhancement in the spectral response in both the visible and near-infrared spectral regions was observed after applying the array. A peak is noticed in the spectral response at wavelength of 1280 nm (0.96 eV), which is below the bandgap energy of GaAs (1.42 eV). This peak is due to the internal photoemission of hot electrons above the Schottky barrier formed at the Au/GaAs interface. The spectral response exhibits a rapid increase in the wavelength region below 870 nm

(1.42 eV) which is due to the excitation of carriers in the bulk GaAs. As usual, the rapid decay in the spectral response in the lower wavelength region is due to the response of the quartz beam-splitter in the FT spectrometer.

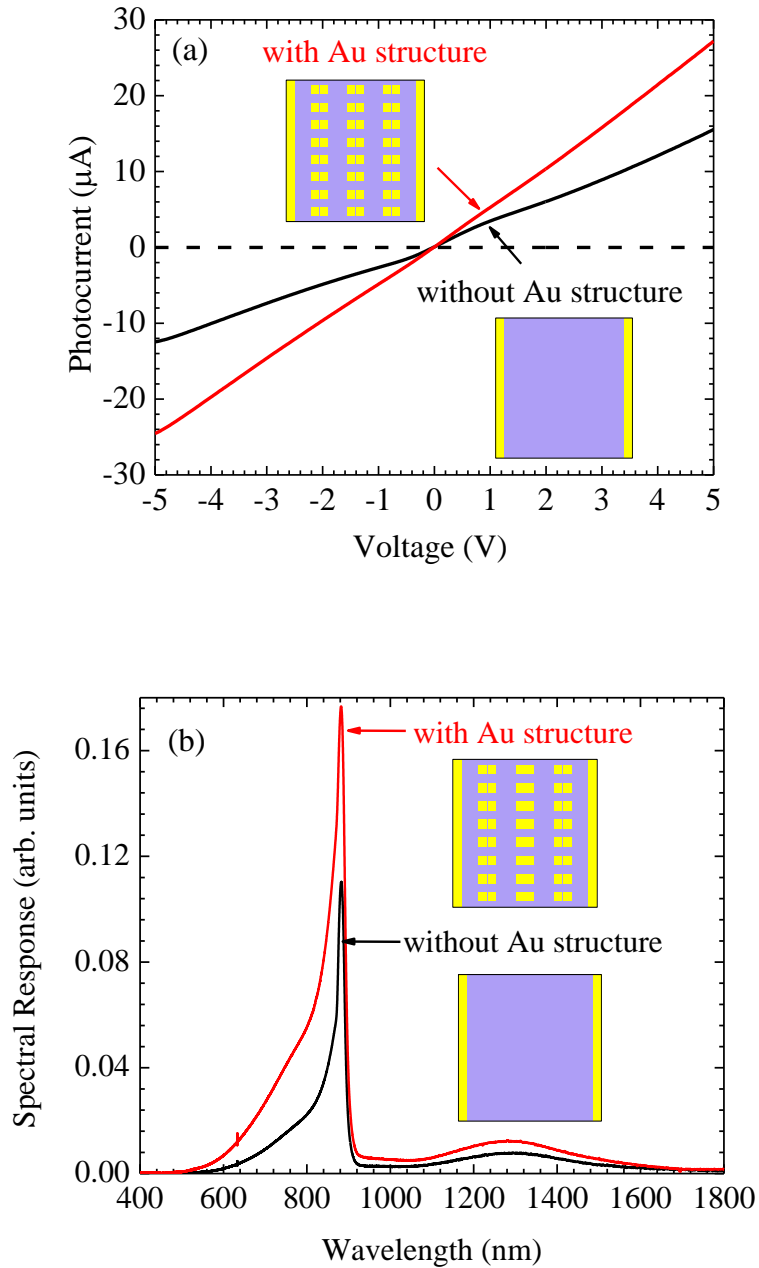


Figure 4.31 Enhancement in (a) the photocurrent and (b) the spectral response after applying an array of Au thin-film with thickness of 50 nm. Reprinted with permission from Nusir *et al* [86].

### Effect of thin-film thickness

The effect of increasing the thickness of the thin-films on the photocurrent enhancement was investigated. Different photodetectors were fabricated with different thicknesses of Au and Ti thin-films. The enhancement in the photocurrent was found by measuring the  $I$ - $V$  curves under illumination before and after applying the array of the metallic pads. Figure 4.32 (a) shows the enhancement in the photocurrent at bias voltage of 5 V as function of Au thickness and without a Ti adhesive layer between the Au and GaAs. The photocurrent enhancement was reduced from 120% to 97%, as the Au thickness was increased from 10 to 50 nm. Next, the photocurrent enhancement was investigated as function of the Ti adhesive layer thickness. The thickness of the Au top layer was kept constant at 10 nm during this investigation. The results are plotted in figure 4.32 (b) and shows that the photocurrent enhancement of the devices was reduced from 120% to 8% as the thickness of the Ti adhesive layer increased to 4 nm.

The result in figure 4.32 (a) implies that the photocurrent enhancement strongly depends on thickness of the Au thin-films and as the Au thickness increases the photocurrent enhancement will decrease. This result matches with the theoretical and experimental work presented by Scales *et al*, which revealed that significant increase in the photoresponse of the devices will be achieved by using thinner Au thin-films [75]. This was attributed to the increase in the emission probability of hot electrons into the semiconductor with thinner thickness of metals. The enhancement in the internal photoemission of hot electrons in thinner Au thin-films is caused by the multiple reflections of hot electrons off the Au/GaAs and Au/air interfaces, as depicted in figure 4.33. This will provide higher emission probability of hot electrons over the Schottky barrier into the semiconductor, as was stated by Scales *et al* [75].

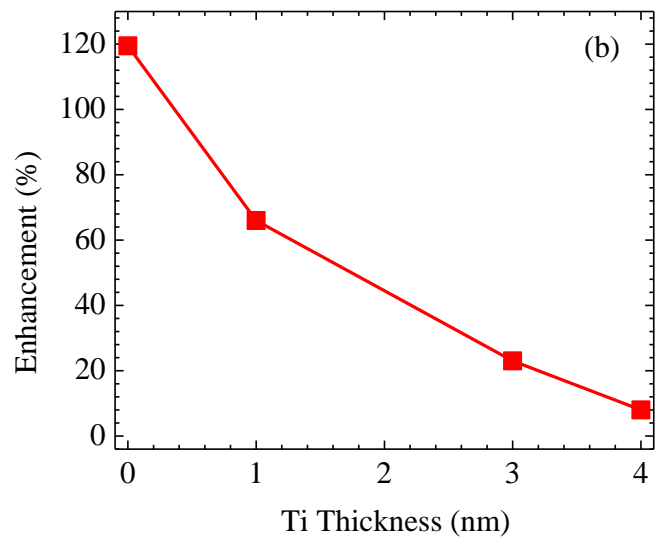
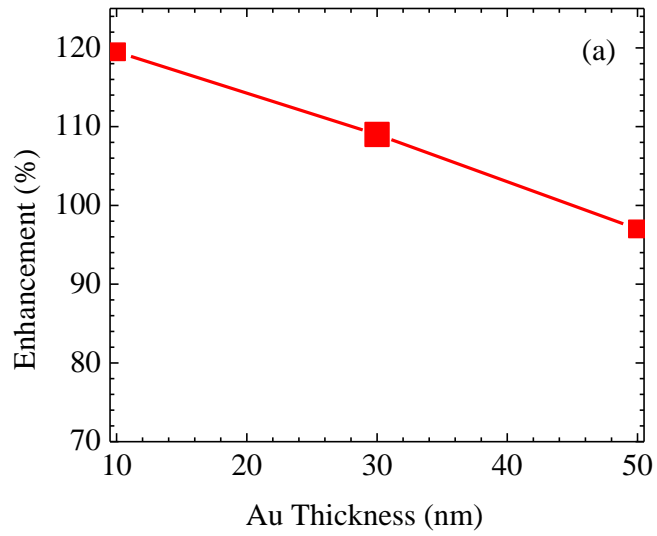


Figure 4.32 Photocurrent enhancement at different: (a) Au and (b) Ti thicknesses. Reprinted with permission from Nusir *et al* [86].

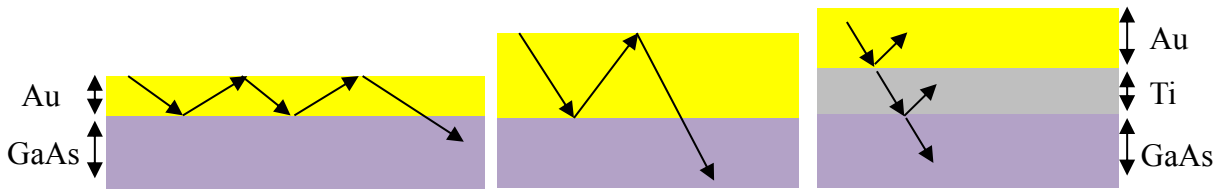


Figure 4.33 Reflections of hot electrons at the interfaces between Au/GaAs and Au/Ti/GaAs.

The result in figure 4.32 (b) showed that the addition of Ti adhesive layer between the Au and the GaAs will significantly reduce the enhancement in the photocurrent. This can be explained by the increase in the path traveled by hot electrons generated in the Au thin-film, which will reduce the emission probability of hot electrons reduces [75]. The addition of Ti layer will create further reflections at the interface between Ti and Au, which will reduce the emission probability of hot electrons, as depicted in figure 4.33.

Surface plasmons can be generated in the metallic structures and assist in generating hot electrons. However in this structure, the effect of plasmons in generating hot electrons is minimized. This is because the plasmons generated at the edge of the structure will decay rapidly before reaching the center of the microstructure, especially the structure is relatively large ( $> 10 \mu\text{m}$ ). Therefore this will prevent the generation of plasmonic resonance. Furthermore, the photocurrent and spectral response did not show any dependence on the polarization direction of the incident light, which is typical for devices based on plasmons [101]. Although the structures presented in this work did not exhibit any plasmonic enhancement. However the microscale arrays showed the ability of absorbing more light and generate further hot electrons. This is due to the large area of the Au structures. The maximum photocurrent enhancement in this work was found to be 120%. This is higher than the percentage of enhancement achieved using plasmonic nanoparticles for solar cells, which was limited to 58% [102].



## V. Conclusions

### A. Summary

Narrow bandgap nanocrystals based on PbSe were investigated for the application of uncooled near-infrared photodetectors. The nanocrystals were grown using wet chemical method and characterized by measuring the optical absorption and photoluminescence to extract the bandgap energy and the size distribution of the nanocrystals. The size of the nanocrystals was tuned by controlling the growth reaction time and measuring the absorbance of nanocrystals at different growth reaction time. The synthesized nanocrystals were functionalized with molecular ligands to improve on the charge transportation between nanocrystals. Afterwards, near-infrared photodetectors were fabricated by coupling the nanocrystals with interdigital electrodes. The devices were characterized by measuring the  $I$ - $V$  characteristics and the spectral response. The dimensions of the interdigital electrodes were optimized by measuring the response of devices with different electrode spacing.

Self-powered near-infrared photodetectors were developed by designing and fabricating asymmetrical Schottky interdigital electrodes. The performance of the devices was optimized by varying the dimensions of the electrodes and the type of the metal contacts. The electrodes were fabricated by using standard optical photolithography on semi-insulating GaAs and undoped Si substrates. The fabricated devices were characterized by measuring the  $I$ - $V$  curves, the spectral response, and EQE at 0 V bias. To further improve on the performance of the self-powered devices, vertically-aligned Si nanowires were grown in the channel between the electrodes. The Si nanowires were grown by using metal-assisted wet etching and characterized by SEM

imaging. Several etching methods based on metal-assisted wet etching were followed to control the diameter and the length of the nanowires.

Hot electrons generated in Au were utilized to enhance the lateral photocurrent circulating between two parallel electrodes deposited on semi-insulating GaAs substrate. This was accomplished by designing and fabricating an array of metallic thin-films. The internal photoemission of the hot electrons was confirmed by measuring the photocurrent map during a sweep of a focused laser over the thin-film. The photocurrent enhancement was measured as function of the thickness of the Au thin-film. Furthermore, the effect of adding a Ti adhesive layer between the Au and the GaAs on the photocurrent enhancement was investigated.

## **B. Contributions**

The work in this dissertation presented the design, fabrication, and characterization of optoelectronic devices based on nanostructures. Several types of nanostructures were investigated for the devices, such as, nanocrystals, nanowires, and thin-films. The optoelectronic devices were designed to detect the near-infrared radiations spanning between the wavelengths of 700 and 1800 nm. The purpose of this investigation is to provide a full design and implementation methodology for future devices based on various types of nanostructures. This includes the growth and processing of the nanomaterials to become suitable for devices. Additionally, the optimization of the device contacts in order to improve on their performance and responsivity.

The first contribution to the field of semiconductor nanomaterials and devices is to utilize PbSe nanocrystals for uncooled near-infrared photodetectors. In this work, the size of the nanocrystals was optimized by setting the growth reaction time to 20 seconds. From the optical

absorbance of the nanocrystals, high quantum confinement was obtained with a first excitonic energy of 0.9 eV, which corresponds to a size of 7 nm. The photoluminescence spectrum showed that the size distribution of the nanocrystals was minimized. The effect of the ligands capping the nanocrystals on the performance of the photodetectors was further investigated. It was found that the device with MAA ligands had lower dark current and larger photocurrent to dark current ratio as compared to the other device with EDT ligands. The EDT ligand is a double functional group which causes the nanocrystals to become closer to each other and as a result cause an increase in the device dark current. The dimensions of the interdigital electrodes for the uncooled photodetectors were optimized. It was found that the device with electrode spacing of 10  $\mu\text{m}$  had larger photocurrent to dark current ratio and stronger spectral response as compared to the other devices with electrode spacing of 20 and 50  $\mu\text{m}$ . The spectral response showed strong operation covering the entire near-infrared region with three separate peaks, producing a wavelength selectivity feature. This feature is the result of the size tunable quantum confinement in the PbSe nanocrystals.

The second contribution to the field is the development of asymmetrical Schottky interdigital contacts for the application of self-powered near-infrared photodetectors. The device performance was optimized by fabricating devices with different electrode spacing. Significant enhancement in the detectivity, EQE, and the spectral response was achieved at zero bias as the electrode spacing was reduced. This enhancement was obtained by the higher built-in electric field in the channel between the electrodes. Furthermore, the effect of the asymmetrical electrodes based on different metal pairs, such as Au-Ti, Au-Ag, and Ag-Ti, was investigated. It was founded that the Au-Ti electrodes produced the strongest response. This is because the

increase in the Schottky barrier height will further strengthen the built-in electric field and provide an efficient separation of photo-excited carrier.

The integration of Si nanowires with the asymmetric interdigital electrodes showed enhancement in the response of the self-powered photodetectors. The Si nanowires were selectively grown between the interdigital electrodes by using electroless etching and Cr hard mask. Enhancement in the short-circuit current and EQE was achieved as compared to other device with planar structure and without nanowires. The spectral response showed rapid increase and broadening above the band-edge of Si. This enhancement is caused by the stronger light absorption due to the increase in the aspect ratio of the active area and the suppression in surface reflection.

In the third investigation, the generated hot electrons in Au thin-films demonstrated the ability to further enhance the photocurrent of devices. This work showed that the photocurrent enhancement strongly depends on the thickness of the Au thin-film and the existence of Ti adhesive layer between the Au and the semiconductor. A decrease in the thickness of the film will increase the injection of hot electrons into the semiconductor and increase the overall photocurrent. This is due to the increase in the emission probability of hot electrons caused by the multiple reflections at the metal/semiconductor interface. The internal photoemission of the hot electrons was confirmed from the peak at wavelength of 1280 nm in the spectral response of the devices. This peak corresponds to the energy of the Schottky barrier formed between Au and GaAs. The enhancement was also confirmed by measuring the photocurrent map using a sweep of focused red laser. The addition of Ti layer between the metal and the semiconductor will damp the enhancement in the photocurrent. This is due to in the further reflection of hot electrons at the interface between Au and Ti, which will reduce the emission probability.

### C. Future Work

Further enhancement in the response of the self-powered photodetectors can be achieved by using longer Si nanowires ( $> 5 \mu\text{m}$ ). Since the longer nanowires will further reduce the surface reflection and increase the light absorption. This requires fabricating thicker Si fingers between the interdigital electrodes using deep RIE. And then the Si fingers will be transformed into nanowires using electroless etching with longer etching time in the HF acid ( $> 1$  hour). This requires further SEM imaging of the Si nanowires to measure the nanowires length as function of longer electroless etching time. Additionally, the integration of Si nanowires between asymmetrical electrodes with less electrode spacing ( $5 \mu\text{m}$ ) will produce strong responsivity of the photodetectors at 0 V bias.

Nanostructures, such as, nanocones and nanowires, can be used with solar cells as an antireflection coatings to increase the power conversion efficiency. The nanostructures can be etched on the surface of GaAs solar cell by using the nanosphere lithography procedure presented in chapter 3 of this dissertation. The polystyrene nanospheres will be first coated on the surface of the GaAs solar cell and then tailored to the required diameter using  $\text{O}_2$  plasma RIE etching. Second, the nanospheres will be used as an etching mask to grow vertically-aligned nanostructures on the surface of the GaAs solar cell. The etching can be performed using RIE and gases, such as,  $\text{Cl}_2$  and  $\text{BCl}_3$ . The nanocones can be grown by using inductive coupled plasma RIE etching to control the anisotropy of the etching profile.

## References

- [1] X. Lan, O. Voznyy, F. P. G. Arquer, M. Liu, J. Xu, A. H. Proppe, G. Walters, F. Fan, H. Tan, M. Liu, Z. Yang, S. Hoogland, and E. H. Sargent\*, “10.6% Certified Colloidal Quantum Dot Solar Cells via Solvent-Polarity-Engineered Halide Passivation,” *Nano Lett.*, vol. 16, no. 7, pp. 4630–4634, Jul. 2016.
- [2] A. C. Scofield, A. Lin, M. Haddad, and D. L. Huffaker, “Axial Diffusion Barriers in Near-Infrared Nanopillar LEDs,” *Nano Lett.*, vol. 14, no. 11, pp. 6037–6041, Nov. 2014.
- [3] P. J. Ko, A. Abderrahmane, N. Kim, and A. Sandhu, “High-performance near-infrared photodetector based on nano-layered MoSe<sub>2</sub>,” *Semicond. Sci. Technol.*, vol. 32, no. 6, p. 065015, Jun. 2017.
- [4] T. Mueller, F. Xia, and P. Avouris, “Graphene photodetectors for high-speed optical communications,” *Nat. Photonics*, vol. 4, no. 5, pp. 297–301, May 2010.
- [5] G. Hong, A. L. Antaris, and H. Dai, “Near-infrared fluorophores for biomedical imaging,” *Nat. Biomed. Eng.*, vol. 1, no. 1, p. 0010, Jan. 2017.
- [6] J. Frangioni, “In vivo near-infrared fluorescence imaging,” *Curr. Opin. Chem. Biol.*, vol. 7, no. 5, pp. 626–634, Oct. 2003.
- [7] Zhengmao Ye, J. C. Campbell, Zhonghui Chen, Eui-Tae Kim, and A. Madhukar, “Normal-incidence InAs self-assembled quantum-dot infrared photodetectors with a high detectivity,” *IEEE J. Quantum Electron.*, vol. 38, no. 9, pp. 1234–1237, Sep. 2002.
- [8] G. Konstantatos, I. Howard, A. Fischer, S. Hoogland, J. Clifford, E. Klem, L. Levina, and E. H. Sargent, “Ultrasensitive solution-cast quantum dot photodetectors,” *Nature*, vol. 442, no. 7099, pp. 180–183, Jul. 2006.
- [9] T. Rauch, M. Böberl, S. F. Tedde, J. Fürst, M. V. Kovalenko, G. Hesser, U. Lemmer, W. Heiss, and O. Hayden, “Near-infrared imaging with quantum-dot-sensitized organic photodiodes,” *Nat. Photonics*, vol. 3, no. 6, pp. 332–336, Jun. 2009.
- [10] Z. Yang, O. Voznyy, G. Walters, J. Z. Fan, M. Liu, S. Kinge, S. Hoogland, and E. H. Sargent, “Quantum Dots in Two-Dimensional Perovskite Matrices for Efficient Near-Infrared Light Emission,” *ACS Photonics*, vol. 4, no. 4, pp. 830–836, Apr. 2017.
- [11] B. W. Boote, L. Men, H. P. Andaraarachchi, U. Bhattacharjee, J. W. Petrich, J. Vela, and E. A. Smith, “Germanium–Tin/Cadmium Sulfide Core/Shell Nanocrystals with Enhanced Near-Infrared Photoluminescence,” *Chem. Mater.*, vol. 29, no. 14, pp. 6012–6021, Jul. 2017.
- [12] J. Lähnemann, A. Ajay, M. I. Den Hertog, and E. Monroy, “Near-Infrared Intersubband Photodetection in GaN/AlN Nanowires,” *Nano Lett.*, vol. 17, no. 11, pp. 6954–6960 Oct. 2017.
- [13] L. Shen, E. Y. B. Pun, and J. C. Ho, “Recent developments in III–V semiconducting nanowires for high-performance photodetectors,” *Mater Chem Front*, vol. 1, no. 4, pp. 630–645, 2017.

- [14] R. R. LaPierre, M. Robson, K. M. Azizur-Rahman, and P. Kuyanov, "A review of III–V nanowire infrared photodetectors and sensors," *J. Phys. Appl. Phys.*, vol. 50, no. 12, p. 123001, Mar. 2017.
- [15] N. P. Dasgupta, J. Sun, C. Liu, S. Brittan, S. C. Andrews, J. Lim, H. Gao, R. Yan, and P. Yang "25th Anniversary Article: Semiconductor Nanowires - Synthesis, Characterization, and Applications," *Adv. Mater.*, vol. 26, no. 14, pp. 2137–2184, Apr. 2014.
- [16] G.-C. Yi, C. Wang, and W. I. Park, "ZnO nanorods: synthesis, characterization and applications," *Semicond. Sci. Technol.*, vol. 20, no. 4, pp. S22–S34, Apr. 2005.
- [17] E. Garnett and P. Yang, "Light Trapping in Silicon Nanowire Solar Cells," *Nano Lett.*, vol. 10, no. 3, pp. 1082–1087, Mar. 2010.
- [18] A. M. Smith and S. Nie, "Semiconductor Nanocrystals: Structure, Properties, and Band Gap Engineering," *Acc. Chem. Res.*, vol. 43, no. 2, pp. 190–200, Feb. 2010.
- [19] B.-R. Huang, Y.-K. Yang, and W.-L. Yang, "Efficiency improvement of silicon nanostructure-based solar cells," *Nanotechnology*, vol. 25, no. 3, p. 035401, Jan. 2014.
- [20] V. R. Voggu, J. Sham, S. Pfeffer, J. Pate, L. Phillip, T. B. Harvey, R. M. Brown, and B. A. Korgel, "Flexible CuInSe<sub>2</sub> Nanocrystal Solar Cells on Paper," *ACS Energy Lett.*, vol. 2, no. 3, pp. 574–581, Mar. 2017.
- [21] A. I. Nusir, J. Aguilar, Z. Bever, and M. O. Manasreh, "Uncooled photodetectors based on CdSe nanocrystals with an interdigital metallization," *Appl. Phys. Lett.*, vol. 104, no. 5, p. 051124, Feb. 2014.
- [22] G. Li, Z.-K. Tan, D. Di, M. L. Lai, L. Jiang, J. H.-W. Lim, R. H. Friend, and N. C. Greenham, "Efficient Light-Emitting Diodes Based on Nanocrystalline Perovskite in a Dielectric Polymer Matrix," *Nano Lett.*, vol. 15, no. 4, pp. 2640–2644, Apr. 2015.
- [23] P. Fan, B. Bai, J. Long, D. Jiang, G. Jin, H. Zhang, and M. Zhong, "Broadband High-Performance Infrared Antireflection Nanowires Facilely Grown on Ultrafast Laser Structured Cu Surface," *Nano Lett.*, vol. 15, no. 9, pp. 5988–5994, Sep. 2015.
- [24] J.-Y. Jung, Z. Guo, S.-W. Jee, H.-D. Um, K.-T. Park, and J.-H. Lee, "A strong antireflective solar cell prepared by tapering silicon nanowires," *Opt. Express*, vol. 18, no. S3, p. A286, Sep. 2010.
- [25] A. H. Khan, R. Brescia, A. Polovitsyn, I. Angeloni, B. Martín-García, and I. Moreels, "Near-Infrared Emitting Colloidal PbS Nanoplatelets: Lateral Size Control and Optical Spectroscopy," *Chem. Mater.*, vol. 29, no. 7, pp. 2883–2889, Apr. 2017.
- [26] J. E. Murphy, M. C. Beard, A. G. Norman, S. P. Ahrenkiel, J. C. Johnson, P. Yu, O. I. Mićić, R. J. Ellingson, and A. J. Nozik, "PbTe Colloidal Nanocrystals: Synthesis, Characterization, and Multiple Exciton Generation," *J. Am. Chem. Soc.*, vol. 128, no. 10, pp. 3241–3247, Mar. 2006.

- [27] X. Pang, L. Zhao, W. Han, X. Xin, and Z. Lin, "A general and robust strategy for the synthesis of nearly monodisperse colloidal nanocrystals," *Nat. Nanotechnol.*, vol. 8, no. 6, pp. 426–431, Jun. 2013.
- [28] J. Park, K. H. Lee, J. F. Galloway, and P. C. Searson, "Synthesis of Cadmium Selenide Quantum Dots from a Non-Coordinating Solvent: Growth Kinetics and Particle Size Distribution," *J. Phys. Chem. C*, vol. 112, no. 46, pp. 17849–17854, Nov. 2008.
- [29] J. Zhao, J. A. Bardecker, A. M. Munro, M. S. Liu, Y. Niu, I.-K. Ding, J. Luo, B. Chen, A. K.-Y. Jen, and D. S. Ginger, "Efficient CdSe/CdS Quantum Dot Light-Emitting Diodes Using a Thermally Polymerized Hole Transport Layer," *Nano Lett.*, vol. 6, no. 3, pp. 463–467, Mar. 2006.
- [30] S.-H. Kang, C. K. Kumar, Z. Lee, K.-H. Kim, C. Huh, and E.-T. Kim, "Quantum-dot light-emitting diodes utilizing CdSe/ZnS nanocrystals embedded in TiO<sub>2</sub> thin film," *Appl. Phys. Lett.*, vol. 93, no. 19, p. 191116, Nov. 2008.
- [31] H. Zhong, Z. Wang, E. Bovero, Z. Lu, F. C. J. M. van Veggel, and G. D. Scholes, "Colloidal CuInSe<sub>2</sub> Nanocrystals in the Quantum Confinement Regime: Synthesis, Optical Properties, and Electroluminescence," *J. Phys. Chem. C*, vol. 115, no. 25, pp. 12396–12402, Jun. 2011.
- [32] H. Huang, M. I. Bodnarchuk, S. V. Kershaw, M. V. Kovalenko, and A. L. Rogach, "Lead Halide Perovskite Nanocrystals in the Research Spotlight: Stability and Defect Tolerance," *ACS Energy Lett.*, vol. 2, no. 9, pp. 2071–2083, Sep. 2017.
- [33] S. D. Gunapala, S. V. Bandara, J. K. Liu, J. M. Mumolo, S. B. Rafol, D. Z. Ting, A. Soibel, and C. Hill, "Quantum Well Infrared Photodetector Technology and Applications," *IEEE J. Sel. Top. Quantum Electron.*, vol. 20, no. 6, pp. 154–165, Nov. 2014.
- [34] B. S. Passmore, Jiang Wu, M. O. Manasreh, V. P. Kunets, P. M. Lytvyn, and G. J. Salamo, "Room Temperature Near-Infrared Photoresponse Based on Interband Transitions in In<sub>0.35</sub>Ga<sub>0.65</sub>As Multiple Quantum Dot Photodetector," *IEEE Electron Device Lett.*, vol. 29, no. 3, pp. 224–227, Mar. 2008.
- [35] R. Saran and R. J. Curry, "Lead sulphide nanocrystal photodetector technologies," *Nat. Photonics*, vol. 10, no. 2, pp. 81–92, Jan. 2016.
- [36] M. Böberl, M. V. Kovalenko, S. Gamerith, E. J. W. List, and W. Heiss, "Inkjet-Printed Nanocrystal Photodetectors Operating up to 3  $\mu$ m Wavelengths," *Adv. Mater.*, vol. 19, no. 21, pp. 3574–3578, Nov. 2007.
- [37] Y. Yu, Y. Zhang, Z. Zhang, H. Zhang, X. Song, M. Cao, Y. Che, H. Dai, J. Yang, J. Wang, H. Zhang, and J. Yao, "Broadband Phototransistor Based on CH<sub>3</sub>NH<sub>3</sub>PbI<sub>3</sub> Perovskite and PbSe Quantum Dot Heterojunction," *J. Phys. Chem. Lett.*, vol. 8, no. 2, pp. 445–451, Jan. 2017.



- [38] J. J. Choi, Y.-F. Lim, M. B. Santiago-Berrios, M. Oh, B.-R. Hyun, L. Sun, A. C. Bartnik, A. Goedhart, G. G. Malliaras, H. D. Abruña, F. W. Wise, and T. Hanrath, “PbSe Nanocrystal Excitonic Solar Cells,” *Nano Lett.*, vol. 9, no. 11, pp. 3749–3755, Nov. 2009.
- [39] H. Zhang, Y. Zhang, X. Song, Y. Yu, M. Cao, Y. Che, J. Wang, J. Yang, H. Dai, G. Zhang, and J. Yao, “High performance PbSe colloidal quantum dot vertical field effect phototransistors,” *Nanotechnology*, vol. 27, no. 42, p. 425204, Oct. 2016.
- [40] H. Fu, W. Luan, and S.-T. Tu, “A simple route for synthesis of PbSe nanocrystals: shape control by ligand and reaction time,” *Dalton Trans.*, vol. 41, no. 39, p. 12254, 2012.
- [41] I. Kang and F. W. Wise, “Electronic structure and optical properties of PbS and PbSe quantum dots,” *J. Opt. Soc. Am. B*, vol. 14, no. 7, p. 1632, Jul. 1997.
- [42] J. M. Pietryga, R. D. Schaller, D. Werder, M. H. Stewart, V. I. Klimov, and J. A. Hollingsworth, “Pushing the Band Gap Envelope: Mid-Infrared Emitting Colloidal PbSe Quantum Dots,” *J. Am. Chem. Soc.*, vol. 126, no. 38, pp. 11752–11753, Sep. 2004.
- [43] A. Dong, X. Ye, J. Chen, Y. Kang, T. Gordon, J. M. Kikkawa, and C. B. Murray, “A Generalized Ligand-Exchange Strategy Enabling Sequential Surface Functionalization of Colloidal Nanocrystals,” *J. Am. Chem. Soc.*, vol. 133, no. 4, pp. 998–1006, Feb. 2011.
- [44] W. W. Yu, J. C. Falkner, B. S. Shih, and V. L. Colvin, “Preparation and Characterization of Monodisperse PbSe Semiconductor Nanocrystals in a Noncoordinating Solvent,” *Chem. Mater.*, vol. 16, no. 17, pp. 3318–3322, Aug. 2004.
- [45] A. Nusir and O. Manasreh, “Effect of ligand exchange on the photoresponsivity of near-infrared sensors based on PbSe nanocrystals,” *2016 IEEE SENSORS*, Orlando, FL, USA, pp. 1–3, Oct 2016.
- [46] O. Manasreh, *Introduction to nanomaterials and devices*. Hoboken, NJ: Wiley, 2012.
- [47] S. Guillemin, L. Rapenne, H. Roussel, E. Sarigiannidou, G. Brémond, and V. Consonni, “Formation Mechanisms of ZnO Nanowires: The Crucial Role of Crystal Orientation and Polarity,” *J. Phys. Chem. C*, vol. 117, no. 40, pp. 20738–20745, Oct. 2013.
- [48] M. A. Othman, N. F. Amat, B. H. Ahmad, and J. Rajan, “Electrical Conductivity Characteristic of TiO<sub>2</sub> Nanowires From Hydrothermal Method,” *J. Phys. Conf. Ser.*, vol. 495, p. 012027, Apr. 2014.
- [49] B. J. M. Brenny, D. R. Abujetas, D. van Dam, J. A. Sánchez-Gil, J. G. Rivas, and A. Polman, “Directional Emission from Leaky and Guided Modes in GaAs Nanowires Measured by Cathodoluminescence,” *ACS Photonics*, vol. 3, no. 4, pp. 677–684, Apr. 2016.
- [50] S. Christiansen, R. Schneider, R. Scholz, U. Gösele, T. Stelzner, G. Andrä, E. Wendler, and W. Wesch, “Vapor-liquid-solid growth of silicon nanowires by chemical vapor deposition on implanted templates,” *J. Appl. Phys.*, vol. 100, no. 8, p. 084323, Oct. 2006.

- [51] H. Wang, M. Sun, K. Ding, M. T. Hill, and C.-Z. Ning, "A Top-down Approach to Fabrication of High Quality Vertical Heterostructure Nanowire Arrays," *Nano Lett.*, vol. 11, no. 4, pp. 1646–1650, Apr. 2011.
- [52] C. Xie, P. Lv, B. Nie, J. Jie, X. Zhang, Z. Wang, P. Jiang, Z. Hu, L. Luo, Z. Zhu, L. Wang, and C. Wu, "Monolayer graphene film/silicon nanowire array Schottky junction solar cells," *Appl. Phys. Lett.*, vol. 99, no. 13, p. 133113, Sep. 2011.
- [53] L. Tsakalakos, J. Balch, J. Fronheiser, B. A. Korevaar, O. Sulima, and J. Rand, "Silicon nanowire solar cells," *Appl. Phys. Lett.*, vol. 91, no. 23, p. 233117, Dec. 2007.
- [54] M. D. Kelzenberg, D. B. Turner-Evans, B. M. Kayes, M. A. Filler, M. C. Putnam, N. S. Lewis, and H. A. Atwater, "Photovoltaic Measurements in Single-Nanowire Silicon Solar Cells," *Nano Lett.*, vol. 8, no. 2, pp. 710–714, Feb. 2008.
- [55] C. Xie, J. Jie, B. Nie, T. Yan, Q. Li, P. Lv, F. Li, M. Wang, C. Wu, L. Wang, and L. Luo "Schottky solar cells based on graphene nanoribbon/multiple silicon nanowires junctions," *Appl. Phys. Lett.*, vol. 100, no. 19, p. 193103, May 2012.
- [56] O. H. A. Zoubi, T. M. Said, M. A. Alher, S. E. Ghazaly, and H. Naseem, "Broadband high efficiency silicon nanowire arrays with radial diversity within diamond-like geometrical distribution for photovoltaic applications," *Opt. Express*, vol. 23, no. 15, p. A767, Jul. 2015.
- [57] L.-B. Luo, L.-H. Zeng, C. Xie, Y.-Q. Yu, F.-X. Liang, C.-Y. Wu, L. Wang, and J.-G. Hu, "Light trapping and surface plasmon enhanced high-performance NIR photodetector," *Sci. Rep.*, vol. 4, no. 1, May 2015.
- [58] D. Lee, J. Bae, S. Hong, H. Yang, and Y.-B. Kim, "Optimized antireflective silicon nanostructure arrays using nanosphere lithography," *Nanotechnology*, vol. 27, no. 21, p. 215302, May 2016.
- [59] Z. Huang, N. Geyer, P. Werner, J. de Boor, and U. Gösele, "Metal-Assisted Chemical Etching of Silicon: A Review: In memory of Prof. Ulrich Gösele," *Adv. Mater.*, vol. 23, no. 2, pp. 285–308, Jan. 2011.
- [60] C. Pan, Z. Luo, C. Xu, J. Luo, R. Liang, G. Zhu, W. Wu, W. Guo, X. Yan, J. Xu, Z. L. Wang, and J. Zhu, "Wafer-Scale High-Throughput Ordered Arrays of Si and Coaxial Si/Si<sub>1-x</sub>Ge<sub>x</sub> Wires: Fabrication, Characterization, and Photovoltaic Application," *ACS Nano*, vol. 5, no. 8, pp. 6629–6636, Aug. 2011.
- [61] H. Park and K. B. Crozier, "Vertically Stacked Photodetector Devices Containing Silicon Nanowires with Engineered Absorption Spectra," *ACS Photonics*, vol. 2, no. 4, pp. 544–549, Apr. 2015.
- [62] V. T. Pham, M. Dutta, H. T. Bui, and N. Fukata, "Effect of nanowire length on the performance of silicon nanowires based solar cell," *Adv. Nat. Sci. Nanosci. Nanotechnol.*, vol. 5, no. 4, p. 045014, Nov. 2014.
- [63] C. L. Cheung, R. J. Nikolić, C. E. Reinhardt, and T. F. Wang, "Fabrication of nanopillars by nanosphere lithography," *Nanotechnology*, vol. 17, no. 5, pp. 1339–1343, Mar. 2006.

- [64] L. Li, N. Coates, and D. Moses, "Solution-Processed Inorganic Solar Cell Based on in Situ Synthesis and Film Deposition of CuInS<sub>2</sub> Nanocrystals," *J. Am. Chem. Soc.*, vol. 132, no. 1, pp. 22–23, Jan. 2010.
- [65] A. K. Rath, M. Bernechea, L. Martinez, and G. Konstantatos, "Solution-Processed Heterojunction Solar Cells Based on p-type PbS Quantum Dots and n-type Bi<sub>2</sub>S<sub>3</sub> Nanocrystals," *Adv. Mater.*, vol. 23, no. 32, pp. 3712–3717, Aug. 2011.
- [66] J. Bae, H. Kim, X.-M. Zhang, C. H. Dang, Y. Zhang, Y. Jin Choi, A. Nurmikko, and Z. Lin Wang, "Si nanowire metal–insulator–semiconductor photodetectors as efficient light harvesters," *Nanotechnology*, vol. 21, no. 9, p. 095502, Mar. 2010.
- [67] P. Fan, K. C. Y. Huang, L. Cao, and M. L. Brongersma, "Redesigning Photodetector Electrodes as an Optical Antenna," *Nano Lett.*, vol. 13, no. 2, pp. 392–396, Feb. 2013.
- [68] H. Kumar, Y. Kumar, G. Rawat, C. Kumar, B. Mukherjee, B. N. Pal, and S. Jit, "Colloidal CdSe Quantum Dots and PQT-12-Based Low-Temperature Self-Powered Hybrid Photodetector," *IEEE Photonics Technol. Lett.*, vol. 29, no. 20, pp. 1715–1718, Oct. 2017.
- [69] S. J. Young, L. W. Ji, R. W. Chuang, S. J. Chang, and X. L. Du, "Characterization of ZnO metal–semiconductor–metal ultraviolet photodiodes with palladium contact electrodes," *Semicond. Sci. Technol.*, vol. 21, no. 10, pp. 1507–1511, Oct. 2006.
- [70] L. Qin, C. Shing, and S. Sawyer, "Metal-Semiconductor-Metal Ultraviolet Photodetectors Based on Zinc-Oxide Colloidal Nanoparticles," *IEEE Electron Device Lett.*, vol. 32, no. 1, pp. 51–53, Jan. 2011.
- [71] D. Li, X. Sun, H. Song, Z. Li, H. Jiang, Y. Chen, G. Miao, and B. Shen "Effect of asymmetric Schottky barrier on GaN-based metal–semiconductor–metal ultraviolet detector," *Appl. Phys. Lett.*, vol. 99, no. 26, p. 261102, Dec. 2011.
- [72] W. Li and J. G. Valentine, "Harvesting the loss: surface plasmon-based hot electron photodetection," *Nanophotonics*, vol. 6, no. 1, Jan. 2017.
- [73] H. Chalabi, D. Schoen, and M. L. Brongersma, "Hot-Electron Photodetection with a Plasmonic Nanostripe Antenna," *Nano Lett.*, vol. 14, no. 3, pp. 1374–1380, Mar. 2014.
- [74] M. W. Knight, H. Sobhani, P. Nordlander, and N. J. Halas, "Photodetection with Active Optical Antennas," *Science*, vol. 332, no. 6030, pp. 702–704, May 2011.
- [75] C. Scales and P. Berini, "Thin-Film Schottky Barrier Photodetector Models," *IEEE J. Quantum Electron.*, vol. 46, no. 5, pp. 633–643, May 2010.
- [76] T. Hong, B. Chamlagain, S. Hu, S. M. Weiss, Z. Zhou, and Y.-Q. Xu, "Plasmonic Hot Electron Induced Photocurrent Response at MoS<sub>2</sub>–Metal Junctions," *ACS Nano*, vol. 9, no. 5, pp. 5357–5363, May 2015.
- [77] G. Sarasqueta, K. R. Choudhury, J. Subbiah, and F. So, "Organic and Inorganic Blocking Layers for Solution-Processed Colloidal PbSe Nanocrystal Infrared Photodetectors," *Adv. Funct. Mater.*, vol. 21, no. 1, pp. 167–171, Jan. 2011.

- [78] J. M. Luther, M. Law, Q. Song, C. L. Perkins, M. C. Beard, and A. J. Nozik, "Structural, Optical, and Electrical Properties of Self-Assembled Films of PbSe Nanocrystals Treated with 1,2-Ethanedithiol," *ACS Nano*, vol. 2, no. 2, pp. 271–280, Feb. 2008.
- [79] J. Huang, S. Y. Chiam, H. H. Tan, S. Wang, and W. K. Chim, "Fabrication of Silicon Nanowires with Precise Diameter Control Using Metal Nanodot Arrays as a Hard Mask Blocking Material in Chemical Etching," *Chem. Mater.*, vol. 22, no. 13, pp. 4111–4116, Jul. 2010.
- [80] H. Han, Z. Huang, and W. Lee, "Metal-assisted chemical etching of silicon and nanotechnology applications," *Nano Today*, vol. 9, no. 3, pp. 271–304, Jun. 2014.
- [81] S. Manna, S. Das, S. P. Mondal, R. Singha, and S. K. Ray, "High Efficiency Si/CdS Radial Nanowire Heterojunction Photodetectors Using Etched Si Nanowire Templates," *J. Phys. Chem. C*, vol. 116, no. 12, pp. 7126–7133, Mar. 2012.
- [82] B. Ozdemir, M. Kulakci, R. Turan, and H. E. Unalan, "Effect of electroless etching parameters on the growth and reflection properties of silicon nanowires," *Nanotechnology*, vol. 22, no. 15, p. 155606, Apr. 2011.
- [83] A. Nusir, J. Aguilar, J. Hill, H. Morris, and M. O. Manasreh, "Uncooled Infrared Photodetector Utilizing PbSe Nanocrystals," *IEEE Trans. Nanotechnol.*, vol. 15, no. 1, pp. 109–112, Jan. 2016.
- [84] A. I. Nusir and M. O. Manasreh, "Self-Powered Near-Infrared Photodetector Based on Asymmetrical Schottky Interdigital Contacts," *IEEE Electron Device Lett.*, vol. 36, no. 11, pp. 1172–1175, Nov. 2015.
- [85] A. I. Nusir, S. J. Bauman, M. S. Marie, J. B. Herzog, and M. O. Manasreh, "Silicon nanowires to enhance the performance of self-powered near-infrared photodetectors with asymmetrical Schottky contacts," *Appl. Phys. Lett.*, vol. 111, no. 17, p. 171103, Oct. 2017.
- [86] A. I. Nusir, G. P. Abbey, A. M. Hill, O. Manasreh, and J. B. Herzog, "Hot Electrons in Microscale Thin-Film Schottky Barriers for Enhancing Near-Infrared Detection," *IEEE Photonics Technol. Lett.*, vol. 28, no. 20, pp. 2241–2244, Oct. 2016.
- [87] B. L. Wehrenberg, C. Wang, and P. Guyot-Sionnest, "Interband and Intraband Optical Studies of PbSe Colloidal Quantum Dots," *J. Phys. Chem. B*, vol. 106, no. 41, pp. 10634–10640, Oct. 2002.
- [88] S. V. Averine, Y. C. Chan, and Y. L. Lam, "Optimization of high-speed MSM-photodiode structures," in *Proc. Optoelectron. Microelectron. Mater. Devices Conf.*, 2000, pp. 515–518.
- [89] G. Sarasqueta, K. R. Choudhury, and F. So, "Effect of Solvent Treatment on Solution-Processed Colloidal PbSe Nanocrystal Infrared Photodetectors," *Chem. Mater.*, vol. 22, no. 11, pp. 3496–3501, Jun. 2010.

- [90] D. Cui, Jian Xu, Sheng-Yong Xu, G. Paradee, B. A. Lewis, and M. D. Gerhold, “Infrared photodiode based on colloidal PbSe nanocrystal quantum dots,” *IEEE Trans. Nanotechnol.*, vol. 5, no. 4, pp. 362–367, Jul. 2006.
- [91] L.-B. Luo, J.-J. Chen, M.-Z. Wang, H. Hu, C.-Y. Wu, Q. Li, L. Wang, J.-A. Huang, and F.-X. Liang, “Near-Infrared Light Photovoltaic Detector Based on GaAs Nanocone Array/Monolayer Graphene Schottky Junction,” *Adv. Funct. Mater.*, vol. 24, no. 19, pp. 2794–2800, May 2014.
- [92] A. D. Stiff, S. Krishna, P. Bhattacharya, and S. W. Kennerly, “Normal-incidence, high-temperature, mid-infrared, InAs-GaAs vertical quantum-dot infrared photodetector,” *IEEE J. Quantum Electron.*, vol. 37, no. 11, pp. 1412–1419, Nov. 2001.
- [93] J. C. Sarker, R. Vasan, Y. F. Makableh, S. Lee, A. I. Nusir, and M. O. Manasreh, “Enhanced performance of surface modified InAs quantum dots solar cell by a sol-gel grown tantalum pentoxide antireflection coating,” *Sol. Energy Mater. Sol. Cells*, vol. 127, pp. 58–62, Aug. 2014.
- [94] H. A. Atwater and A. Polman, “Plasmonics for improved photovoltaic devices,” *Nat. Mater.*, vol. 9, no. 3, pp. 205–213, Mar. 2010.
- [95] S. K. Srivastava, D. Kumar, P. K. Singh, M. Kar, V. Kumar, and M. Husain, “Excellent antireflection properties of vertical silicon nanowire arrays,” *Sol. Energy Mater. Sol. Cells*, vol. 94, no. 9, pp. 1506–1511, Sep. 2010.
- [96] K. Das, S. Mukherjee, S. Manna, S. K. Ray, and A. K. Raychaudhuri, “Single Si nanowire (diameter  $\leq 100$  nm) based polarization sensitive near-infrared photodetector with ultra-high responsivity,” *Nanoscale*, vol. 6, no. 19, pp. 11232–11239, 2014.
- [97] Y. Dan, K. Seo, K. Takei, J. H. Meza, A. Javey, and K. B. Crozier, “Dramatic Reduction of Surface Recombination by in Situ Surface Passivation of Silicon Nanowires,” *Nano Lett.*, vol. 11, no. 6, pp. 2527–2532, Jun. 2011.
- [98] M. M. Adachi, K. Wang, F. Chen, and K. S. Karim, “Silicon nanowire metal-semiconductor-metal photodetectors,” *Proc SPIE*, vol. 7622, p. 76224M, Mar. 2010.
- [99] E. Mulazimoglu, S. Coskun, M. Gunoven, B. Butun, E. Ozbay, R. Turan, and H. E. Unalan, “Silicon nanowire network metal-semiconductor-metal photodetectors,” *Appl. Phys. Lett.*, vol. 103, no. 8, p. 083114, Aug. 2013.
- [100] L. P. Hackett, M. A. Seyedi, M. Fiorentino, and R. G. Beausoleil, “Large-area silicon nanowire Schottky junction photodetector with tunable absorption and low junction capacitance,” *J. Phys. Appl. Phys.*, vol. 50, no. 21, p. 215105, Jun. 2017.
- [101] J. B. Herzog, M. W. Knight, Y. Li, K. M. Evans, N. J. Halas, and D. Natelson, “Dark Plasmons in Hot Spot Generation and Polarization in Interelectrode Nanoscale Junctions,” *Nano Lett.*, vol. 13, no. 3, pp. 1359–1364, Mar. 2013.

- [102] E. S. Arinze, B. Qiu, G. Nyirjesy, and S. M. Thon, “Plasmonic Nanoparticle Enhancement of Solution-Processed Solar Cells: Practical Limits and Opportunities,” *ACS Photonics*, vol. 3, no. 2, pp. 158–173, Feb. 2016.